Advances in Structural LEED Analyses of Silicon Surfaces

Dissertation

zur Erlangung des Grades eines
Doktors der Naturwissenschaften (Dr. rer. nat.)

dem Fachbereich Physik der Universität Osnabrück
vorgelegt von

Jascha Bahlmann, M.Sc.

Osnabrück, August 2022

Contents

1. Introduction

Silicon substrates have been always of particular interest due to their important role in the semiconductor industry as an integral part of transistors, thus being the foundation of a majority of modern technology like computers, smart phones, and many other devices. To understand the electronic properties of surface structures and hence be able to tailor their characteristics, knowledge of the underlying atomic structure is of utmost importance. However, obtaining geometrical atomic information of surfaces is no trivial task due to the complex interactions happening at these interfaces.

Low-energy electron diffraction (LEED) is one possible experimental approach to determine atomic positions within the surface, as opposed to purely theoretical approaches like *ab initio* density-functional theory (DFT) calculations. Nonetheless, structural analysis by LEED requires the application of multiple scattering theory to interpret the measurements adequately. These calculations limit the complexity of the structures that can be investigated successfully by LEED.

For example, the covalent bonds of silicon can lead to complex displacements of atoms near the surface, making the determination of the structure increasingly complicated. This is further aggravated by the interaction of adsorbates, forming reconstructions, which can have interesting electronic properties. The self-induced formation of quasi-one-dimensional nanowires is a type of structures promising physical properties, which can not be found in systems with higher dimensionality, as Peierls instability [1], needing the Luttinger liquid theory [2] as an alternative description of the interacting particles. The term *quasi-one-dimensional* originates from the fact that real one-dimensional systems are not stable and need therefore a substrate for stabilization, making the system quasi-one-dimensional. A prominent example for those wires is the Si(111)-(5×2)-Au reconstruction [3–5], which is also an example of the difficulties of structural analyses, being still debated over 50 years after its discovery. Furthermore, the self-assembled gold chains on vicinal Si(hhk) substrates [6–8] are another group of self-assembled nanowires. Thereby, the terraces of the vicinal substrates predetermine the growth direction of nanowires.

Experimental structural analysis of such material systems is predominantly carried out by X-ray diffraction (XRD), which can be described by a single scattering formalism. Large unit cells combined with reconstructions reaching deep into the crystal make the inclusion of the effects of multiple scattering for the description of electron diffraction much more challenging, which is the reason why structural LEED analyses of large unit cells are rather rare. This thesis aims to examine these material systems and propose possible improvements to advance the structural determination of complex crystalline surfaces.

The first part (Chapters 2, 3 and 4) discusses the theoretical foundations as well as the material systems relevant within this thesis and gives an overview of the used experimental setup. Chapter 5 covers the analysis of the Si(001) surface and proposes an approach to facilitate the LEED analysis of covalent crystal surfaces. Chapter 6 resolves the discussion about the different models of the Si(111)-(5×2)-Au reconstruction. Finally, in Chapter 7, possibilities to make use of the enormously improved computational power in the last decades within LEED intensity calculations are discussed.

2. Physical Foundations

In this chapter, first, the experimental technique of low-energy electron diffraction (LEED) is presented. In the following, the theoretical background necessary for this thesis as well as insights into the description of the interaction of electrons with surfaces are given.

2.1. LEED Experiment

After the first observation of electron diffraction at crystal surfaces in 1927 by Davisson and Germer [9], expectations were high that electron diffraction would reiterate the successful path of X-ray diffraction with the first experiment in 1912 by von Laue followed by the first structural analysis in 1913 by Bragg [10]. But it took more than forty years until Pendry had success in the description of strong atomic scattering while introducing a perturbation scheme to manage the multiple scattering [11]. Since then, numerous structures have been solved using LEED. Nowadays, LEED has become a standard tool for UHV laboratories due to its relatively easy experimental access to structural properties of crystalline surfaces. The high surface sensitivity of LEED electrons, caused by the low inelastic mean free path in the order of only a few nanometers independent from the specific surface [12], makes it a valuable tool in the examination of surfaces. The information about the surface that can be derived from the reflexes of the diffraction pattern can be roughly split into three groups: Periodicities and symmetries can be obtained from the position, details of the morphology may be derived from the spot profiles, and atomic positions can be inferred from the intensity distribution. The latter point is the main focus of this thesis.

2.1.1. Setup

Due to the short mean free path of electrons at ambient pressure, a LEED optics can only operate in a vacuum environment. A schematic sketch of a typical three-grid LEED optics is depicted in Figure 2.1. An electron gun generates an electron beam that is accelerated by a voltage U_B and focused by electrostatic lenses, located in the center of a hemispherical screen. The diffracted electrons need to overcome a potential step, which is created by a voltage slightly less than U_B at the grids, to reach the screen, preventing the detection of inelastically scattered electrons. Finally, the voltage U_S accelerates the diffracted electrons onto the screen to cause luminescence. The first and third grid as well as the sample are grounded to ensure a field-free space between the sample and the grids. The camera, mounted on the outside of the UHV chamber at a view port, records the diffraction pattern from

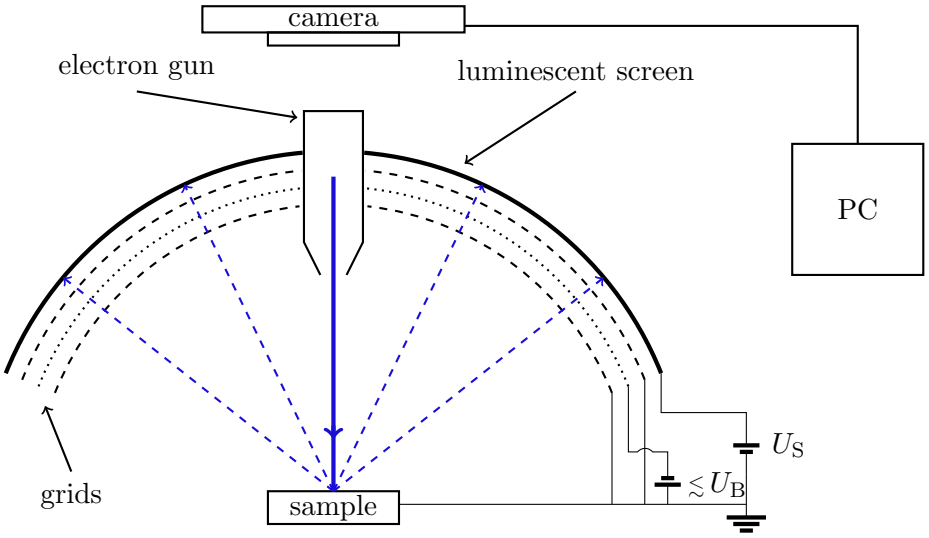

Figure 2.1.: Schematic sketch of a three-grid LEED optics with an external camera to capture the diffraction pattern digitally. The optics is located inside a UHV chamber, while the camera is mounted on the outside of a view port. The electron gun generates and focuses an electron beam, while the voltages U_B and U_S shield the screen from inelastically scattered electrons and accelerate the elastically scattered electrons to illuminate the screen, respectively. A computer is used to control the voltages and record the resulting diffraction patterns for further analysis.

behind the electron gun. A computer can be used to control the acceleration voltage U_B and to record the diffraction patterns for an energy range in an automated process.

Typical beam sizes on the surface lie in the order of magnitude of $1\,\mathrm{mm}^2$, implying that an incredible high number of atoms is probed simultaneously. This makes, on the one hand, the demand that the surface must be prepared carefully, so the beam is not diffracted at different surface structures, making the interpretation of the diffraction pattern difficult. On the other hand, the large beam sizes in LEED are beneficial for the purpose of structural analysis in contrast to local probing techniques like STM, since the results are obtained from a significantly greater area and are therefore insusceptible for random local deviations.

However, due to non ideal conditions in a real experiment, like the finite size of the electron cathode, a distribution of the energy of the LEED electrons caused by their thermionic emission and an angular opening of the beam, the coherence of the probing electron is limited, leading to an *instrumental transfer width* of approximately 100 Å [10]. Therefore, the observed diffraction pattern is an incoherent superposition of the diffraction processes occurring within these approximately 10^{10} coherent areas of the electron beam. Furthermore, due to the strong attenuation of LEED electrons within the surface, those coherent areas can be further divided into regions with a size of approximately 10 Å, which define scattered amplitudes [10].

Requirements on the setup

To perform a successful LEED experiment for structural analysis, some requirements on the setup should be considered to not impair the quality of the experimental data. Most importantly, an ultra high vacuum (UHV) chamber is necessary to operate the LEED optics and furthermore to minimize influences on the surface structure due to contaminations from the gas phase. Besides the careful preparation of the surface structure under investigation, the possibility to place the sample without constraints in front of the LEED optics, so that the angle of incidence of the electron beam is perpendicular to the surface, is desirable. This requires three degrees of freedom for linear motion as well as two degrees of freedom for the rotation of the sample. Already small inaccuracies in the angle of incidence in the magnitude of 1° have a serious influence on the spectra [13]. Furthermore, it is advisable to be able to cool the sample to decrease the background in the diffraction pattern. The thermal influence is caused by vibrational motion of the atoms (cf. section 2.3.5), making the constructive diffraction condition (cf. section 2.2.4) increasingly diffuse. Through cooling, the details in the spectra get much more distinct [13], which improves the evaluation of data.

2.1.2. Data evaluation

In principle, it would suffice to evaluate the relative intensities of the different beams at one energy to deduce the underlying geometrical structure. However, due to the loss of phase information upon the measurement of intensity (which is proportional to the squared modulus of the diffracted electrons wave function), a direct calculation of the structure from the diffraction pattern is not possible in general. Furthermore, hardly controllable influences in the experiment (uneven sensitivity of the screen, etc.) and the high amount of geometrical parameters make it advisable to collect a huge data set to support the fitting of many parameters and to diminish the influence of some experimental inaccuracies. For this purpose, the intensity as a function of the electron energy of a given reflex ($I_{(E)}$ or IV spectra) is used for the analysis. To obtain these IV spectra, the recorded collection of two-dimensional diffraction patterns at different energies needs further evaluation.

The intensity of a single reflex at a certain energy can be extracted with two circular regions of interest (ROI) as depicted in Figure 2.2. This allows the subtraction of the local background intensity to achieve more accurate measured values. Repeating this procedure for all beams and all recorded energies yields a set of IV curves. These can then be compared to IV curves acquired by dynamical scattering theory calculations. If the experimental spectra match the calculated ones very well, it can be assumed that the structure given as input to the calculation is in accordance with the real structure of the atoms in the experiment. Thus, by variation of the input for the calculations, it is tried to achieve the best possible fit between experiment and theory.

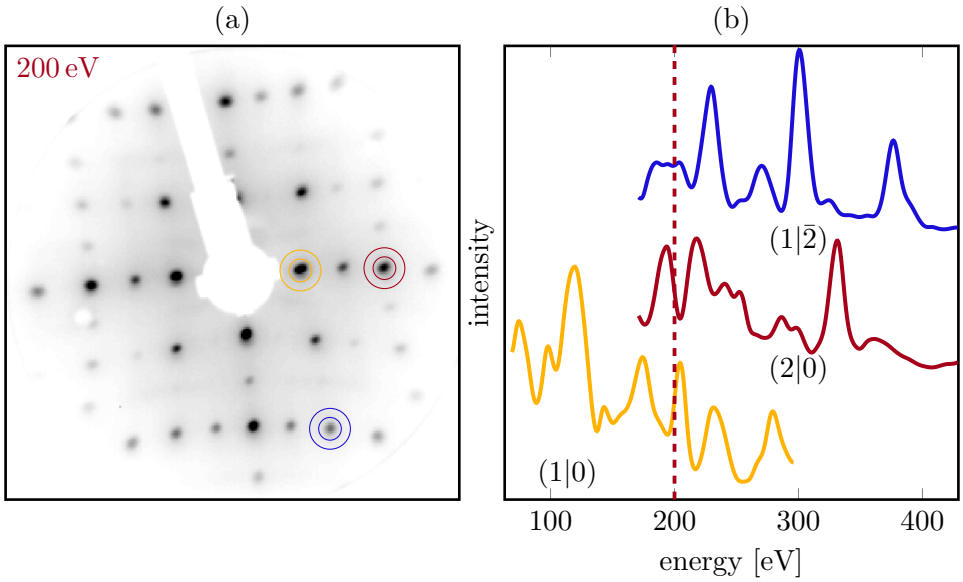

Figure 2.2.: (a) Diffraction pattern recorded at an electron energy of 200 eV. Three exemplary reflexes are encircled with ROIs, used to evaluate intensities. (b) Resulting IV spectra of the evaluated beams. The spectra are shifted along the ordinate for improved visibility. The electron energy used for the diffraction pattern in (a) is denoted by a red dashed line.

Reliability factor

This trial and error approach requires an automated quantitative comparison between calculated and experimental spectra to facilitate the evaluation of many trial structures. For this purpose a reliability factor that yields a single number as a measure for the agreement between calculated and experimental spectra is used. As can be seen in Figure 2.2 (b), IV spectra consist of multiple peaks with varying intensity. The positions of those numerous maxima are determined by multiple scattering and are therefore sensitive to geometrical changes. By contrast, the absolute intensity of those peaks is also dependent on thermal effects and data evaluation. The Pendry reliability factor R_P [14] sets emphasis on the positions of extrema, while being comparably insensitive to relative intensities. To calculate R_P, the logarithmic derivative

$$L_{(E)} = \frac{\mathrm{d}}{\mathrm{d}E} \ln(I) = \frac{\frac{\mathrm{d}I}{\mathrm{d}E}}{I} \tag{2.1}$$

is determined to obtain a function independent of the absolute intensity. Via the definition of the Y-functions according to

$$Y_{(E)} = \frac{L^{-1}}{(L^{-2} + V_\mathrm{i}^2)} \ , \tag{2.2}$$

with V_i being the imaginary part of the inner potential, the Pendry R factor is defined as

$$R_\mathrm{P} = \frac{\sum_g \int (Y_{g,\mathrm{theo}} - Y_{g,\mathrm{exp}})^2 \, \mathrm{d}E}{\sum_g \int (Y_{g,\mathrm{theo}}^2 + Y_{g,\mathrm{exp}}^2) \, \mathrm{d}E} \, . \tag{2.3}$$

Here, the summation is done over all g measured beams to form a weighted average of the R-factors of individual spectra. The denominator is used for normalization. Thus, $R_\mathrm{P} = 1$ if there is no correlation between the theoretical and experimental spectra. If $R_\mathrm{P} = 0$, the spectra are identical, while $R_\mathrm{P} = 2$ results if there is an anti-correlation. When $R_\mathrm{P} < 0.2$, it is usually assumed to have found the correct structure [15].

While the reliability factor is a measure of the agreement between calculated and experimental spectra, it does not make an estimation about the significance of this agreement with respect to the number of free parameters in the structure model. To analyze whether a R_P value can result by chance, the assumption is made that the IV spectra consist of closely packed Lorentzian-shaped peaks with widths defined by the imaginary part of the inner potential V_i. This leads to the estimation of $N = E_\mathrm{T}/(4|V_\mathrm{i}|)$ measured peaks that can be found in the total energy range E_T of all spectra [14]. Therefore, the redundancy ρ

$$\rho = \frac{N}{f} = \frac{E_\mathrm{T}}{4|V_\mathrm{i}| \; f} \tag{2.4}$$

approximates the ratio between significant structures found in the spectra and the number of free parameters f used to simulate the spectra. A value of $\rho < 1$ means *over-fitting*, since the use of more parameters than sampling points is expected to yield a fit matching those points. However, when performing a structure optimization with LEED, an increase in parameters can mainly be done by the inclusion of more reconstructed layers. Due to the attenuation of the LEED electrons, those additional parameters have only a reduced impact on the spectra. However, a high redundancy is desirable for a conclusive analysis.

Furthermore, to estimate the errors in the determination of the values for the respective parameters, the variance of R_P ($\mathrm{Var}(R_\mathrm{P}) = R_\mathrm{P,min}\sqrt{8|V_\mathrm{i}|/E_\mathrm{T}}$) deduced from the minimum of the Pendry R factor $R_\mathrm{P,min}$ can be used [14]. It can be assumed that a given parameter lies with the confidence of one standard deviation within the range for which $R_\mathrm{P} \leq R_\mathrm{P,min} + \mathrm{Var}(R_\mathrm{P})$ is fulfilled under the variation of this parameter.

Smoothing

One issue with the Pendry R factor is its sensitivity to high-frequency noise, which can be found in experimental spectra, due to non-perfect experimental conditions (varying electron beam flux, non-even efficiency of the luminescence screen, etc.) and inaccuracies in measurement and data evaluation (quality of the recording camera,

intensity extraction from two-dimensional diffraction patterns, etc.). To ensure a reliable comparison between calculated and experimental spectra, smoothing of the curves is a necessity. The CLEED package [16] used in this thesis for the calculation of IV spectra uses, as proposed by Pendry [14], the convolution of the IV spectra with a Lorentzian according to

$$I'_{(E)} = \frac{1}{\pi} \int \frac{I_{(E')}\ \kappa}{(E - E')^2 + \kappa^2}\ \mathrm{d}E' \tag{2.5}$$

for smoothing purposes. The parameter κ should be equal to or lesser than the imaginary part of the inner Potential V_i to avoid loss of information. Within this thesis, $\kappa = 4\,\mathrm{eV}$ was used. This smoothing alters the spectra significantly, but it retains the position of the peaks. Hence, it must be applied to experimental as well as calculated spectra to enable a meaningful comparison.

Due to the use of the logarithmic derivative in the calculation of R_P, negative intensities in the experimental spectra (which can happen in regions of very low intensity) lead to a sign change, which affects the reliability factor immensely. Furthermore, since the logarithmic derivative is not defined for zero intensity, experimental spectra must be corrected in regions of low intensity to fulfill these demands.

2.2. Periodical Surface Structures

In this section, the basic theoretical concepts necessary to understand diffraction at crystalline surfaces are presented.

2.2.1. Crystals and surfaces

In solid state physics, a strict distinction is made between the solid and its surface. Many properties of the solid are based on its periodicity, which is present in every spatial direction. It is thus composed of repeating unit cells, which do not differ from each other. This arrangement can be conceived as a space lattice. For the mathematical description of the lattice, the translation vector $\mathbf{r}_\mathrm{crystal}$ is introduced, which can reach any one point of the lattice from any other point of the lattice

$$\mathbf{r}_\mathrm{crystal} = n_1\mathbf{a}_\mathrm{c} + n_2\mathbf{b}_\mathrm{c} + n_3\mathbf{c}_\mathrm{c} \qquad \text{with } \{n_1, n_2, n_3\} \in \mathbb{Z}\ , \tag{2.6}$$

with the linearly independent lattice vectors $\mathbf{a}_\mathrm{c}$, $\mathbf{b}_\mathrm{c}$, and $\mathbf{c}_\mathrm{c}$ that span the unit cell. For the description of crystal structures, it is necessary to consider a basis. Conveniently, the reference point of the lattice is placed in the center of a basis atom. If the unit cell contains more than one atom, the relative coordinates of the atoms $\mathbf{r}_\mathrm{B}$ with respect to the origin of the basis are given. In Figure 2.3 (a) a schematic sketch of a lattice with a basis consisting of two atoms is shown.

To describe planes within a crystal, Miller's indices are used. They are calculated from the reciprocals of the numbers n_1, n_2, and n_3 at which the plane intersects the respective axes. These reciprocals are then multiplied by their least common

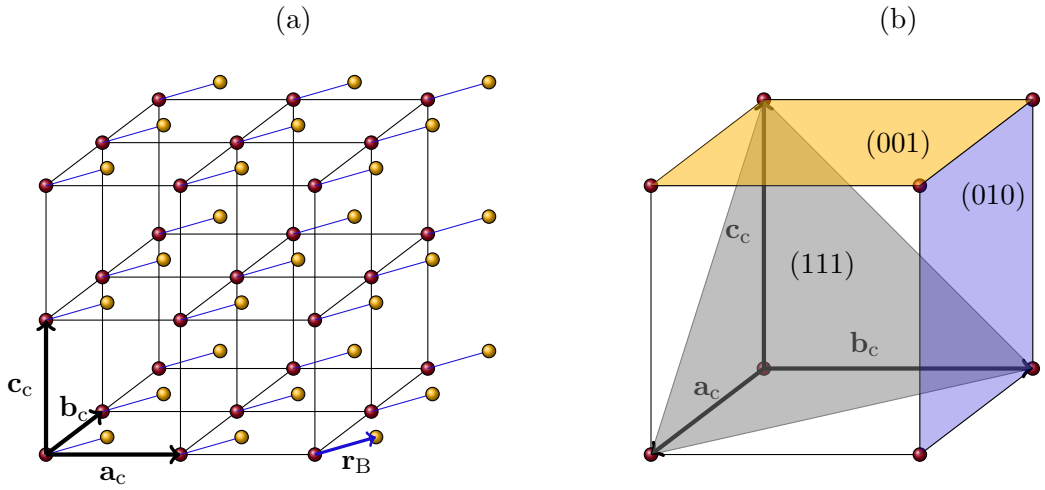

Figure 2.3.: (a) Crystal lattice with primitive translation vectors $\mathbf{a}_c$, $\mathbf{b}_c$, and $\mathbf{c}_c$. The origin of the reference frame is located at the position of a "red atom". The description of the full basis (red and yellow) is done by means of the vector $\mathbf{r}_B$, which gives the position of the "yellow atom" relative to the reference point. (b) Cubic primitive unit cell. The gray and blue and yellow colored surfaces correspond to the planes with Miller indices (111), (010), and (001), respectively.

multiple to obtain the Miller indices. If there is no intersection with an axis, the corresponding index is 0. Thus, for the plane with the axis intersections 4, 3, and 2, the corresponding Miller indices are (346). In Figure 2.3 (b), three planes with their respective Miller indices are shown as an example. Directions in a crystal, on the other hand, are indicated with square brackets. For cubic lattices, a direction with the same indices as a plane is perpendicular to this plane.

At the surface, the translational invariance of the lattice is broken in one spatial direction. Therefore, two translation vectors suffice to describe the periodicity. Furthermore, unsaturated bonds at the surface can cause a reconstruction of the surface atoms, which minimizes the total energy of the system. The resulting reconstructed surface may differ from an equivalent plane in the solid by a change in translational symmetry. For this reason, a separate translation vector $\mathbf{r}_{\text{surf}}$ is introduced for the lattice of the surface, which is composed of two lateral primitive translation vectors

$$\mathbf{r}_{\text{surf}} = m_1\mathbf{a} + m_2\mathbf{b} \qquad \text{with } \{m_1, m_2\} \in \mathbb{Z}\ . \tag{2.7}$$

The parallelogram spanning the vectors $\mathbf{a}$ and $\mathbf{b}$ is called the lateral unit cell. In addition, to fully describe a two-dimensional structure, a basis with multiple atoms may need to be considered. Instead of the 14 Bravais lattices used to classify different three-dimensional crystal structures, the surface can be described by five Bravais lattices that are depicted in Figure 2.4.

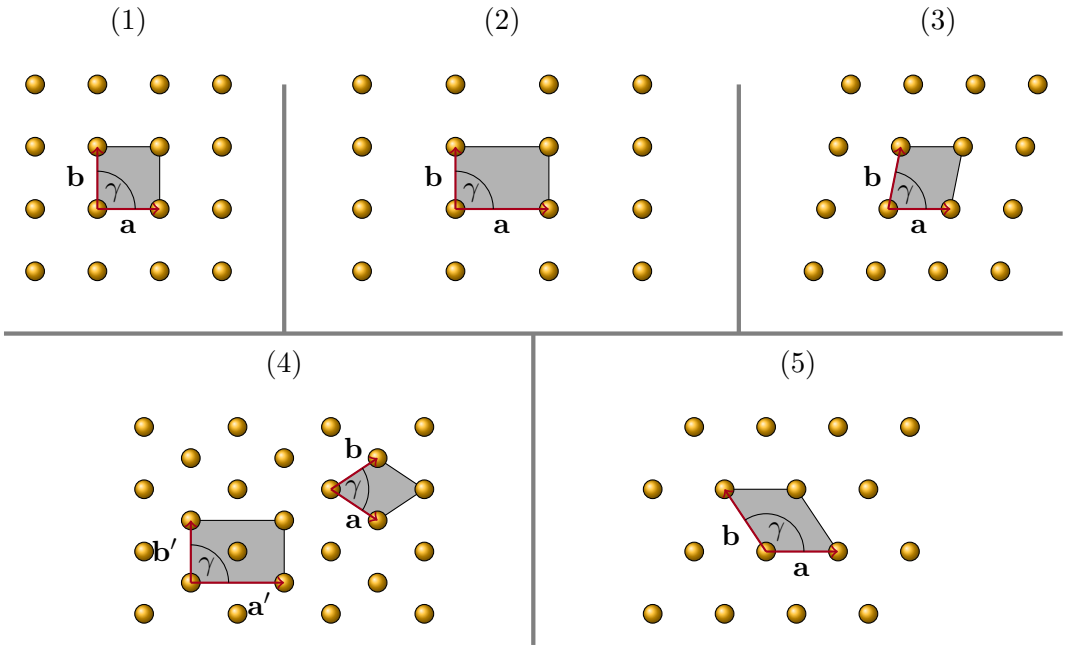

Figure 2.4.: The 5 Bravais lattices for two-dimensional structures:
(1) square $|\mathbf{a}| = |\mathbf{b}|$; $\gamma = 90°$,
(2) rectangular $|\mathbf{a}| \neq |\mathbf{b}|$; $\gamma = 90°$,
(3) oblique $|\mathbf{a}| \neq |\mathbf{b}|$; $\gamma \neq 90°$,
(4) centered rectangular $|\mathbf{a}| = |\mathbf{b}|$; $\gamma \neq 120°$,
(5) hexagonal $|\mathbf{a}| = |\mathbf{b}|$; $\gamma = 120°$.
For the centered rectangular lattice, a primitive and a non-primitive lattice are shown. The non-primitive lattice is commonly used due to its convenience of description.

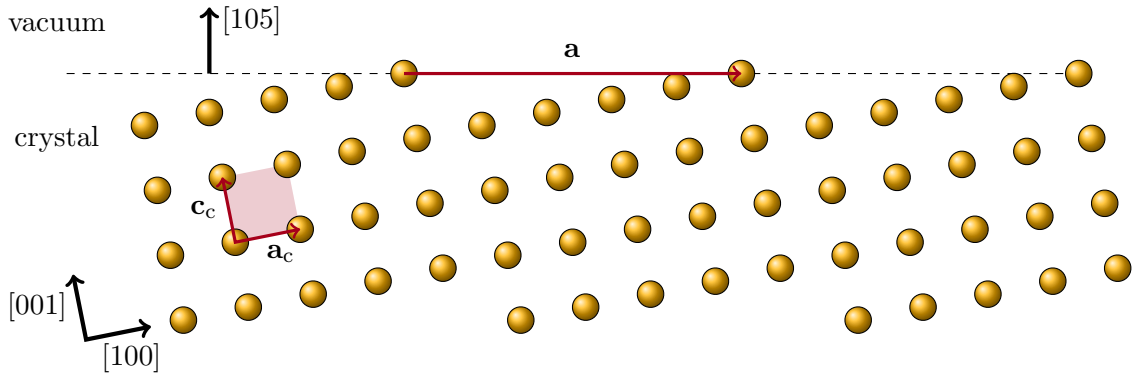

Figure 2.5.: Example of a vicinal surface of a cubic crystal with the Miller indices (105). The lattice vectors of the crystal are denoted by $\mathbf{a}_c$ and $\mathbf{c}_c$, respectively. The relatively small angle of about 11.31° toward the highly symmetric (001) plane leads to a surface exhibiting terraces with (001) orientation separated by periodic atomic steps. The surface translation vector $\mathbf{a}$ is significantly greater than the translation vectors of the crystal.

Vicinal surfaces

In the case of cutting a crystal along a plane that has an angle of a few degrees toward a plane with low Miller indices (thus being highly symmetric), a so-called *vicinal surface* is created. While not being a special case regarding the previous definitions, the resulting planes described by high Miller indices have characteristics that differentiate them from surfaces with low Miller indices. Figure 2.5 displays a schematic sketch of the (105) and thus vicinal surface of a simple cubic crystal. The angle of about 11.31° toward the highly symmetric (001) plane leads to a surface, which exhibits terraces that are analogously to a pristine (001) surface but separated by periodic mono-atomic steps. This leads to a significantly increased length of the lateral translation vector $\mathbf{a}$ compared to the translations of the bulk $\mathbf{a}_c$. The asymmetry of the surface induced by the steps creates different adsorption sites, making vicinal surfaces especially interesting for self-induced reconstructions. Furthermore, they can act as a template guiding the growth direction of nanowires if the growth is constrained by the steps to only one dimension.

2.2.2. Superstructures

Due to unsaturated bonds of the surface or the interaction with adsorbates, surfaces can reconstruct and thus exhibit periodicities deviating from those of the bulk. Figure 2.6 displays a rectangular lattice with a superstructure induced by additional atoms. The usual notations for describing superstructures link the primitive lattice vectors of the superstructure to the primitive lattice vectors of an underlying unreconstructed plane of the solid with the lateral translation vectors $\mathbf{a}$ and $\mathbf{b}$.

In matrix notation, the relationship between the translation vectors of the sub-

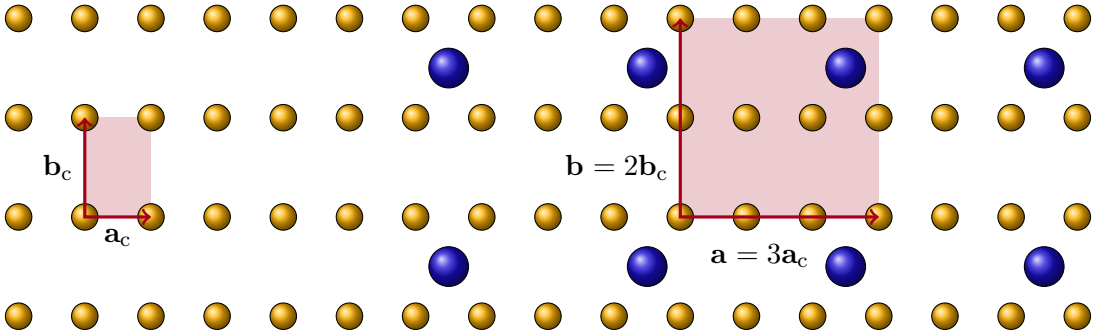

Figure 2.6.: Example for the creation of a superstructure. On the left, a rectangular lattice with the translation vectors $\mathbf{a}_c$ and $\mathbf{b}_c$ can be seen. On the right, the additional blue spheres induce a deviating periodicity of the surface with the translation vectors $\mathbf{a}$ and $\mathbf{b}$.

strate and the translation vectors of the superstructure is denoted by

$$\mathbf{a} = G_{11}\mathbf{a}_c + G_{12}\mathbf{b}_c \qquad \mathbf{b} = G_{21}\mathbf{a}_c + G_{22}\mathbf{b}_c \ . \tag{2.8}$$

The superstructure is then given by the matrix

$$\underline{G} = \begin{pmatrix} G_{11} & G_{12} \\ G_{21} & G_{22} \end{pmatrix} . \tag{2.9}$$

By contrast, Wood's notation, considers the ratio of the lengths of the translation vectors

$$\frac{|\mathbf{a}|}{|\mathbf{a}_c|} = m \qquad \frac{|\mathbf{b}|}{|\mathbf{b}_c|} = n \ . \tag{2.10}$$

The superstructure in this notation is given as $X(hkl)c(m \times n) - R\varphi - Ad$, where hkl corresponds to the Miller indices of the surface of the substrate X. A rotation between the base translation vectors of the substrate and the superstructure is indicated by the angle φ, if applicable, while any centering is represented by a c (e.g., Si(001)$c(4 \times 2)$). If the superstructure is induced by adsorbate atoms, Ad is replaced by the corresponding chemical symbol with the number of adsorbate atoms present in a unit cell (e.g., Si(111)$(\sqrt{3} \times \sqrt{3}) - R30°-$3Bi). It should be noted that Wood's notation, unlike the matrix notation, can only be used correctly if the angle between the translation vectors of the substrate is equal to the angle between the translation vectors of the superstructure. For example, the superstructure shown in Figure 2.6 can be described as $\begin{pmatrix} 3 & 0 \\ 0 & 2 \end{pmatrix}$ with the matrix notation, or as (3×2) in Woods notation.

Domains

On real surfaces, if a superstructure is induced, the formation of different domains can be typically observed. Within each domain, the periodicity of the superstructure

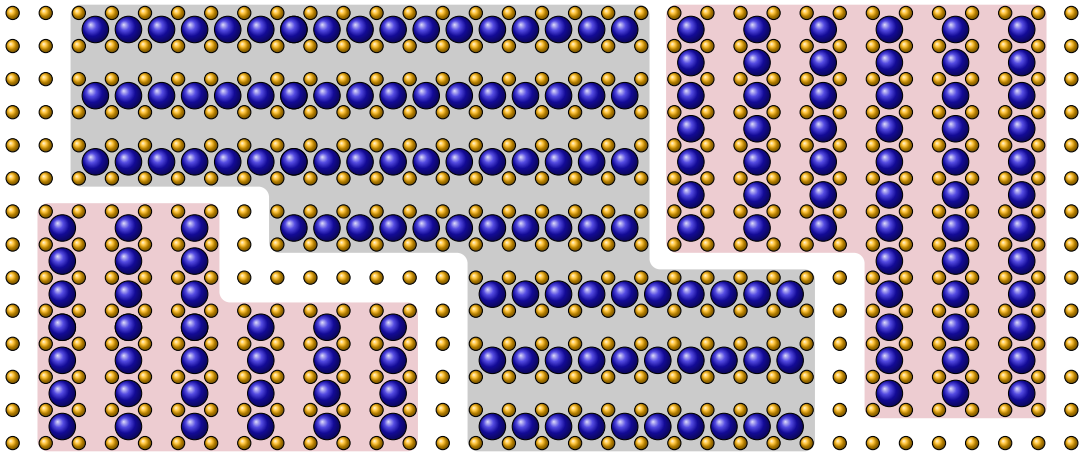

Figure 2.7.: Schematic sketch of a surface covered by different (rotational) domains. The addition of blue spheres on the surface with a square unit cell (yellow spheres) forms a superstructure, whereby two different alignments are supported. The (2×1) reconstruction highlighted in red and the (1×2) reconstruction highlighted in gray (rotated by 90°) form different rotational domains. The intensity observed in the diffraction pattern is an incoherent superimposition of the different domains.

is well defined. However, at domain boundaries the long range order is broken. For a LEED experiment, if the domains are sufficiently large, it can be assumed that the influence of the domain boundaries in the diffraction pattern is negligible. Then, due to the limited transfer width, the diffraction pattern consists of the incoherent superposition of the contribution of the different domains.

Domains can be classified into different types. Anti-phase domains occur when the periodicity of the superstructure is shifted by half a lattice constant at domain boundaries, which can lead to the extinction of reflexes. Another type of domains are rotational domains, which can be observed when different alignments of a superstructure are supported by the substrate. A schematic sketch of a surface covered by rotational domains is depicted in Figure 2.7. The superimposition of those rotational domains in the diffraction pattern can lead to additional reflexes with regard to the consideration of a single domain. Thereby, the superimposed diffraction pattern can exhibit a higher symmetry than the superstructure, making the averaging of the intensity of calculated beams necessary for a comparison with experimental spectra.

2.2.3. Reciprocal space

The reciprocal space is a concept that is very useful when using diffractive measurement methods such as LEED. Thereby, each lattice describing the periodicity of a surface structure is assigned to a reciprocal lattice. This reciprocal lattice can be

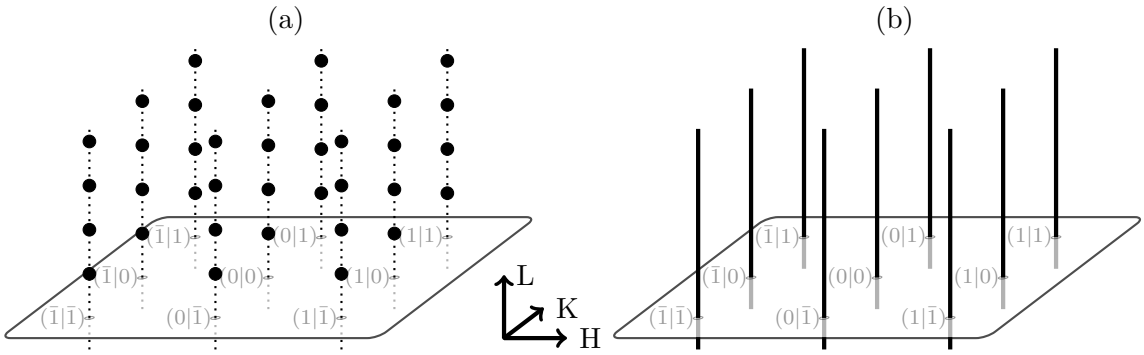

Figure 2.8.: (a) Schematic representation of the reciprocal space for a three-dimensional crystal lattice with a cubic unit cell. (b) Schematic representation of the reciprocal space for a two-dimensional crystal lattice with square unit cell. While the reciprocal space of the three-dimensional crystal consists of points, the reduced translation symmetry of the surface results in reciprocal lattice rods for the two-dimensional crystal.

described analogously to equation (2.7) by

$$\mathbf{G}_{\parallel} = h\mathbf{a}^* + k\mathbf{b}^* \qquad \text{with } \{h,k\} \in \mathbb{Z}\ , \tag{2.11}$$

where $\mathbf{a}^*$ and $\mathbf{b}^*$ are the reciprocal translation vectors of the reciprocal lattice. The subscript of $\mathbf{G}_{\parallel}$ indicates that the lattice lies within the plane of the surface. The reciprocal translation vectors are obtained from the translation vectors of the real space lattice according to

$$\mathbf{a}^* = 2\pi \cdot \frac{\mathbf{b} \times \mathbf{n}}{|\mathbf{a} \times \mathbf{b}|} \qquad \mathbf{b}^* = 2\pi \cdot \frac{\mathbf{n} \times \mathbf{a}}{|\mathbf{a} \times \mathbf{b}|}\ , \tag{2.12}$$

where $\mathbf{n}$ is a unit vector perpendicular to the surface. Thus, the dimension of the reciprocal translation vectors is $[\frac{1}{\text{length}}]$. Notably, $\mathbf{a}$ is perpendicular to $\mathbf{b}^*$ and $\mathbf{b}$ is perpendicular to $\mathbf{a}^*$. Furthermore, the scalar products $\mathbf{a} \cdot \mathbf{a}^*$ and $\mathbf{b} \cdot \mathbf{b}^*$ yield 2π, respectively. The reciprocal space of a three-dimensional crystal lattice consists of points. For two-dimensional lattices, because of the lack of periodicity, the distance between two lattice points in the vertical direction can be assumed to be infinite, bringing the points in the reciprocal space together to form rods. Figure 2.8 shows the reciprocal space of a three-dimensional and a two-dimensional crystal lattice. The two-dimensional case corresponds to a single layer of the three-dimensional crystal.

However, in a generic diffraction experiment, the surface of three-dimensional crystalline solids is examined. In this case, the unit cell extends from the surface deep into the crystal (cf. Figure 2.9). Although a three-dimensional crystal is examined, strict periodicity can only be found in lateral directions. Therefore, the reciprocal space of a truncated crystal consists of rods as depicted in Figure 2.8 (b).

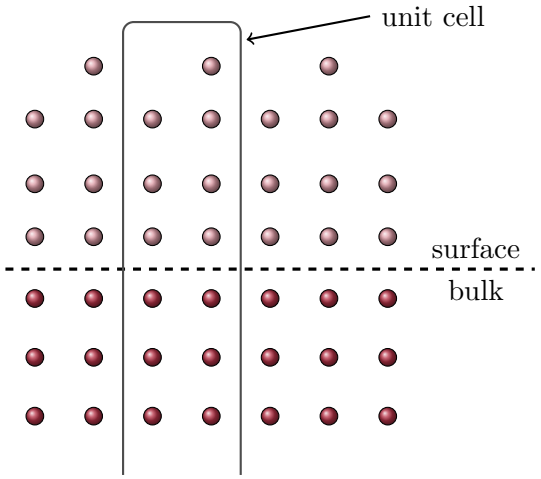

Figure 2.9.: Schematic representation of the unit cell of a surface structure. The surface, in which the positions of the atoms deviate from the crystal lattice sites, and the bulk, in which the atoms are arranged according to the crystal lattice, are to be distinguished. Due to the broken periodicity, the crystal is only in lateral directions strictly periodic. Therefore, the reciprocal space of a truncated crystal consists of rods as depicted in Figure 2.8 (b).

2.2.4. Diffraction on periodical structures

In this part, first, the diffraction condition for periodic surface structures is derived. Subsequently, it is illustrated with the Ewald construction in reciprocal space.

Diffraction condition

According to the wave particle dualism of quantum physics, a de Broglie wavelength can be assigned to the electrons used for diffraction according to

$$\lambda = \frac{2\pi\hbar}{\sqrt{2m_{\mathrm{e}}E}} \ . \tag{2.13}$$

The energy range of approximately 50 eV to 700 eV typically used in LEED corresponds to wavelengths of about 0.5 Å to 1.7 Å, which is the same order of magnitude as typical atomic distances in crystals. Since the distance of the electron source from the sample surface is sufficiently large, the electrons can be treated as plane waves. From Figure 2.10, the condition for constructive interference of two neighboring scattering centers whose position with respect to each other is described by $\mathbf{a}$ can be derived. Constructive interference can be expected if the path difference between the two waves is equal to a multiple of the wavelength λ, which is described by

$$\mathbf{a} \cdot (\mathbf{s} - \mathbf{s}_0) = h\lambda \qquad \text{with } h \in \mathbb{Z} \ , \tag{2.14}$$

where $\mathbf{s}$ and $\mathbf{s}_0$ are unit vectors with the directions of the incident and scattered wave, respectively. For two points whose relative position to each other is described by $\mathbf{b}$ or $\mathbf{c}$, it follows analogously

$$\mathbf{b} \cdot (\mathbf{s} - \mathbf{s}_0) = k\lambda \qquad \text{with } k \in \mathbb{Z} \tag{2.15}$$

$$\mathbf{c} \cdot (\mathbf{s} - \mathbf{s}_0) = l\lambda \qquad \text{with } l \in \mathbb{Z} \ . \tag{2.16}$$

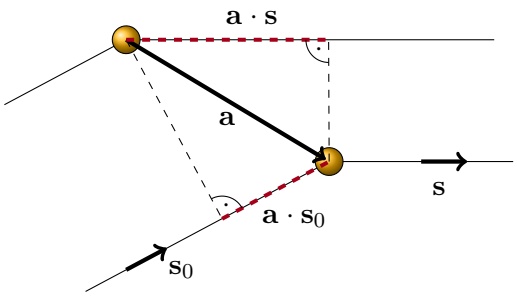

Figure 2.10.: Sketch for the derivation of the diffraction condition of two neighboring scatterers whose relative position to each other is described by $\mathbf{a}$. The vectors $\mathbf{s}$ and $\mathbf{s}_0$ are unit vectors with the direction of the incident and diffracted beam, respectively. From the lengths of the red dashed lines, the path difference can be determined.

For any translation vector of the reciprocal lattice $\mathbf{G} = h\mathbf{a}^* + k\mathbf{b}^* + l\mathbf{c}^*$, the equations (2.14) to (2.16) can be expressed by

$$\mathbf{s} - \mathbf{s}_0 = \frac{\lambda}{2\pi}\,\mathbf{G}\ , \tag{2.17}$$

which is therefore the diffraction condition for a three-dimensional crystal. As a proof, both sides can be multiplied scalar by $\mathbf{a}$, $\mathbf{b}$, or $\mathbf{c}$. Respecting the definition of the reciprocal lattice vectors, the equations (2.14) to (2.16) are obtained. Replacing $\mathbf{s}$ and $\mathbf{s}_0$ by the wavenumber vectors $\mathbf{k}$ and $\mathbf{k}_0$ according to

$$\mathbf{s} = \frac{\lambda}{2\pi}\,\mathbf{k} \qquad \text{and} \qquad \mathbf{s}_0 = \frac{\lambda}{2\pi}\,\mathbf{k}_0 \tag{2.18}$$

and the introduction of the scattering vector $\mathbf{K} = \mathbf{k} - \mathbf{k}_0$ allows to write equation (2.17) as the Laue equation

$$\mathbf{K} = \mathbf{G}\ . \tag{2.19}$$

Thus, constructive interference is expected, when the scattering vector matches a vector of the reciprocal lattice. Since the reciprocal space of a surface consists of rods, the component of $\mathbf{G}$ that is perpendicular to the surface can take any value to satisfy equation (2.17). Thus, only the components of $\mathbf{k}$ and $\mathbf{k}_0$ that are parallel to the surface are important. Therefore, the diffraction condition for a two-dimensional surface is given by

$$\mathbf{k}_\parallel - \mathbf{k}_{0,\parallel} = \mathbf{G}_\parallel\ . \tag{2.20}$$

Ewald construction

Since only elastically scattered electrons are detected in LEED, $|\mathbf{k}| = |\mathbf{k}_0|$ must hold. With this additional condition, equation (2.20) can be illustrated by the Ewald construction as depicted in Figure 2.11.

In conventional LEED, the angle of incidence of the electron beam is typically perpendicular to the sample. For this reason, $\mathbf{k}_0$ is drawn parallel to the diffraction rods so that its tip lies on the (00)-diffraction rod, at the origin of the reciprocal space. A circle of radius $|\mathbf{k}_0|$ is now drawn around the starting point. For the validity

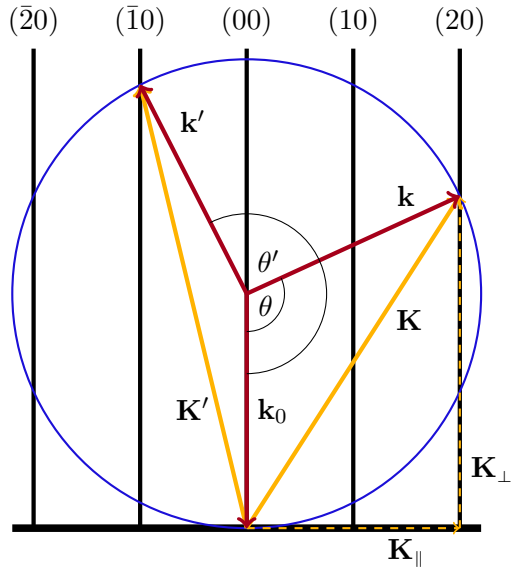

Figure 2.11.: Sketch of the Ewald construction for diffraction on a surface for the two beams $(2|0)$ and $(\bar{1}|0)$ with perpendicular incidence. $\mathbf{k}_0$ points to the origin of the reciprocal space. The two reflexes $(2|0)$ and $(\bar{1}|0)$ can be observed at angles θ and θ', since in these directions the equation (2.20) is satisfied. The scattering vectors $\mathbf{K}$ is also depicted with its components $\mathbf{K}_\parallel$ and $\mathbf{K}_\perp$. For better illustration, only a section through the reciprocal space and the Ewald sphere is shown and further possible diffracted beams are not included.

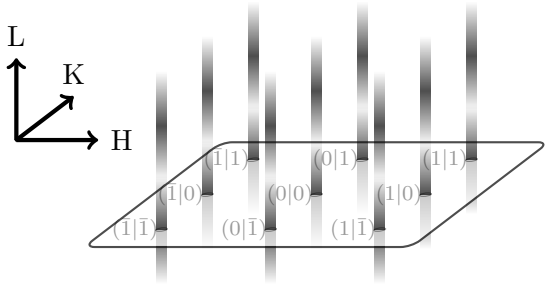

Figure 2.12.: Due to the three-dimensional unit cell, whose periodicity is broken in one spatial direction by the surface, diffraction rods are created in reciprocal space. Here the varying shading of the rods shall symbolize that the observed intensity at different points on the rods is not constant.

of equation (2.20), only the components of the vectors $\mathbf{k}_0$ and $\mathbf{k}$, which are parallel to the surface, are important. Thus, the equation is always satisfied if $\mathbf{k}$ runs from the starting point of $\mathbf{k}_0$ to an intersection of the circle with the diffraction rods. Hence, these are the directions in which reflections are to be expected in the diffraction experiment.

The used energy for the electron beam and its angle of incident on the surface determine at which points the Ewald sphere intersects with the reciprocal lattice rods. This can be used to measure along the reciprocal lattice rods. The atomic structure of the surface within the three-dimensional unit cell determines which intensity can be expected at each point of the reciprocal lattice rod. Figure 2.12 shows the reciprocal space of a surface consisting of rods. However, the atomic structure causes a variation in observed intensity, depending which point of the rod is probed in a diffraction experiment. Here, this is visualized by a varying shading of the rods. Conversely, the intensity distribution along the rods can be used to infer the atomic structure.

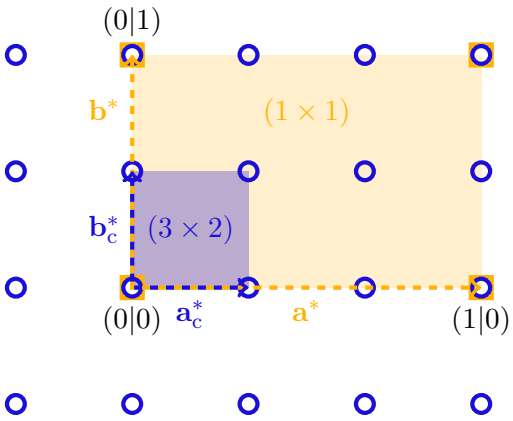

Figure 2.13.: Schematic part of the diffraction pattern of the superstructure depicted in Figure 2.6, as it would be observed in a LEED experiment. The reflexes originating from the substrate (yellow spheres) are depicted with yellow squares, while the reflexes originating from the superstructure are depicted with blue circles. Due to the larger translational vectors in real space, the reflexes of the superstructure are closer in reciprocal space.

Connection to observable LEED pattern

In a LEED experiment, the diffraction patterns that can be observed on the luminescent screen can be interpreted as a view onto the Ewald sphere (along the direction of $\mathbf{k}_0$). Thus, the reflexes on the screen correspond to the intersections of the diffraction rods with the Ewald sphere. Therefore, varying the energy of the electron beam (and hence the length of $\mathbf{k}_0$) allows the evaluation of the diffraction rods at different positions, while the pattern of reflexes does not change. Furthermore, at higher energies and thus a larger radius of the Ewald sphere, more beams become accessible. Figure 2.13 displays the diffraction pattern of the superstructure from Figure 2.6. As can be seen, the LEED pattern allows a direct inference on the relation of the translational vectors of the substrate and the superstructure. Additionally, the positions of the reflexes allow a direct inference on the surface lattices (here, a rectangular lattice and a square superstructure).

2.2.5. Symmetries

Additional to the five Bravais lattices, which characterize the different possible translations, further symmetries can be found on real surfaces. These include rotations, reflections and glide reflections, which occur depending on the arrangement of the atoms within the unit cell. For two-dimensional patterns 17 so-called *wallpaper groups* exist to describe the symmetry operations possible. The two groups relevant within this thesis are *pm* and *p2mm*, which are depicted in Figure 2.14. The *p* followed by a number indicates rotational symmetry, meaning a pattern containing *p2* symmetry can be rotated by 360°/2 without changing its appearance. The number of *m*s (and eventually *g*s) denotes the possible (glide) reflections. Due to the additional reflection axis, the *p2mm* has therefore a higher symmetry. The intersection of the perpendicular reflection axes acts as a rotational center of order 2 (180°).

Applied to surface structures, these symmetry operations can be used to reduce the number of free geometrical parameters in a structural optimization. While an atom located on a reflection plane can only move on this plane, two atoms on opposite sides of such a plane must conserve symmetry and are hence bound to mirror each

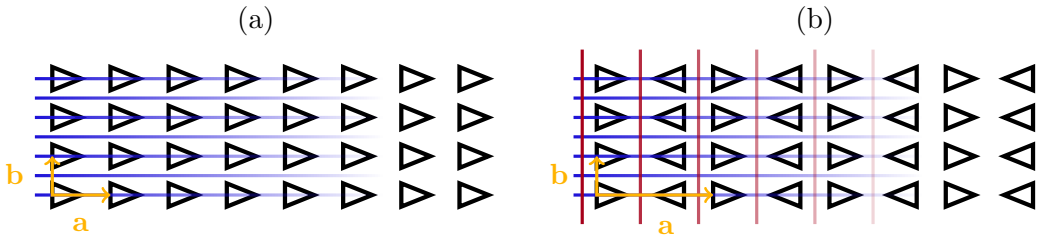

Figure 2.14.: (a) Example for a pattern with *pm* symmetry. (b) Example for a pattern with *p2mm* symmetry. The blue lines denote horizontal reflection axes, while the red ones denote vertical reflection axes, which are not present in (a). The intersections of reflection axes are also rotational centers of order 2 (180°). Translational vectors are denoted in yellow.

others position.

These symmetries in real space can also be found in reciprocal space in the diffraction pattern. Therefore, on surface with symmetries, reflexes with identical IV spectra are expected. For a LEED analysis, these symmetries can be exploited by averaging equivalent spectra, thus reducing noise. Furthermore, small inaccuracies like a deviation from a perpendicular perpendicular incidence can be partly compensated.

2.3. LEED Theory

In this section, the essential ingredients for a successful description of the scattering of electrons on crystalline surfaces are presented. Historically, the kinematic scattering theory had great success in the explanation of diffraction experiments using X-rays. Within the kinematic scattering theory, it is assumed that every probing particle gets scattered elastically exactly one time. However, it could not explain the intensity spectra observed with the diffraction of electrons. This is mainly due to the fact that in LEED, multiple scattering plays a dominant role and leads to additional smaller peaks in the spectra between those that can be explained kinematically. The kinematic scattering theory can be extended by many aspects that are necessary for a successful description of electron diffraction like the correct scattering of electrons at atoms, temperature effects, and the inner potential, whereby the agreement with experimental spectra can be improved. Nonetheless, the inclusion of multiple scattering events is essential to simulate LEED spectra. Hence the introduction of a *dynamical scattering theory* was inevitable.

2.3.1. Surface of a one-dimensional crystal

To explain the concepts and parameters used in a full dynamical calculation, it is helpful to start with a model of an one-dimensional crystal, placing scatterers periodically along one axis in only one direction ($z < 0$) with the spacing d as shown schematically in Figure 2.15 (a). The incident electron wave can be described by e^{-ikz}, with the wave vector k being connected to the de Broglie wavelength by $k = \frac{2\pi}{\lambda}$. The most basic approximation of the amplitude of the scattered wave is the summation of each wave reflected by exactly one of these atoms. This leads to a phase shift e^{i2kz_i} between these reflected waves, depending on the position z_i of those atoms causing interference. The factor 2 is due to the way from the surface to the atom and then back.

Figure 2.15 (b) depicts the energy-dependent intensity, which is the square of the (probability) amplitudes. For most energies, the resulting intensity is low, but when a multiple of the wavelength equals to the atomic distance d, peaks with high intensity can be observed, since all scattered waves interfere constructively. An increase in the number of atoms N used to model this surface causes an increasing intensity of the peaks, getting also sharper. However, this description does not fit electron diffraction, since they have a short mean-free path due to their large scattering cross sections with atoms. Therefore, it is necessary to limit the penetration depth of the electrons. This can be done by the introduction of an imaginary potential V_i within the crystal. Hence, the wave vector of the electron itself becomes complex, causing a dampening of the amplitude as the wave propagates inside the crystal. This leads also to a broadening of the reflexes, although no intermediate peaks can be observed (now it does not matter if the surface consists of 100 or 1000 atoms, since the electrons can not reach deep enough into the crystal) as can be seen in Figure 2.15 (b). Notably, the peak intensity increases now with increasing energy

due to weaker dampening at higher energies within this approach of an imaginary part of the potential. Additionally, a real part of the potential V_r leads to a shift of the whole spectra. This potential step causes a change in the wavelength of the electron inside the crystal, hence shifting the condition for constructive interference. However, this has not been done here.

Due to the potential around an atom core, the electron is expected to be phase shifted upon scattering. This can be qualitatively understood by the acceleration an electron experiences when approaching the atom core. This increase in kinetic energy shortens its wavelength momentarily. Hence, when leaving the atom, its phase is advanced compared to the propagation without the atomic potential. This effect changes the conditions for constructive interference to lower energies, since the optical path has been lengthened as can be seen in Figure 2.15 (d). However, the inclusion of multiple scattering does not alter the IV spectra otherwise, since all possible path differences of the electron are also included in the kinematic model. Notably, this is not the case for scattering on a two or three-dimensional crystal.

The introduction of a relaxed surface (changing the positions of the top 4 layers slightly) does change the spectra immensely, as is depicted in Figure 2.15 (e). The peaks from the non-reconstructed case still exist, but many additional peaks emerge and their intensities are no more easily predictable.

Peak width

As can be seen in Figure 2.15 (b), the width of the peaks increases in the kinematic approach by reducing the number of scatterers as well as by the use of an imaginary potential (cf. Figure 2.15 (c)). Therefore, the imaginary part of the potential effectively limits the penetration depth of the electrons into the surface. The electron wave inside a surface with an imaginary potential V_i can be described by

$$e^{ikz} = e^{i\frac{z}{\hbar}\sqrt{2m_e(E+V_\mathrm{i})}} \qquad \text{with } k = \frac{\sqrt{2m_e(E+V_\mathrm{i})}}{\hbar} \ . \tag{2.21}$$

To illustrate the effect of V_i, the approximation with the first two terms of the Taylor series of $\sqrt{E+x} = \sqrt{E} + \frac{x}{2\sqrt{E}} + \dots$ leads to

$$e^{ikz} \approx e^{i\frac{z}{\hbar}\sqrt{2m_e}\left(\sqrt{E}+\frac{1}{2\sqrt{E}}V_\mathrm{i}\right)} = e^{ik_r z}\ e^{i\frac{z}{\hbar}\sqrt{2m_e}\frac{V_\mathrm{i}}{2\sqrt{E}}} \ , \tag{2.22}$$

with k_r being the wave vector of the electron within a surface without an imaginary potential. Since $V_\mathrm{i} = i|V_\mathrm{i}|$, this can be rewritten to

$$e^{ikz} \approx e^{ik_r z}\ e^{-\frac{kz}{2E}|V_\mathrm{i}|} \ . \tag{2.23}$$

Thus, the imaginary potential causes an exponential dampening of the amplitude of the electrons. The mean free path Λ is the distance that must be traveled, so the amplitude becomes e^{-1}, so

$$\Lambda = \frac{2E}{k|V_\mathrm{i}|} \ . \tag{2.24}$$

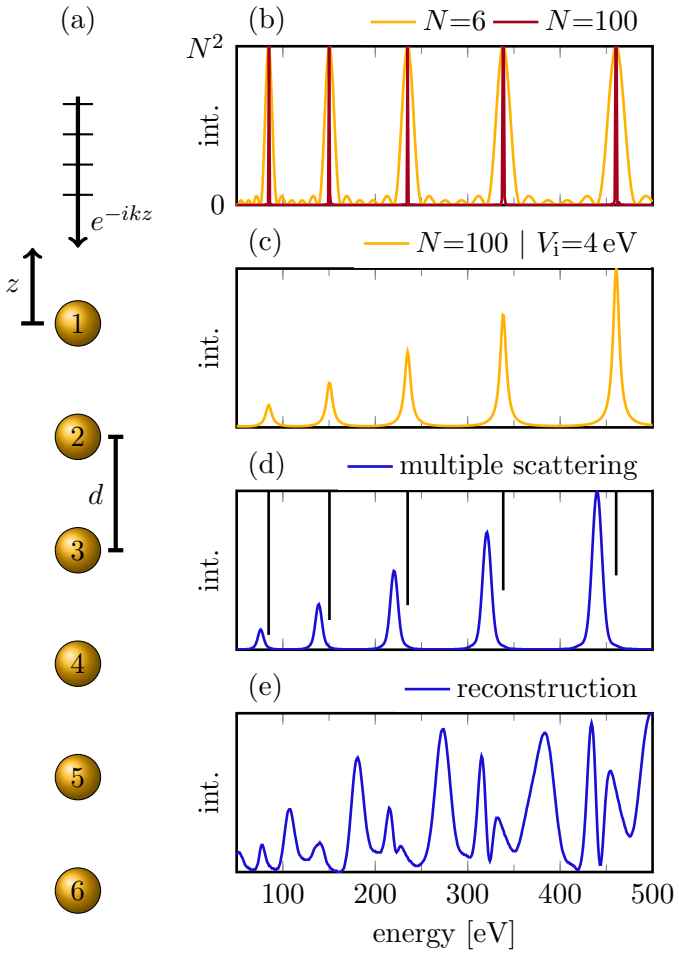

Figure 2.15.: (a) Sketch of the surface of a one-dimensional crystal. Atoms are aligned along one axis with the distance d. An electron wave e^{-ikz} reaches the crystal ($z < 0$) from the vacuum ($z > 0$) and gets scattered. (b)-(e) Intensity spectra starting with a kinematic approach and including progressively dynamic concepts like an imaginary part V_i of the inner potential and a more detailed description of the scattering process at the atoms. In (d) are the peak positions of (b) and (c) denoted to display the shift to lower energies, caused by the inclusion of phase shifts occurring at atomic scattering. In the one-dimensional model, additional peaks due to multiple scattering can only be observed in the presence of a relaxation.

To relate the expected width of peaks with the mean free path a closer look to Figure 2.15 (b) exhibits that two major peaks are separated by $N-1$ minima, with the number of scatterers N. Additionally, their distance in the reciprocal space can be expressed by $\Delta k = \frac{\pi}{d}$, since constructive interference happens, when $n\lambda = 2d$ is fulfilled. Therefore, the width of the peaks (in reciprocal space) is approximately given by $\Delta k' \approx \frac{\Delta k}{N} = \frac{\pi}{Nd}$.

The assumption that only scatterers up to a depth of one mean free path participate in the scattering process can be expressed by

$$Nd = \Lambda \tag{2.25}$$

$$\frac{\pi}{\Delta k'} = \frac{2E}{k|V_\mathrm{i}|}$$

$$\frac{\pi}{(\Delta\sqrt{E})} = \frac{2\sqrt{E}}{|V_\mathrm{i}|} \ , \tag{2.26}$$

with $(\Delta\sqrt{E}) = \sqrt{E + \frac{\Delta E}{2}} - \sqrt{E - \frac{\Delta E}{2}}$. It can be shown (cf. appendix B) that $\sqrt{E}\ (\Delta\sqrt{E}) \approx \frac{\Delta E}{2}$, thus the imaginary part of the potential V_i leads to peaks in the spectra with a width of approximately

$$\Delta E = \pi |V_\mathrm{i}| \ . \tag{2.27}$$

However, this is only a rough estimation and shall only illustrate the effect of the imaginary potential. Within the derivation of the Pendry R factor [14] a value of $\Delta E = 2|V_\mathrm{i}|$ is assumed.

2.3.2. Intensity distribution

Until now, only the angles under which constructive interference is expected were discussed. How the intensity is distributed over these reflexes can be estimated with the help of the structure factor within the kinematic scattering theory. Since the electron source is at a large distance from the surface, the amplitude of the incident electrons a_i at the position $\mathbf{r}$ can be described as plane waves by

$$a_i = a_0 e^{i\mathbf{k}_0\mathbf{r}} \qquad \text{with } k_0 = \frac{\sqrt{2m_e E}}{\hbar} \ , \tag{2.28}$$

with the incident wave vector $\mathbf{k}_0$, the electron mass m_e, and the kinetic energy of electrons E. The amplitude of the scattered beam a_f with the scattered wave vector $\mathbf{k}_f$ at the position $\mathbf{r}$ can be expressed by the plane wave

$$a_f = a_0\ e^{i\mathbf{k}_f\mathbf{r}} \sum_n f_{n(\mathbf{q})}\ e^{i\mathbf{q}\mathbf{r}_n} \qquad \text{with } \mathbf{q} = \mathbf{k}_f - \mathbf{k}_0 \ , \tag{2.29}$$

with the summation over all n atoms at positions $\mathbf{r}_n$ with the scattering factor $f_{n(\mathbf{q})}$, depending on the momentum transfer $\mathbf{q}$. This includes the phase shift due to the

different positions of the atoms ($e^{i\mathbf{q}\mathbf{r}_n}$) as well as the change in the amplitude of the electron wave due to the scattering at a single atom ($f_{n(\mathbf{q})}$). For a surface with two-dimensional periodicity, the atomic positions can be expressed as

$$\mathbf{r}_n = \mathbf{r}_\mathrm{u} + \mathbf{r}_\mathrm{surf} = \mathbf{r}_\mathrm{u} + m_1\mathbf{a} + m_2\mathbf{b} \ , \tag{2.30}$$

where $\mathbf{r}_\mathrm{u}$ includes all atoms within the surface unit cell. As described in section 2.2.4, to determine whether constructive interference occurs, only the component of the momentum transfer parallel to the surface $\mathbf{q}_\parallel$ is relevant. Inserting into 2.29 yields

$$a_f = a_0 \ e^{i\mathbf{k}_f\mathbf{r}} \ \sum_u f_{u(\mathbf{q})} \ e^{i\mathbf{q}\mathbf{r}_\mathrm{u}} \ \sum_{m_1,m_2} \ e^{i\mathbf{q}_\parallel\mathbf{r}_\mathrm{surf}} \ . \tag{2.31}$$

The exponential function in the second summation is one if the momentum transfer and the reciprocal lattice vector are equal ($\mathbf{q}_\parallel = \mathbf{G}_\parallel$) due to the definition of the reciprocal lattice vectors. For an infinite surface, the scattered amplitude is therefore infinite in directions of constructive interference and else zero. As $\mathbf{r}_\mathrm{surf}$ is only dependent of the size and shape of the unit cell, the position of reflexes is independent of the geometry within the unit cell, as well as the scattering mechanism itself. This means that multiple scattering can not affect the positions of reflexes.

However, real surfaces do not have perfect periodicity due to domain boundaries and atomic steps. Therefore, the second summation does not yield infinity at the constructive diffraction condition for real surfaces. This allows the inference from the spot profile of reflexes on the morphology of the surface. Due to its dependence on the lattice, it is called *lattice factor* G. The relative intensities of the different beams are, however, determined within the first summation which is only dependent on the structure within the unit cell, hence called *structure factor* F.

The intensity observed in the experiment is proportional to the (probability) amplitude of the electrons

$$I \propto |a_f|^2 = |a_0|^2 \ |F|^2 \ |G|^2 \ . \tag{2.32}$$

This illustrates the dependence of the atomic positions on beam intensity nicely. In principle, the effects of multiple scattering on the diffracted intensity could be included in the scattering factor f_u. However, since neighboring atoms scatter toward each other, such a modified scattering factor of a single atom would be dependent on the scattering factors of neighboring atoms. This complicates the evaluation of this approach and therefore does not help directly in the development of a theory that includes multiple scattering.

2.3.3. Description of the surface

To be able to calculate the amplitudes of the electrons diffracted at the surface and hence the intensities, it is necessary to make approximations for the surface, since

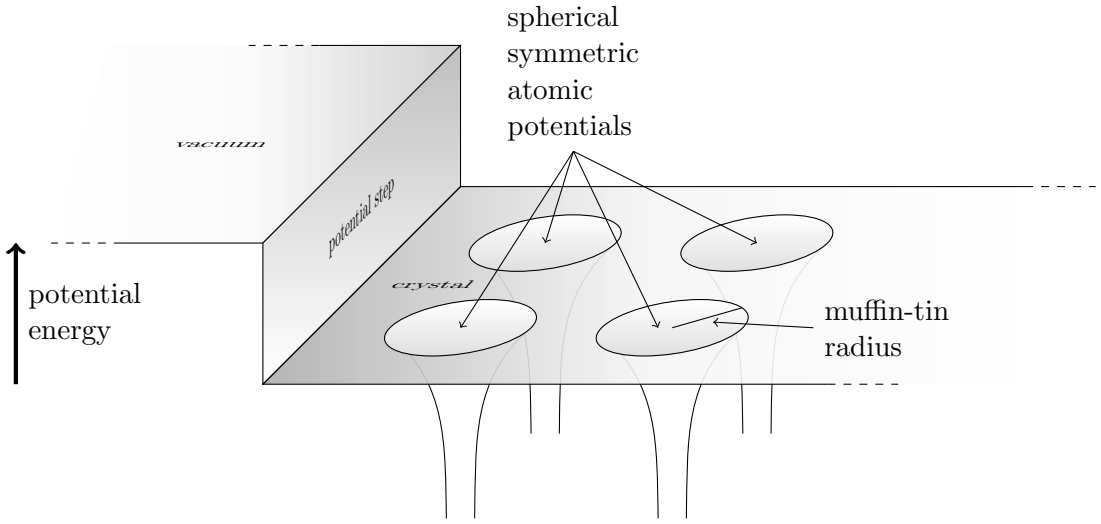

Figure 2.16.: Schematic sketch of the potential energy of a LEED electron within the muffin-tin model at the surface. The spherical symmetric atomic potentials are separated by regions of constant potential outside the muffin-tin radius. When entering the crystal from the vacuum, a potential step causes refraction of the electron wave.

the solution of the Schrödinger equation of an electron inside the potential of all surface atoms is too complex to solve generally. Therefore, the muffin-tin model is used to simplify the description of the surface. A sketch of the muffin tin model can be seen in Figure 2.16. The potential in the space inside the crystal between the atoms is assumed to be constant. This can be justified by the small variations in the potential in these regions compared to the energies of LEED electrons. Furthermore, the potential around atoms within the muffin-tin radius is approximated as spherical symmetric. Especially near the surface, this assumption is quite ambitious because of the highly anisotropic environment. Nevertheless, this approximation has been justified by the good agreement between experimental and calculated IV spectra and can be explained by the rather small contribution of the valence electrons to the scattering process.

These two approximations facilitate the treatment of the interaction between electron and surface massively. The potential step at the surface causes a refraction of the electron wave due to its changed kinetic energy and therefore altered wavelength. Propagation of the electron between the scatterers is easy to describe due to the constant potential, while the actual scattering at spherical symmetric potentials is also treatable.

2.3.4. Atomic scattering

With the assumption of spherical symmetrical atoms, the solution of the Schrödinger equation for a LEED electron can be expressed as the product of a radial function

$R_{l(r)}$ multiplied with the spherical harmonics $\mathrm{Y}_l^m{}_{(\theta,\varphi)}$ as the angular functions with the angular momentum quantum numbers l and m. Thus, the differential equation becomes one-dimensional

$$\frac{-\hbar^2}{2mr^2}\frac{\mathrm{d}}{\mathrm{dr}}\left(r^2\frac{\mathrm{d}R_{l(r)}}{\mathrm{dr}}\right)+\frac{\hbar^2 l(l+1)}{2mr^2}R_{l(r)}+V_{\mathrm{eff}(r)}R_{l(r)}=E_l R_{l(r)}\ . \tag{2.33}$$

This expansion to spherical waves is especially convenient, since the angular momentum is conserved in the scattering process at a spherical symmetric potential. The definition of the spherical harmonics as well as other functions used in the following can be found in appendix A.

Scattering of spherical waves

A solution for the radial part are the spherical Bessel functions [17], which can be expressed as a sum of Hankel functions of the first and second kind as in

$$R_{l(r)}=\mathrm{j}_{l(kr)}=\frac{1}{2}\left(\mathrm{h}_l^{(1)}{}_{(kr)}+\mathrm{h}_l^{(2)}{}_{(kr)}\right)\ , \tag{2.34}$$

with the wavenumber $k=\sqrt{2m_eE}/\hbar$. Here, the Hankel functions describe an incoming and outgoing wave, respectively. If only elastic scattering processes are considered, the incoming and outgoing scattered wave must have the same amplitude because of flux conversation and thus can only be phase shifted. Hence, the scattering potential can modify the outgoing wave and therefore the solution to the Schrödinger equation only according to

$$R'_{l(r)}=\frac{1}{2}\left(e^{2i\delta_l}\ \mathrm{h}_l^{(1)}{}_{(kr)}+\mathrm{h}_l^{(2)}{}_{(kr)}\right)\ , \tag{2.35}$$

with the phase shifts δ_l that are dependent on the angular momentum quantum number l. To obtain an expression for the generated scattered wave, the difference between equations (2.35) and (2.34) yields

$$\frac{e^{2i\delta_l}-1}{2}\ \mathrm{h}_l^{(1)}=\mathrm{t}_l\mathrm{h}_l^{(1)}\ . \tag{2.36}$$

Here, t_l is the amplitude of the scattered wave for a given l, in the following called *scattering element*.

Scattering of plane waves

Since the incoming electron beam on the surface can be regarded as a plane wave, it is necessary to determine how a plane wave is affected by a spherical symmetric potential. Therefore, the plane wave expansion

$$e^{i\mathbf{kr}}=4\pi\sum_{l=0}^{\infty}\sum_{m=-l}^{l}i^l\ \mathrm{j}_{l(kr)}\ \mathrm{Y}_l^m{}_{(\mathbf{k})}\ {}^*\mathrm{Y}_l^m{}_{(\mathbf{r})} \tag{2.37}$$

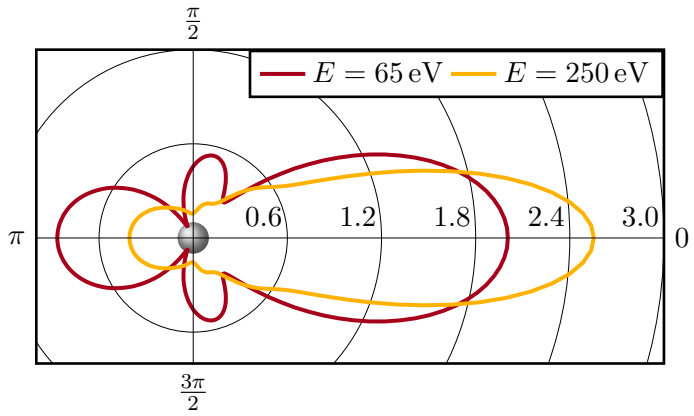

Figure 2.17.: Angular dependence of the absolute values of the atomic scattering factor $|t_\theta|$ of silicon for two energies (65 eV and 250 eV). The forward scattering (angle of 0) increases with increasing energy. Values are given in [Å].

is used. The asterisk denotes complex conjugation. A substitution of the Bessel function $\mathrm{j}_l(kr)$ by the scattered waves of 2.36 results in

$$2\pi \sum_{l=0}^{\infty} \sum_{m=-l}^{l} i^l \, (e^{2i\delta_l} - 1) \, \mathrm{h}_l^{(1)}(kr) \, \mathrm{Y}_l^m(\mathbf{k}) \, {}^*\mathrm{Y}_l^m(\mathbf{r}) \; , \tag{2.38}$$

as a expression for the amplitude of a scattered plane wave. For large arguments, the Hankel functions can be expressed as

$$\lim_{kr\to\infty} \left(i^{l+1} \, \mathrm{h}_l^{(1)}(kr) \right) = \frac{e^{ikr}}{kr} \; , \tag{2.39}$$

and thereby, for the asymptotic behavior of the scattered wave follows

$$t_\theta \, \frac{e^{ikr}}{r} \; , \tag{2.40}$$

with the atomic scattering factor t_θ

$$t_\theta = \frac{4\pi}{i \, k} \sum_{l=0}^{\infty} \sum_{m=-l}^{l} t_l \, \mathrm{Y}_l^m(\mathbf{k}) \, {}^*\mathrm{Y}_l^m(\mathbf{r}) \; . \tag{2.41}$$

The index of t_θ denotes the dependence on the scattering angle θ, which is the angle between the directions of incident wave $\mathbf{k}$ and scattered wave $\mathbf{r}$. Figure 2.17 shows the absolute value of the atomic scattering factor $|t_\theta|$ of a silicon atom for two different energies. The angle dependence stems from phase shifts of the respective partial waves. While at lower energies, the side and back scattering is comparably strong, forward scattering is predominant at higher energies.

According to Heinz [10], the atomic scattering factor is related to the differential and total elastic cross section by

$$\frac{\mathrm{d}\sigma}{\mathrm{d}\Omega} = |t_\theta|^2 \qquad \text{and} \qquad \sigma = \frac{4\pi}{k^2} \sum_l (2l+1) \sin^2 \delta_l = \frac{4\pi}{k^2} \, \mathrm{Im}\{t_{\theta=0}\} \; . \tag{2.42}$$

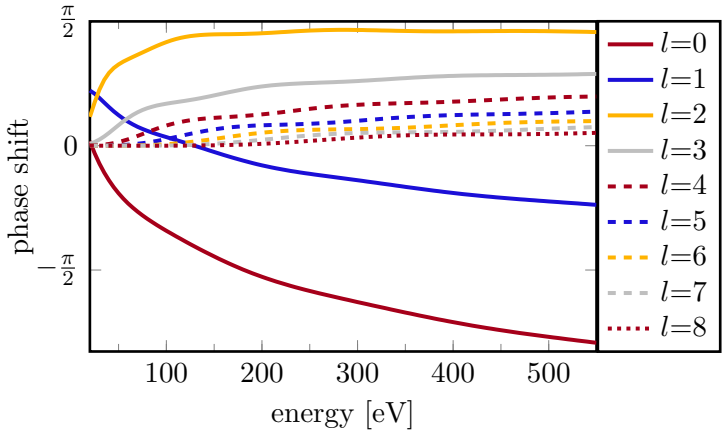

Figure 2.18.: The energy dependence of the phase shifts of silicon up to $l = 8$. The magnitude of the phase shift decreases with increasing l, while at higher energies an increasing number of phase shifts is relevant.

Therefore, the cross section is of comparable order as the geometrical cross section, which means that in a densely packed crystal, the probability that an electron gets scattered by an atom its passing is quite high.

Phase shifts

As can be seen from equations (2.36) and (2.38), the scattering process can be described using only the phase shifts δ_l, without the need to solve the Schrödinger equation for every incident wave. This is only true for the region outside the muffin-tin radius, but for LEED the exact solution inside the muffin-tin radius is irrelevant. For this reason, it is possible to separate the calculation of phase shifts (scattering of the single atoms) from the calculation of the scattering of the lattice.

The phase shifts can be obtained by the requirement that the wave functions inside and outside the muffin-tin radius r_m must have a continuous transition. This criteria is met, when the logarithmic derivatives are equal [17], yielding for the solutions $\mathrm{R}_{l(r)}$ of equation (2.33) and the scattered wave field from equation (2.35)

$$\frac{\mathrm{R}'_{l(r_m)}}{\mathrm{R}_{l(r_m)}} = \frac{e^{2i\delta_l}\ \mathrm{h}_l^{'(1)}(kr_m) + \mathrm{h}_l^{'(2)}(kr_m)}{e^{2i\delta_l}\ \mathrm{h}_l^{(1)}(kr_m) + \mathrm{h}_l^{(2)}(kr_m)} \ . \tag{2.43}$$

Reorganizing yields

$$e^{2i\delta_l} = \frac{\mathrm{h}_l^{'(2)}(kr_m) - L\ \mathrm{h}_l^{(2)}(kr_m)}{L\ \mathrm{h}_l^{(1)}(kr_m) - \mathrm{h}_l^{'(1)}(kr_m)} \ , \qquad \text{with} \quad L = \frac{\mathrm{R}'_{l(r_m)}}{\mathrm{R}_{l(r_m)}} \ . \tag{2.44}$$

Figure 2.18 shows the energy dependence of the phase shifts of silicon up to $l = 8$. While at 100 eV approximately five phase shifts are sufficient, it is necessary to include more phase shifts for higher energies. Nonetheless, the infinite sum from equation (2.38) can be truncated at approximately $l = 10$ for most cases, without much loss of accuracy.

With the description of atomic scattering through phase shifts, the scatterers are effectively replaced by point scatterers. Hereby, the description of the scattering by the lattice is further simplified. This point scatterer picture is not an approximation; instead, it is a consequence of the fact that outside the muffin-tin radius, the scattering can be described as a phase shift.

2.3.5. Temperature effects

In the previous picture, the atoms were assumed to be motionless at their respective positions in the lattice. To estimate the influence of thermal vibrational motions within the kinematic scattering theory, the Debye-Waller factor can be used.

Debye-Waller factor

The structure factor from equation (2.31) can be extended, to include the time average of the displacements of the atoms around their lattice position ($\mathbf{r}_\mathrm{u} + \Delta\mathbf{r}_\mathrm{u}$)

$$\overline{F_{(T)}} = \sum_u f_{u(\mathbf{q})}\ \overline{e^{i\mathbf{G}_\parallel(\mathbf{r}_\mathrm{u}+\Delta\mathbf{r}_\mathrm{u})}} = \sum_u f_{u(\mathbf{q})}\ e^{i\mathbf{G}_\parallel\mathbf{r}_\mathrm{u}}\ \overline{e^{i\mathbf{G}_\parallel\Delta\mathbf{r}_\mathrm{u}}} = F_{(T=0)}\ \overline{e^{i\mathbf{G}_\parallel\Delta\mathbf{r}_\mathrm{u}}}\ . \quad (2.45)$$

This can be shown [13] to be approximately

$$\overline{F_{(T)}} \approx F_{(T=0)}\ e^{-\frac{1}{6}|\mathbf{G}_\parallel|^2\ \overline{(\Delta r_\mathrm{u})^2}}\ , \quad (2.46)$$

assuming isotropic thermal vibrations. Hence, the observed intensity is attenuated by the Debye-Waller factor according to

$$I_{(T)} = I_{(T=0)}\ e^{-\frac{1}{3}|\mathbf{G}_\parallel|^2\ \overline{(\Delta r_\mathrm{u})^2}}\ . \quad (2.47)$$

This is only valid within kinematic theory. For electrons that get scattered by multiple atoms, a stronger attenuation is expected. Therefore, the decrease of the reflex intensity in the spectra is dependent on the dominant scattering mechanism of this single peak. Hence, the attenuation of the intensity should be different for distinct parts of the spectra.

Temperature dependent phase shifts

To include thermal vibrations within a frame applicable to multiple scattering, *temperature dependent phase shifts* can be used. If only isotropic vibrations and no correlations between different atoms are considered, the temperature dependent scattering factor $t_{\theta(T)}$ can be expressed by

$$t_{\theta(T)} = e^{-M}\ t_\theta = \frac{4\pi}{i\ k}\ \sum_{l=0}^{\infty}\sum_{m=-l}^{l}\ t_{l(T)}\ \mathrm{Y}_l^m{}_{(\mathbf{k})}\ {}^*\mathrm{Y}_l^m{}_{(\mathbf{r})} \quad (2.48)$$

with the the dampening factor e^{-M} and the now temperature dependent scattering elements $t_{l(T)}$ that are in turn given by

$$t_{l(T)} = \frac{e^{2i\delta_{l}(T)} - 1}{2} \ , \tag{2.49}$$

with the temperature dependent phase shifts $\delta_{l(T)}$. According to van Hove et al. [18], the relation between the scattering element t_l and the temperature dependent scattering element $t_{l(T)}$ is given by

$$t_{l(T)} = \sum_{l_i=0}^{l_{max}} i^{l_j} \ e^{-4\alpha(E+V_\mathrm{r})} \ \mathrm{j}_{l_j}(4\alpha(E+V_\mathrm{r})) \ t_{l_j} \ \left(\frac{4\pi(2l_i+1)(2l_j+1)}{2l+1} \right)^{\frac{1}{2}} \gamma_{(l,l_i,l_j)} \tag{2.50}$$

with $\alpha = \frac{m_e}{\hbar^2} \frac{1}{6} \ \overline{(\Delta r)^2}$. $\gamma_{(l,l_i,l_j)}$ are the Gaunt coefficients with $m = m_i = m_j = 0$ and thus $l_j = l + l_i$ for non-zero values and l_{max} being the highest value of l considered for calculations that appear again in section 2.3.6. The prefactors in α are due to the use of the Debye-Waller factor with $M = \frac{1}{6}|\mathbf{G}|^2 \ \overline{(\Delta r)^2}$.

Thus, the previous discussed formalism for the atomic scattering can be retained. By the conversation of the phase shifts to their temperature dependent counterparts, an isotropic thermal vibration is taken into account.

2.3.6. Propagation inside the crystal

While scattering on single atoms was described in chapter 2.3.4, a full dynamical scattering theory also needs a description of the electrons propagating inside the crystal between the atoms. Within the muffin-tin model, the inter-atomic space has constant potential. Furthermore, the assumed spherical symmetry of the atomic potential allows them to be treated as point scatterers. Notably, due to the description of atomic scattering by phase shifts, the results for propagation obtained by a point scatterer picture are identical to those obtained by calculations with a finite muffin-tin radius. Therefore, the muffin-tin radius only appears in the calculation of phase shifts, while for propagation point scatterers are assumed.

To describe the propagation of an electron between two atoms within the spherical wave representation, it is necessary to define how the spherical waves centered on the first atom decompose into spherical waves centered on the second atom. This can be done using a Greens Function G [17], in the following called *propagator* given by

$${}^{2}_{1}G^{L_2}_{L_1} = 4\pi \sum_{l_r} \sum_{m_r=-l_r}^{l_r} i^{l_r} \ \gamma_{(L_1,L_2,L_r)} \ \mathrm{h}^{(1)}_{l_r}(k|\mathbf{r}_2-\mathbf{r}_1|) \ \mathrm{Y}^{m_r}_{l_r}(\mathbf{r}_2-\mathbf{r}_1) \ . \tag{2.51}$$

Here, the value of ${}^{2}_{1}G^{L_2}_{L_1}$ gives the transition for a spherical wave with $L_1 = \{l_1, m_1\}$ centered on atom 1 (located at $\mathbf{r}_1$) to the spherical wave with $L_2 = \{l_2, m_2\}$, centered on atom 2 (located at $\mathbf{r}_2$). The values of $L_r = \{l_r, m_r\}$ are given by

$$|l_1 - l_2| \leq l_r \leq l_1 + l_2 \qquad \text{and} \qquad m_r = m_1 + m_2 \ . \tag{2.52}$$

This constraint stems from the Gaunt coefficients γ

$$\gamma_{(L_1,L_2,L_r)} = \int_{\varphi}^{2\pi} \int_{\theta}^{\pi} \mathrm{Y}_{l_1}^{m_1}(\theta,\varphi)\ \mathrm{Y}_{l_2}^{m_2}(\theta,\varphi)\ {}^{*}\mathrm{Y}_{l_r}^{m_r}(\theta,\varphi)\ \sin\theta\ \mathrm{d}\theta\mathrm{d}\varphi\ , \tag{2.53}$$

that are zero otherwise. The Hankel function and the spherical harmonics describe the propagation, while the need for the Gaunt coefficients arises from the expansion from spherical waves in one reference frame (atom 1) into spherical waves of another reference frame (atom 2). The use of this propagator requires the treatment of the atoms as point scatterers as the propagation ranges from one atomic center to the other.

2.3.7. Inelastic effects

Neither in the atomic scattering, nor in the propagation were any inelastic effects included until now. In the experiment, the grids in front of the screen of the LEED optics repel electrons that have lost energy through inelastic effects. In the dynamic LEED theory, it is therefore sufficient to include all inelastic effects (no matter what exact processes take place) by the decrease of the amplitude of the wave functions of elastically scattered electrons. This can be done by the introduction of an imaginary part V_i to the inner potential. Hereby, the wave vector k of the electron inside the crystal becomes complex, so that the Hankel function in the propagator causes a dampening of the electron wave. In this picture, the electron is still scattered elastically at the atoms, but its probability amplitude is decreased the further it propagates inside the crystal. Therefore, the concept of the imaginary part of the inner potential is equivalent to a mean free path of the electron inside the crystal (cf. section 2.3.1).

2.3.8. Calculation of multiple scattering

To determine the amplitude of the electron scattered by the surface, all possibilities, how the electron can be scattered should be considered. Unfortunately, the possibilities are virtually infinite, since the electrons can penetrate the crystal effectively to an infinite depth and also can be scattered infinite times between the atoms. However, the probability amplitudes for those paths with a very high number of scatterings or long propagations inside the crystal are low, so it is sufficient to include only those scattering paths with higher probability.

Probability of a single path

To obtain the probability for any given path, the atomic scattering must be combined with the propagation. In terms of spherical waves, this can be done using matrix multiplication. The scattering elements t_l can be arranged in a diagonal scattering matrix $\overline{T}$ with the size of $(l_{max}+1)^2$, containing an entry for every $L = \{l, m\}$. The fact that $\overline{T}$ is diagonal stems from the conservation of the angular momentum

quantum numbers l and m upon scattering at a spherical potential. Thus, for non-spherical potentials, $\overline{T}$ would also be non-diagonal. The propagator matrix contains all possible combinations of L_1 and L_2 and has therefore also the size $(l_{max}+1)^2$. For scattering at atom 1, respectively propagation from atom 1 to atom 2, $\overline{T}$ and $\overline{G}$ would be composed for $l_{\max}=1$ according to

$$ {}_1\overline{T} = \frac{1}{ik}\begin{pmatrix} {}_1t_{l=0} & 0 & 0 & 0 \\ 0 & t_{l=1} & 0 & 0 \\ 0 & 0 & t_{l=1} & 0 \\ 0 & 0 & 0 & t_{l=1} \end{pmatrix}, \tag{2.54} $$

$$ {}^2_1\overline{G} = ik\begin{pmatrix} {}^2_1G^{l_2=0,m_2=0}_{l_1=0,m_1=0} & G^{0,0}_{1,-1} & G^{0,0}_{1,0} & G^{0,0}_{1,1} \\ G^{1,-1}_{0,0} & G^{1,-1}_{1,-1} & G^{1,-1}_{1,0} & G^{1,-1}_{1,1} \\ G^{1,0}_{0,0} & G^{1,0}_{1,-1} & G^{1,0}_{1,0} & G^{1,0}_{1,1} \\ G^{1,1}_{0,0} & G^{1,1}_{1,-1} & G^{1,1}_{1,0} & G^{1,1}_{1,1} \end{pmatrix}. \tag{2.55} $$

Here, inside the matrices, the indices for the respective atoms 1 and 2 were omitted, except for the first entry. The prefactors result from the common expression as a T-matrix [19]. The probability amplitude of an electron is then given by a vector of length $(l_{max}+1)^2$, containing the amplitudes of all spherical waves up to l_{max}. With this formalism, the expression

$$ A' = {}_1\overline{T}\ {}^1_2\overline{G}\ {}_2\overline{T}\ {}^2_3\overline{G}\ {}_3\overline{T}\ {}^3_1\overline{G}\ {}_1\overline{T}\ A \tag{2.56} $$

gives the final probability amplitude A' of an electron with initial amplitudes A which is scattered by atom 1, then propagates to atom 3, then gets scattered at atom 3 to propagate to atom 2 to get scattered there, to finally propagate to atom 1 and get scattered there again. This path is depicted in Figure 2.19. In this fashion, the probability of every possible path can be determined. Finally, to obtain the resulting total amplitude, a summation over the spherical waves of all paths must be performed.

Computation

The only thing left is a scheme to include paths, until the final scattered amplitudes converge. While there are several possibilities how this can be achieved, it is necessary to consider the computational effort, so the calculations converge fast enough. While there have been multiple approaches in the beginning [18, 20–25], a self-consistent formalism that divides the surface into distinct layers [18] has become the prevalent approach. Thereby, the final wave departing from atom 1 (A'_1) is expressed by the sum of the scattered incident plane wave on atom 1 (A_1) and all waves scattered from neighboring atoms toward atom 1 to be a last time scattered there. For two atoms, this is described by the infinite sums

$$ A'_1 = {}_1\overline{T}\ A_1 + {}_1\overline{T}\ {}^1_2\overline{G}\ {}_2\overline{T}\ A_2 + {}_1\overline{T}\ {}^1_2\overline{G}\ {}_2\overline{T}\ {}^2_1\overline{G}\ {}_1\overline{T}\ A_1 + \dots, \tag{2.57} $$

$$ A'_2 = {}_2\overline{T}\ A_2 + {}_2\overline{T}\ {}^2_1\overline{G}\ {}_1\overline{T}\ A_1 + {}_2\overline{T}\ {}^2_1\overline{G}\ {}_1\overline{T}\ {}^1_2\overline{G}\ {}_2\overline{T}\ A_2 + \dots, \tag{2.58} $$

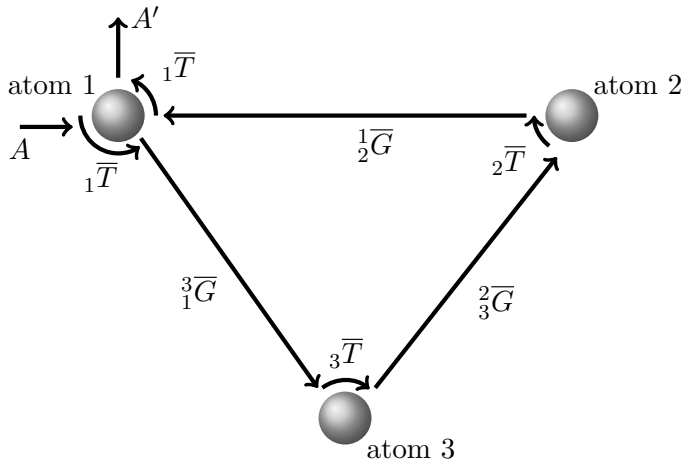

Figure 2.19.: Schematic sketch of the scattering path described by equation (2.56). The electron with amplitude A gets scattered from atom 1 to atom 3, then to atom 2 and back to atom 1 to have the resulting amplitude A'. The propagators G and scattering matrices T are denoted at their respective segments.

which can also be written as

$$A'_1 = {}_1\overline{T}\, A_1 + {}_1\overline{T}\, {}^1_2\overline{G}\, A'_2 \,, \tag{2.59}$$

$$A'_2 = {}_2\overline{T}\, A_2 + {}_2\overline{T}\, {}^2_1\overline{G}\, A'_1 \,. \tag{2.60}$$

Thus, scattering up to an infinite order is included. This can be done analogously for any number of atoms. To calculate the amplitudes A'_n, these equations can be solved using matrix notation as

$$\begin{pmatrix} A'_1 \\ A'_2 \end{pmatrix} = \begin{pmatrix} I & -{}_1\overline{T}\, {}^1_2\overline{G} \\ -{}_2\overline{T}\, {}^2_1\overline{G} & I \end{pmatrix}^{-1} \begin{pmatrix} {}_1\overline{T} A_1 \\ {}_2\overline{T} A_2 \end{pmatrix} \,. \tag{2.61}$$

While this is an elegant solution in including multiple scattering up to an infinite order, this comes at the cost of requiring repeated matrix inversions that are computationally expensive, thus limiting this approach to small numbers of atoms. However, this dilemma can be circumvented by the use of the translational symmetry of the surface.

Since any atoms scattered amplitude must equal the scattered amplitudes of equal atoms in adjacent unit cells due to symmetry, every atom in a so-called Bravais layer (one atom per unit cell) has the same diffracted wave. Figure 2.20 depicts how the surface is divided into Bravais layers, which are used in the description of multiple scattering. First, the multiple scattering within each Bravais layer is solved. A *layer diffraction matrix* can be used to describe how an incident wave on a given layer is diffracted into departing waves. Forward as well as back scattering must be considered. Then, the transition from one Bravais plane to another is determined. This can be done either in spherical waves or in plane waves for which the layer spacing must not be smaller than 0.7 Å to ensure convergence [10]. Thereby, the scattering of the whole surface is described by a stacking of those layers. This can be done efficiently by *renormalized forward scattering*, sorting the possible sequence of layers participating in the scattering such that low numbers of backscattering are

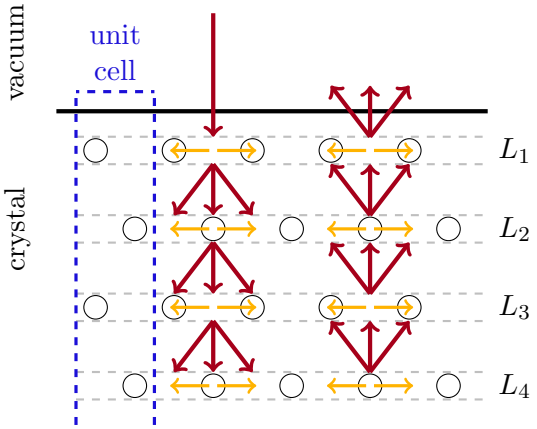

Figure 2.20.: Illustration of the division of the surface atoms into Bravais layers L_n, denoted by gray dashed lines. First, the multiple scattering inside a layer is calculated (yellow arrows). Then, the propagation between layers is computed (red arrows). Thereby, a *layer diffraction matrix* can describe how a plane wave incident on a layer is diffracted into departing plane waves. The summation over all possible sequences of layers describes the diffraction of the entire surface.

considered first. This helps converging the calculations, since the backscattering is weak compared to the forward scattering of a layer for LEED electrons (cf. Figure 2.17).

Another aspect is the inclusion of the unreconstructed atoms below the surface, which also exhibit perfect periodicity in the direction into the surface. The method of *layer doubling* can be used to calculate the diffraction of the atoms at bulk positions. Thereby, the diffraction for a slab of n bulk layers is calculated. Then, the thickness of this slab is doubled and the diffraction is calculated again. This is repeated, until the diffracted amplitudes converge.

Nonetheless, full dynamical calculations are computationally costly. The trial and error approach of IV LEED makes it very time consuming to optimize surface structures. This is further complicated through the complex process of matrix inversion, making it necessary to recalculate everything if only a small change in one atomic position is considered. A solution to this problem is Tensor LEED [26]. Within this method, a full dynamical calculation of a *reference structure* is conducted. Then, the effects of small deviations from this reference structure is expressed in a first-order perturbation theory, allowing the fast analysis of the full parameter space around the reference structure. This leads to a significant acceleration compared to the full dynamical approach. However, this does not solve the problem of the enormous effort it takes to calculate the diffraction at large unit cells or vicinal surfaces. Since the approximations allow only the exploration of the parameter space close to the reference structure, still multiple full dynamical calculations are necessary.

2.4. Elastic Strain Energy of Crystals

The elastic strain energy in covalent crystals is caused by the deviation of bond lengths and bond angles from their equilibrium values. The Keating energy is a

concept to quantify this energy [27, 28] by the approximation

$$\alpha \sum_{i,j} \left(\mathbf{r}_{ij}^2 - r_0^2\right)^2 \; + \; \beta \sum_{i,j,k} \left(\mathbf{r}_{ij} \cdot \mathbf{r}_{ik} + \frac{1}{3} r_0^2\right)^2 \tag{2.62}$$

for crystals with tetrahedral bonds. Here, $\mathbf{r}_{ij}$ is the vector from atom i to atom j, while r_0 denotes the equilibrium bond length. The sums run over each bond (ij) and each bond angle (ijk), respectively. The factor $\frac{1}{3}$ causes a tetrahedral equilibrium bond configuration. The parameters α and β are element specific constants. In this thesis, for silicon, the values of $\alpha = 0.2009\,\mathrm{eV\,\mathring{A}^{-4}}$ and $\beta = 0.0183\,\mathrm{eV\,\mathring{A}^{-4}}$ according to Pedersen [28] were used. Notably, the concept of the Keating energy can be extended to any covalent crystal (exhibiting different chemical elements and non-tetrahedral bond angles). However, for this thesis, the special case from equation (2.62) is sufficient.

Since the Keating energy is derived from the deviation of the equilibrium, it is zero for a fully relaxed crystal. Furthermore, this concept can not be used to find new structures due to the fact that all bonds have to be predefined and thus neither new bonds can be formed nor existing bonds can be broken. However, the Keating energy can be used to predict the displacements of atoms adjacent to a disturbance of the perfect crystal structure like a surface reconstruction.

3. Investigated Materials and Systems

In this chapter the material systems investigated in this thesis are presented. This includes basic properties as well as a rough overview of previous studies to enable a better understanding of the experiments within this thesis.

3.1. Silicon Substrates

Silicon is the second most common chemical element within the Earth's crust and has the chemical symbol **Si**. Its atomic number is 14; hence it is part of the carbon group and has the electron configuration [Ne] $3s^2$ $3p^2$. Therefore, it crystallizes sp^3 hybridized in a tetrahedral configuration, building a diamond cubic lattice as is depicted in Figure 3.1. The silicon crystal is a semiconductor, offering the possibility to tune its conductivity at room temperature by the doping with other elements (e.g. boron, phosphorous or nitrogen). These electrical characteristics as well as its abundance in the earth's crust made silicon the predominantly used substrate within the semiconductor industry. Silicons cubic lattice constant is $a_{\mathrm{Si}} \approx 5.430\,\text{Å}$, resulting in a next neighbor distance of $a_{\mathrm{NN}} = a_{\mathrm{Si}}\sqrt{3}/4 \approx 2.351\,\text{Å}$. Its melting point is $T_{\mathrm{melt}} \approx 1410\,^{\circ}\mathrm{C}$.

3.1.1. Si(001)

The Si(001) surface is a cut along one face of the cubic unit cell, exhibiting a quadratic unit cell with the lattice constant $a_{001} = a_{\mathrm{Si}}/\sqrt{2} \approx 3.840\,\text{Å}$, as is depicted in Figure 3.2. The layer spacing is $a_{\mathrm{Si}}/4 \approx 1.357\,\text{Å}$. Due to the two unsaturated bonds per surface atom, the surface reconstructs at room temperature into a (2×1)

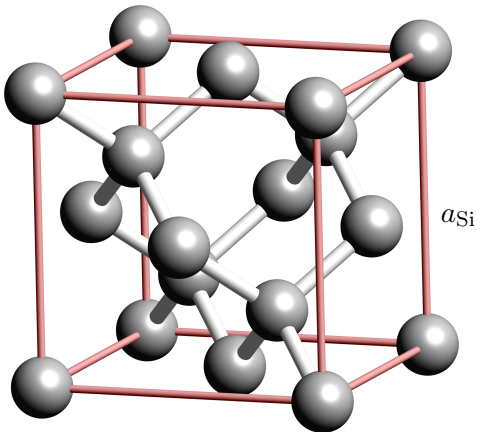

Figure 3.1.: Cubic unit cell of the diamond cubic lattice, caused by the tetrahedral bonding of the silicon atoms. The red rods highlight the cubic unit cell, while the white rods illustrate the covalent bonds between the silicon atoms.

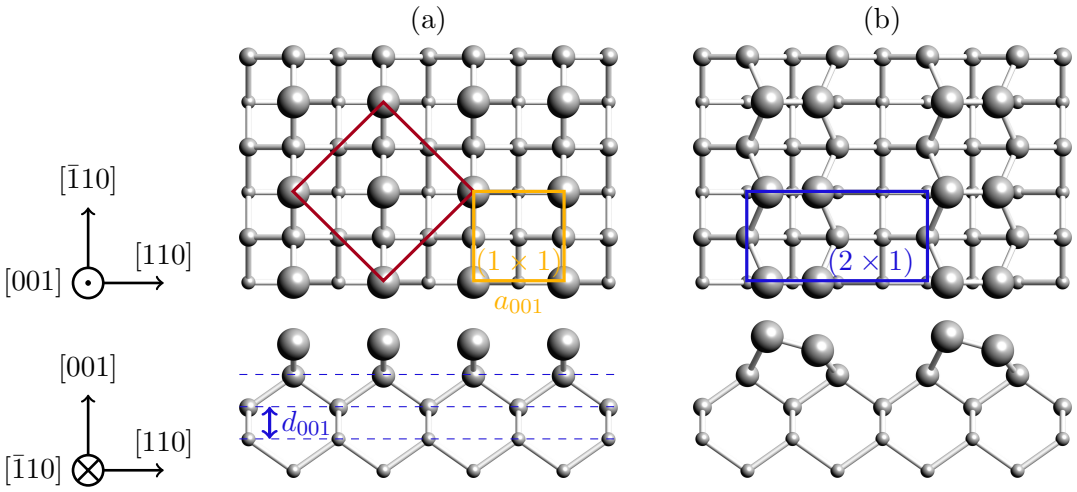

Figure 3.2.: (a) Bulk terminated surface of the Si(001) surface. The face of the cubic bulk unit cell is denoted in red, while the surface unit cell with the lattice constant a_{001} is denoted in yellow. The layer spacing is depicted in blue. (b) Sketch of the reconstruction due to the dimerization of surface atoms forming a (2×1) reconstruction as denoted in blue. The diameter of the atoms decreases with increasing distance to the surface for illustration purposes.

superstructure to minimize its surface energy. In this reconstruction, two adjacent surface atoms form a new bond to reduce the number of dangling bonds. The so-formed dimers are tilted, but can switch their orientation. This happens at room temperature at such a high rate that they appear symmetric within STM imaging [29]. However, the probing of the LEED electrons is so fast that this is not the case for LEED [30]. At low temperatures, the surface undergoes a transition into a c(4×2) reconstruction, caused by an alternating alignment of the tilted dimers, which is the ground state of this surface, although transitions to other reconstructions can be induced easily by electron beam or probing tips [31–34]. Therefore, at room temperature the dimers are not neatly aligned in a (2×1) reconstruction, but randomly tilted, which causes the appearance as (2×1) in the LEED pattern.

Due to the bonding to the second layer, the dimers can only form along one axis, though at atomic steps that are always present in the experiment, this axis is rotated by 90° for adjacent terraces. Therefore, in the diffraction pattern, the superposition of both rotational domains can be observed as depicted in Figure 3.3. The Si(001) surface is highly reactive, so a diffraction pattern of a (2×1) reconstruction is a good indication for a clean and adsorbate free Si(001) surface.

3.1.2. Si(111)

The Si(111) surface is a cut along the diagonal plane of the cubic unit cell. Therefore, it exhibits a hexagonal surface structure with a lattice constant of $a_{111} = a_{\mathrm{Si}}/\sqrt{2} \approx$

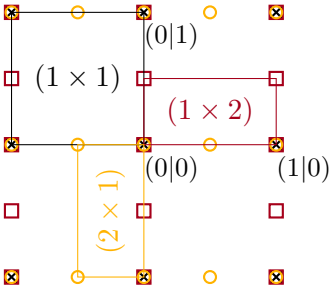

Figure 3.3.: Schematic diffraction pattern for the reconstructed surface of Si(001). The reflexes of the (1×1) are depicted with black crosses. The (2×1) reconstruction exists due to the rotation at atomic steps in two rotational domains (red squares and yellow circles), which superimpose in the diffraction pattern. Hence, the resulting diffraction pattern has a quadratic box like shape.

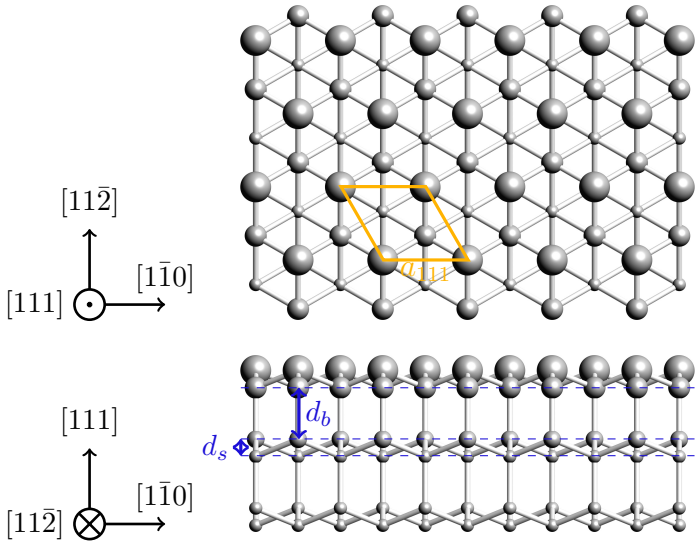

Figure 3.4.: Sketch of the bulk-terminated Si(111) surface. The surface unit cell is denoted in yellow, while the lattice constant of the surface unit cell is denoted in blue. The diameter of the atoms decreases with increasing distance to the surface for illustration purposes.

3.840 Å, as is depicted in Figure 3.4. The unsaturated bonds of each surface atom lead upon annealing to a (7×7) reconstruction, described by the so-called DAS model (dimer stacking fault [35]), where Si adatoms reduce the total energy. This reconstruction can be used as an indication for a clean Si(111) surface.

As depicted in Figure 3.4, the layers have an alternating big ($d_\mathrm{b} = a_\mathrm{NN} \approx 2.351$ Å) and small layer spacing ($d_\mathrm{s} = d_\mathrm{b}/3 \approx 0.784$ Å). This is relevant for the treatment of this substrate within the common dynamical LEED formalism. The two layers with the small spacing must be treated as a composite layer to ensure convergence of the calculation and are hence called in the following *bilayer*.

3.2. Gold on Si(111)

Gold is a chemical element with the chemical symbol **Au** and has the atomic number 79 with the electronic configuration [Xe] $4f^{14}$ $5d^{10}$ $6s^1$. It belongs to the noble metals and exhibits therefore a low chemical reactivity.

On a Si(111) surface, multiple reconstructions induced by gold atoms appear in the sub-monolayer regime, depending on the temperature and especially the coverage. At elevated temperatures of approximately 700 °C, Au coverages less than 0.5 monolayers lead to a coexistence of pure (7×7) reconstructions of the substrate

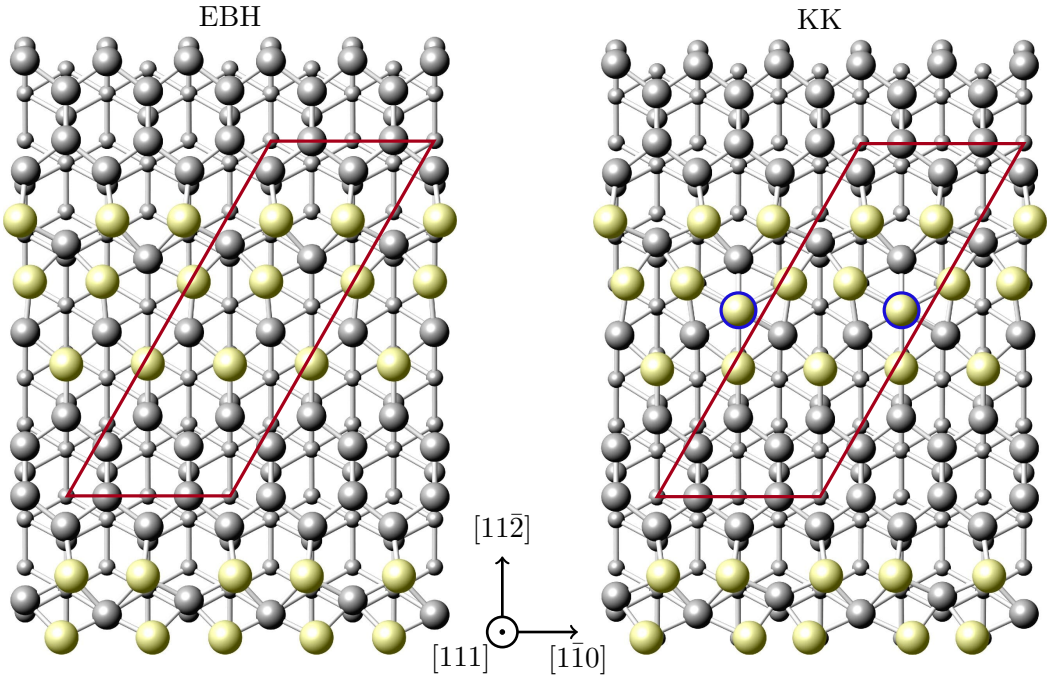

Figure 3.5.: Structure models of the EBH and the KK model. The unit cell is denoted in red. The additional gold atom in the KK model is highlighted with a blue circle. Both models exhibit a silicon honeycomb motif between the rows of gold atoms.

and areas with a (5×2) reconstruction induced by gold atoms. A surface covered completely by the (5×2) reconstruction can only be observed at approximately 0.67 monolayers. Higher coverages lead to the coexistence of the (5×2) reconstruction with a reconstruction exhibiting $(\sqrt{3} \times \sqrt{3})$ periodicity until the (5×2) reconstruction vanishes. At temperatures above 800 °C only a disordered (1×1) phase can be observed [36].

However, for this thesis, only the (5×2) reconstruction is of particular interest. Since its first description [3], multiple suggestions about the atomic arrangements were made. Currently, there are two models that can explain experimental data well, the Erwin-Barke-Himpsel (EBH [4]) and the Kwon-Kang (KK [5]) model, which are depicted in Figure 3.5. The main difference is an additional gold atom in the KK model (highlighted by a blue circle), leading to small displacements of surrounding atoms. The otherwise high similarity of the two models causes the difficulties to distinguish them on the basis of experimental data.

Notably, due to the honeycomb motif of the silicon atoms at the surface, the gold adatoms build chains, and thus represent a model system of nanowires. Since these wires can be shifted with respect to each other by a lattice vector of the substrate, adjacent wires are uncorrelated. This leads to streaks in the diffraction pattern, instead of sharp reflexes for the $\times 2$ periodicity.

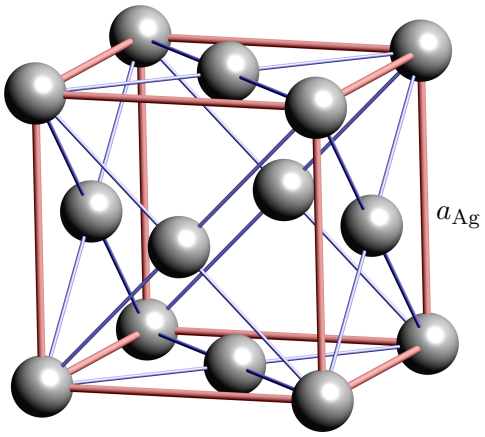

Figure 3.6.: Cubic unit cell of the face centered cubic lattice. The red rods highlight the cubic unit cell with the lattice parameter $a_{\mathrm{Ag}} \approx 4.085\,\text{Å}$, while the blue rods act only as guide to the eye to clarify the positions of the atoms on the faces.

3.3. Ag(001)

Silver is a chemical element with the atomic number 47 and the chemical symbol **Ag**. It has the electron configuration [Kr] $4d^{10}\ 5s^1$ and crystallizes in a face-centered cubic lattice with a lattice constant of $a_{\mathrm{Ag}} \approx 4.085\,\text{Å}$, as depicted in Figure 3.6. The (001) surface is a cut along a face of the cubic unit cell, thus exhibiting a fourfold rotational symmetry with the lattice constant $a_{001} = a_{\mathrm{Ag}}/\sqrt{2} \approx 2.89\,\text{Å}$ and a layer spacing of $d_{\mathrm{Ag}} = a_{\mathrm{Ag}}/2 \approx 2.04\,\text{Å}$. The surface atoms are arranged highly symmetric, so no reconstructions can be observed on the clean surface. The only reaction to the broken symmetry at the surface is a relaxation of the topmost layers, meaning a variation in the interlayer spacings near the surface.

Due to its minor deviations from bulk positions and simple quadratic surface unit cell, the Ag(001) surface is an particularly good material system to examine the influence of experimental aspects of LEED [13], since a very good agreement between experiment and calculations has been achieved [37, 38]. Within this thesis, no actual silver crystal is used, however, the Ag(001) surface is used to compare the results of different approaches to the calculation of LEED spectra.

4. Experimental Setup

In this chapter, the experimental setup used for the experiments as part of this thesis is presented.

4.1. UHV Chamber

On the one hand, the **U**ltra **H**igh **V**acuum (UHV) chamber is necessary to operate the LEED optics. On the other hand, the structures of the investigated surfaces in this thesis are sensitive to contamination of adsorbates. The UHV chamber is therefore a means to minimize the interaction between the surface and the gas phase.

The chamber used in this thesis is schematically depicted in Figure 4.1 and was designed and taken into operation as a part of the work within this thesis. The chamber is equipped with a LEED optics and an effusion cell to enable in-situ measurements. The valve, transfer rods and load lock allow the exchange of samples without breaking the vacuum inside the UHV chamber. The manipulator can move the sample inside the chamber in all spatial directions linearly. Additionally, two independent rotations are possible, enabling the adjustment of the sample in front of the effusion cell and LEED optics.

The base pressure inside the UHV chamber of 1×10^{-10} mbar is achieved by a combination of different pumps. A dry scroll pump creates the vacuum necessary to operate the two turbo-molecular pumps, which are attached to the UHV chamber and load lock, respectively. An ion getter pump provides, in combination with a titanium sublimation pump, the base pressure of the UHV chamber.

The sample on the sample holder can be heated by direct current, while the temperature of the sample can be monitored by an infrared pyrometer through a view port and a thermocouple, attached to the manipulator in proximity to the sample. Additionally, the manipulator can be cooled by liquid nitrogen, allowing measurements at low temperatures.

4.2. Effusion Cell

To apply material onto the substrate for self-induced reconstructions, the technique of physical vapor deposition is used. This can be done using an effusion cell as depicted schematically in Figure 4.2. Inside a crucible made of tantalum, the material to be evaporated is stored. The crucible is heated by the bombardment of free electrons, generated by thermionic emission at the filament, that are accelerated by a high voltage applied to the crucible. The rise in temperature of the crucible leads eventually to the evaporation of the material inside, forming a molecular beam due

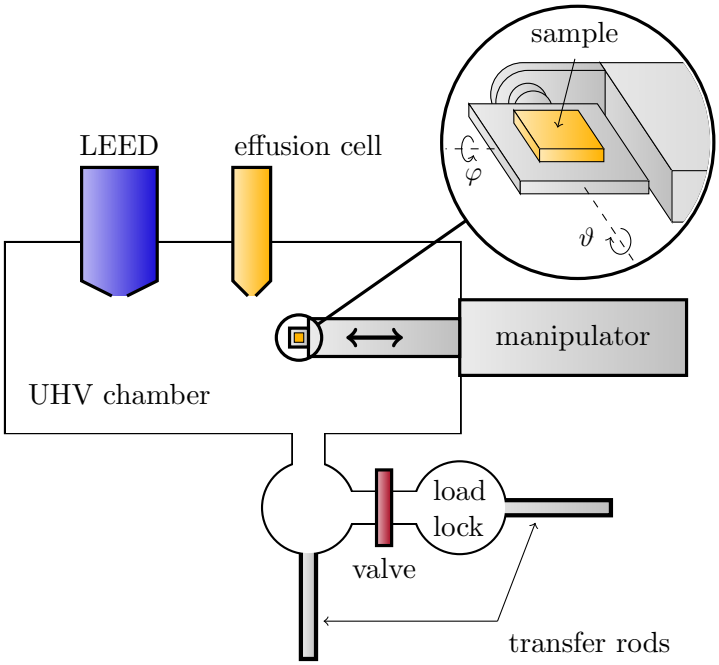

Figure 4.1.: Schematic sketch of the UHV chamber used for the experiments presented in this thesis. The pumping system is omitted. The transfer rods allow to convey the sample from the load lock to the manipulator, on which it can be placed in front of the effusion cell or LEED optics. The manipulator allows the linear movement of the sample on three axes and rotations around two axes. Furthermore, it enables the cooling of the sample with liquid nitrogen.

to the apertures. The flux of the molecular beam can be controlled by the power of the electrons impinging on the crucible. The shutter allows the precise control of the time the substrate is exposed to the beam and thus the amount of material deposited onto the sample. To prevent a rise of pressure inside the UHV chamber due to the heating of the whole effusion cell, a copper body that can be cooled by water encloses the crucible.

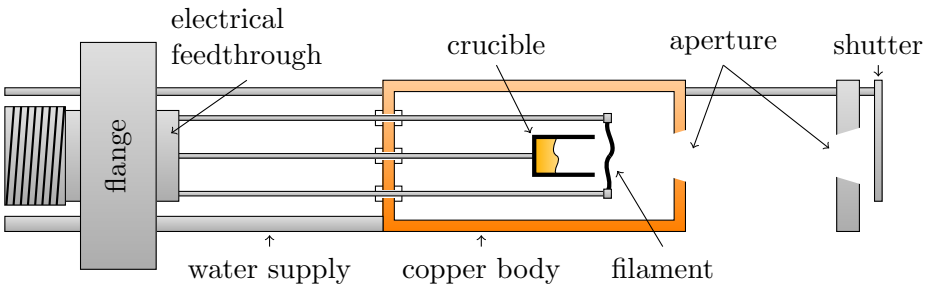

Figure 4.2.: Schematic sketch of an effusion cell used for physical vapor deposition. The material to be evaporated is stored in the crucible, which can be heated by electron bombardment. A water supply cools the body of the effusion cell, while the shutter is used to control the emission.

4.3. Sample Preparation

The silicon substrates are cut from commercial silicon wafers to a size of approximately $2 \times 0.5\,\mathrm{cm}^2$ to allow the mounting on the sample holder. After removing splinters and dust in a stream of nitrogen gas, the sample is transferred into the UHV and heated to 600 °C by direct current to desorb remaining adsorbates for at least 12 h. Afterward, the native SiO_2 layer is removed by repeated cycles of *flash-annealing*. Therefore, the sample is heated quickly up to 1200 °C by direct current within a few seconds. After reaching this temperature, the direct current is stopped so the sample can cool down to 500 °C. The pressure may not exceed 1×10^{-8} mbar within this procedure. This cycle is repeated approximately 5 times and can also be used to remove the material brought onto the sample by means of physical vapor deposition, so the same sample can be used for multiple preparations. The LEED patterns of the (2×1) and (7×7) reconstruction for Si(001) and Si(111) respectively, verify a clean, adsorbate free surface.

To prepare the gold-induced reconstructions investigated in this thesis, the crucible of an effusion cell was equipped with a gold wire. Upon heating, the gold wire is melted and then evaporates into the vacuum. The amount of gold brought onto the sample is controlled by the opening time of the shutter for a fixed heating power applied to the crucible. This approach gives no access to the absolute amount of gold brought onto the substrate, but allows to vary the evaporation time to achieve the right amount for the well-known (5×2) reconstruction. The silicon substrate is heated to 750 °C while exposed to the gold beam. Directly after the preparation, the sample is cooled with liquid nitrogen to −170 °C for the conduction of the LEED measurements.

4.4. MCP-LEED

The diffraction experiments in this thesis were performed with a commercial LEED optics by *OCI* (Model BDL800IR-MCP1). Opposed to the schematic sketch depicted in Figure 2.1, this optics has no spherical screen. Behind the grids, a **m**icro-**c**hannel **p**late (therefore MCP-LEED) multiplies the elastically scattered electrons by secondary emission. Behind the (flat) micro-channel plate, a flat luminescent screen is located to enable the observation of the diffracted beams. With this setup, the diffraction pattern appears to be distorted, compared to a conventional LEED with a spherical screen. For the analysis of the reflex intensities this distortion is irrelevant, since neither the shape nor the exact positions of reflexes is crucial for a structural analysis, it is only the intensity of the beams that must be recorded properly. However, the multiplication of electrons allows the usage of lower beam currents for the LEED experiment. This can be beneficial for delicate material systems, whose structure can be altered by the interaction with the LEED electrons, as the Si(001) surface for temperatures below 40 K [39].

4.5. Data Acquisition

The diffraction patterns were recorded with a commercial camera by *Unibrain* (Fire-i 580b) equipped with a lens by *Ricoh* (ricoh tv lens 12mm 1:1.2). The resulting images were then processed by two *Graphical User Interfaces* (GUIs), which were developed within the work for this thesis. The first GUI extracts the IV spectra from the collection of images using circular ROIs. The positioning of the ROIs works automatically, but can also be corrected manually, if necessary. The second GUI is used to revise the spectra. This includes the concatenation of separate parts (if the full data set was recorded within different measurements) as well as the removal of artifacts like sudden jumps in intensity and negative intensities. Furthermore, a Savitzky-Golay filter can be used to improve the smoothness of the spectra. This is important, since the Pendry R factor uses the logarithmic derivative of the spectra and thus outputs high values if any noise is contained in the experimental spectra. Additionally, within this second ROI, beams that are expected to be equivalent due to symmetry can be averaged.

The dynamical scattering calculations were conducted with CLEED [16], which also compares the calculated spectra to the revised averaged experimental spectra. To improve the automatic variation of parameters to the calculations, a *wrapper* for CLEED was programmed and used.

5. Structural LEED Analysis of the Reconstructed Si(001) Surface

5.1. Introduction

Due to their role in the semiconductor technology, silicon surfaces have always been of particular interest. To understand the electronic properties of the surface, on which the devices are manufactured, knowledge of the atomic geometry is important. While the formation of dimers on the Si(001) surface was undoubted, it took many years to obtain accurate structural data, although much effort was taken [29, 30, 40–45]. Two main problems have been, on the one hand, the sensitivity of the reconstruction to adsorbates on the silicon surface, complicating a proper preparation and measurement of experimental data. On the other hand, computational performance was not comparable to today's possibilities, impeding the calculation of the scattering and full theoretical methods like DFT. Hence, early attempts of a structural LEED analysis in the 1980s were likely to not succeed [40, 42], relying on high quality experimental data and the computational costly dynamical diffraction theory. Only more than 20 years later conclusive results could be achieved by LEED studies [39, 46]. Today, investigations of the reconstructed Si(001) surface are still useful to test new methods, which can be expanded toward more complicated systems that are in reach for today's resources.

5.2. Experimental Details

For the structural LEED analysis of the Si(001) surface, commercial Si(001) wafers (n-doped, resistivity of 7-10 Ω cm) were used. The choice of the dopant has negligible influence on the results of the structural analysis of Si(001)[39]. The surface was prepared by repeatedly flash annealing the sample with direct current to 1200 °C. After preparation, the sample was cooled down to 105 K using liquid nitrogen. IV LEED data were recorded from 63-430 eV in 1 eV steps. At each energy, a camera using an exposure time of 50 ms per frame averaged 20 frames to obtain the final diffraction pattern. The Si(001) surface is sensitive to contamination, which has a serious effect on the arrangement of the dimers [47] . Due to this degradation of the surface, the energy range was split into three parts. Between those parts, the sample was flash annealed to ensure a clean surface throughout the full energy range. The diffraction patterns exhibited a fourfold symmetry as expected for a Si(001) surface with rotational domains due to mono atomic steps. Therefore, 13 inequivalent beams were recorded which yield a total energy range of 2603 eV. The quarter order reflexes could not be evaluated properly due to low intensities and

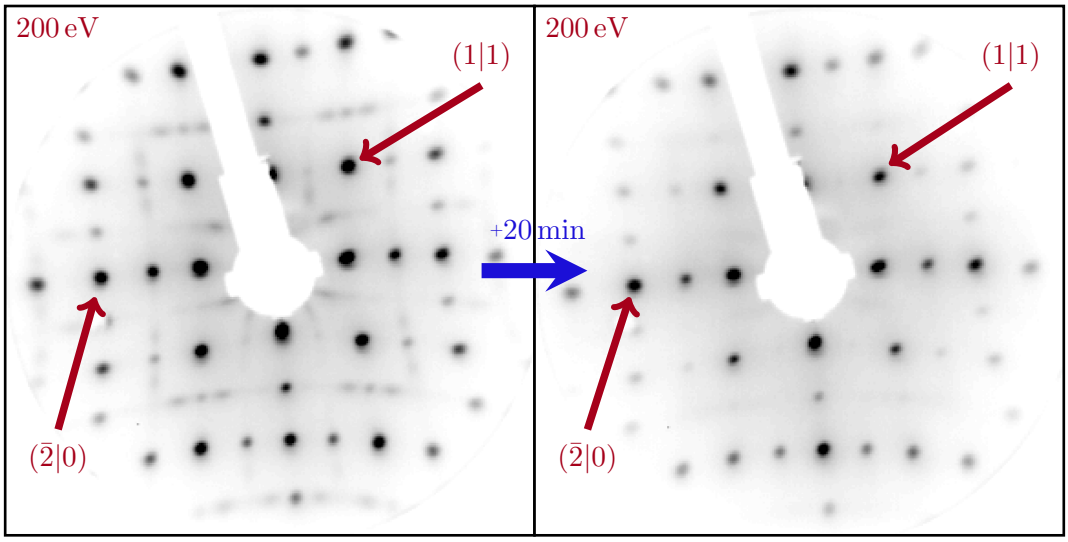

Figure 5.1.: Diffraction pattern of Si(001)-c(4 × 2). Directly after flash annealing, the cooled sample exhibits a c(4× 2) pattern. After 20 min, the quarter order reflexes are gone due to the interaction with residual gases. The distortion of the pattern is caused by the MCP-LEED optics.

fast degradation due to the contamination. In Figure 5.1, a diffraction pattern of the freshly prepared surface can be found, exhibiting quarter order reflexes of the c(4 × 2) reconstruction. After 20 min in the UHV chamber without any further incident electron beam, these quarter order spots vanish leaving only slight streaks. This effect could be explained with the increasing density of so-called *type-C* defects originating from the surface with the residual gas [47].

5.3. IV LEED Analysis

The CLEED package [16] was used to calculate theoretical spectra. The atomic scattering was simulated by thirteen phase shifts ($l_{\max} = 12$) obtained by the Barbieri-van Hove phase shift calculation package [48]. Damping was represented by an imaginary part of the inner potential of 3.8 eV. The angle of incidence of the electron beam as well as the isotropic thermal vibrational amplitudes were optimized. The Pendry R factor (R_P) [14] was used to evaluate the difference between experimental and calculated spectra to direct the automatic optimization of parameters.

5.3.1. Optimized model

The best agreement between experimental and calculated spectra was achieved by a c(4×2) reconstruction of the topmost nine layers, yielding an R_P of 0.048. Figure 5.2 shows the experimental IV curves and calculated spectra of the best fit model. The maxima and minima coincide very well. Apart from deviations in relative intensities of different maxima, especially at lower energies, the agreement of spectra is very

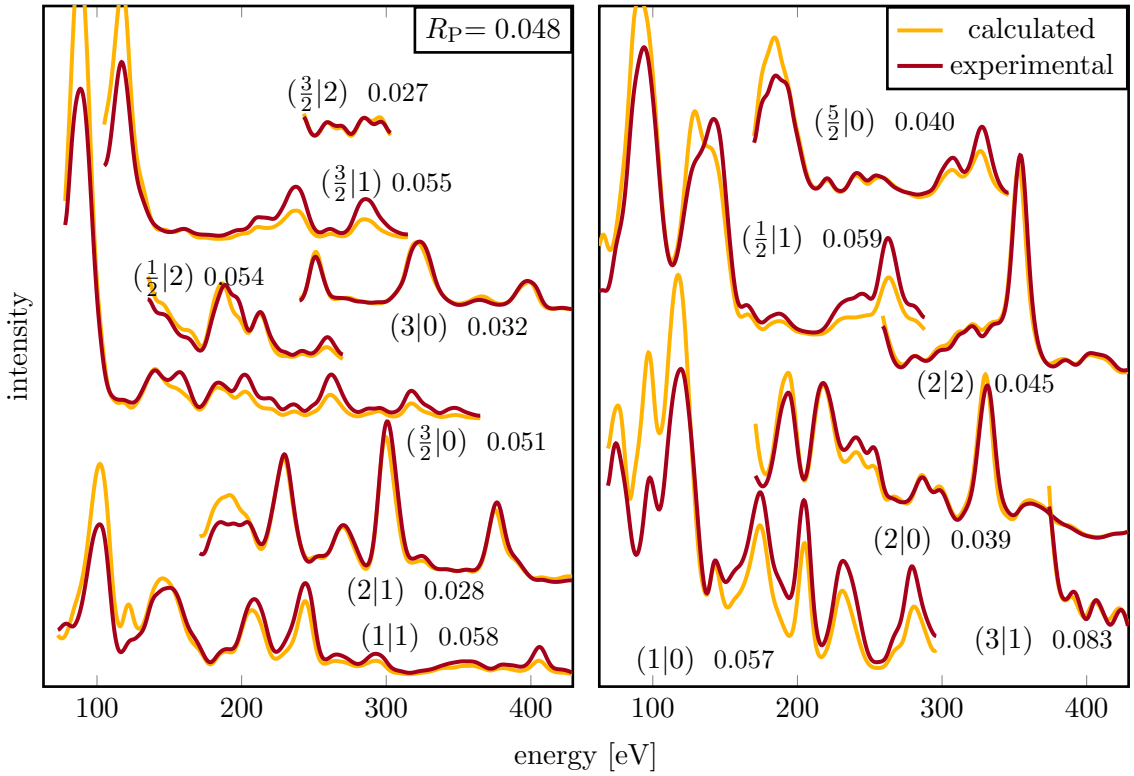

Figure 5.2.: Calculated IV spectra (yellow) of the best fit model in comparison with the experimental spectra (red). The different beams are shifted along the ordinate for better visibility. For each pair the index of the respecting beam is given as well as the Pendry R factor. The overall Pendry R factor is 0.048.

good. A visualization of the model is given in Figure 5.3. The optimization of atomic positions was conducted conserving a *p2mm* symmetry which leads to a reduction of free parameters. The bulk-terminated surface was used as a starting point for the optimization. The corresponding coordinates for inequivalent atoms can be found in Table 5.1. The uncertainties were determined using the variance of R_P ($\mathrm{Var}_{(R_\mathrm{P})} = R_{\mathrm{P,min}}\sqrt{8|V_\mathrm{i}|/E_\mathrm{T}}$) deduced from the imaginary part of the inner potential V_i and the total energy range E_T. The results are in excellent agreement with previous detailed LEED studies on this reconstruction [39, 46] and *ab initio* DFT calculations [49]. The redundancy for this model is $\rho \approx 4.2$, thus indicating that the amount of experimental data supports the number of parameters within this model.

5.3.2. Detailed analysis

Figure 5.4 shows the derivation of the uncertainties of exemplary atoms. The position of a single atom was varied, while all other atoms were fixed. The uncertainties were determined by the displacement necessary to raise R_P over the value of $R_{\mathrm{P,min}} + \mathrm{Var}_{(R_\mathrm{P})}$. This analysis was done for every single atom, however, curves

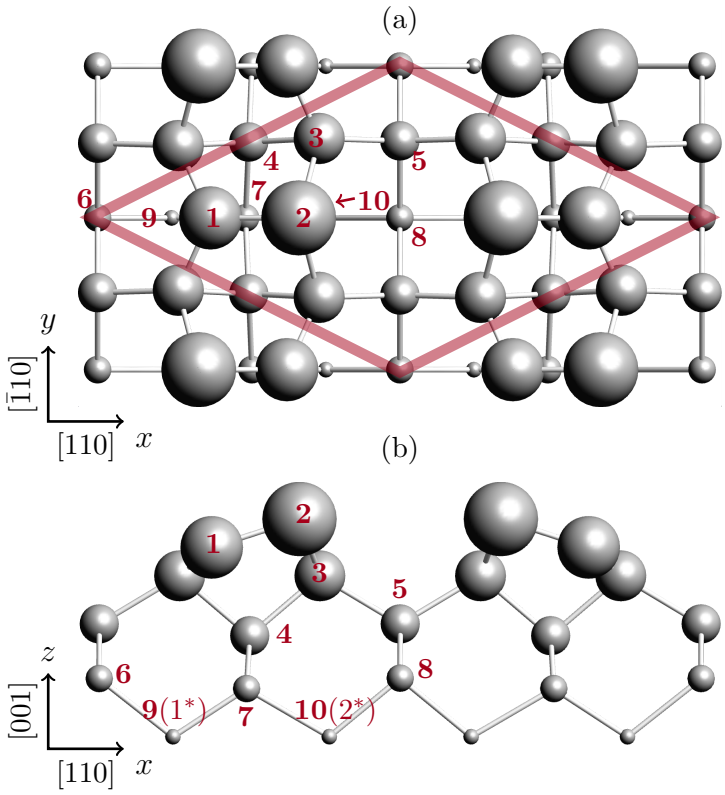

Figure 5.3.: Structure model of the Si(001)-c(4 × 2) reconstruction in top view (a) and side view (b). The silicon atoms are represented by gray spheres. Their diameter decreases with increasing distance to the surface for better clarity of the view from top. The primitive unit cell is marked by a red rhomboid, while the inequal atoms are denoted with red numbers. The side view is a cut along the ($\bar{1}10$)-plane. Only the top five layers are shown corresponding to the height of a cubic bulk unit cell.

Table 5.1.: Atomic coordinates of the best fit structure. Values are given as displacement from the bulk positions. Atom numbers correspond to Figure 5.3. Numbers with asterisks indicate identical lateral bulk positions, but a deeper layer.

Layer	Atom	Δx [Å]	Δy [Å]	Δz [Å]
1	1	0.96 ± 0.07		-0.605 ± 0.018
	2	-0.60 ± 0.08		0.118 ± 0.018
2	3	-0.13 ± 0.04	-0.05 ± 0.14	0.024 ± 0.013
3	4			-0.160 ± 0.017
	5		0.06 ± 0.14	0.157 ± 0.013
4	6			0.103 ± 0.027
	7	0.14 ± 0.19		-0.132 ± 0.027
	8			0.132 ± 0.024
5	9(1*)	-0.06 ± 0.08		-0.009 ± 0.024
	10(2*)	0.08 ± 0.07		-0.016 ± 0.022
6	3*	0.04 ± 0.04	-0.03 ± 0.10	-0.007 ± 0.010
7	4*			0.027 ± 0.031
	5*		0.03 ± 0.11	-0.040 ± 0.014
8	6*			-0.028 ± 0.026
	7*	-0.01 ± 0.12		0.022 ± 0.020
	8*			-0.028 ± 0.027
9	1**	0.03 ± 0.12		0.007 ± 0.030
	2**	0.03 ± 0.15		-0.022 ± 0.035

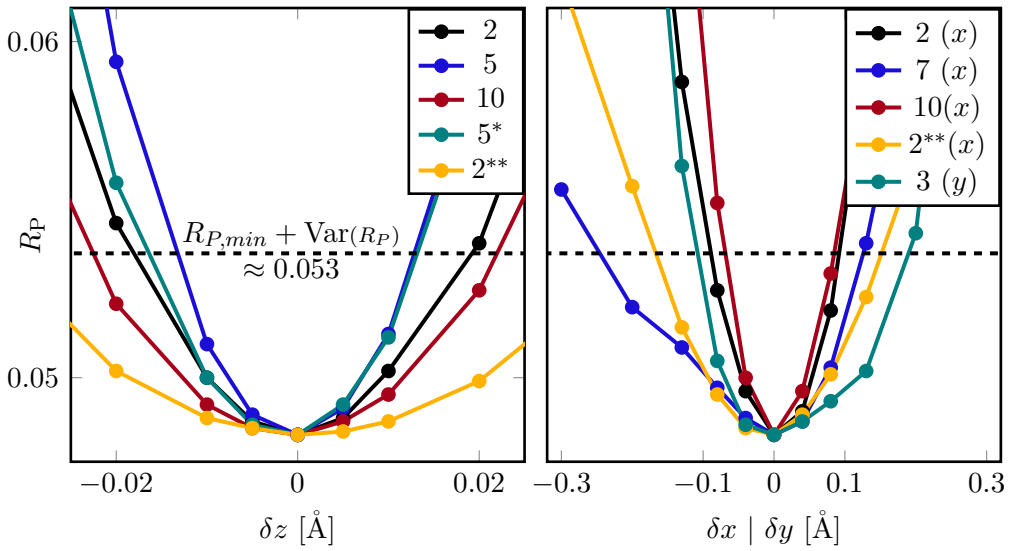

Figure 5.4.: Dependence of the Pendry R factor (R_P) from the displacement of a single atom relative to its best fit position (δz, δx, δy) while holding all other positions constant. The plots are divided into lateral and vertical displacements due to the different sensitivity of backscattered electrons on the respective displacements.

for only exemplary atoms are displayed in Figure 5.4. The uncertainties for lateral displacements are, as expected, significantly larger than for vertical displacements due to the high sensitivity of backscattered electrons on the vertical position. Surprisingly, the IV spectra are more sensitive to the vertical position of atom 5* in the seventh layer than of atom 2 on the surface. This proves the validity to include the deeper layers in this analysis. Varying its depth, atom 2** in the ninth layer exhibits a much wider opening of the curve and hence an increased uncertainty. This is the reason why no more than nine layers were included in the optimization. Interestingly, some of the R_P values for lateral displacement show a steep slope in one direction, while much more shallow in the opposite direction. Further investigation on this effect can be found in section 5.5.

Due to the covalent bonds of silicon, the dimerization is expected to cause reconstructions of several layers. To investigate this effect further, models with varying number of reconstructed layers were optimized. Figure 5.5 (a) shows the improvement of the Pendry R factor for an increasing number of layers included in the optimization. Generally, increasing the number of layers in the optimization also improves R_P. The inclusion of different vibrational amplitudes for the top five layers achieves convergence in R_P. Their optimized values change smoothly from a radial root mean square displacement of 0.12 Å at the first layer toward 0.06 Å as bulk value. The inclusion of different vibrational amplitudes for the top layers is motivated by the covalent bonds of silicon, making an influence of the increased vibrational amplitude at the surface toward deeper layers plausible.

Interestingly, for the inclusion of an increasing number of layers within the opti-

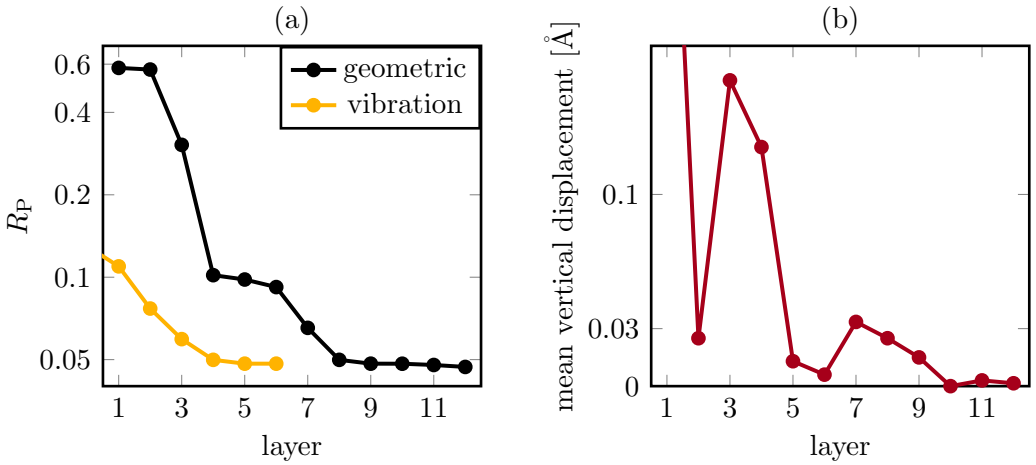

Figure 5.5.: (a) R_P as a function of the number of optimized layers (geometrical parameters in black; vibrational amplitudes in yellow). (b) Average displacement per layer for an optimized model including twelve layers.

mization, there are two major improvements with the layers three and four as well as with the layers seven and eight for the geometrical parameters. In between, R_P is rather constant. Thus, increasing the number of layers included in the optimization process from four to six, no improvement is observed, while the number of geometrical parameters is increased. In Figure 5.5 (b) the averaged vertical displacement of each layer is plotted. Here, two peaks of stronger displacements for the layers 3,4,7 and 8 can be seen, meaning they exhibit a displacement greater than that of surrounding layers. The same tendency can be seen for layers 11 and 12, although much less prominent. Here, it should be noted that the cubic bulk unit cell of silicon consists of four layers, meaning that every fourth layer has the same lateral position and identical chemical surrounding. Hence, this kind of periodicity in every fourth layer is expected to stem from the directed bonds of silicon, which allow different layers a different amount of absorption of the stress induced by the dimerization.

On the one hand, these deep reconstructions make the treatment of covalent bonded substrates with IV LEED challenging, since one needs to include much more parameters to achieve a conclusive result. This was a major drawback in the past, when computing resources were not comparable to today's and explains why previous attempts yielded rather ambiguous results [30, 42] when including an insufficient number of reconstructed layers. On the other hand, these reconstructions can be understood easily in terms of elastic strains. Thus, the Keating model [27] for elastic strain energy can be applied.

5.4. Accelerated Structure Optimization with Keating Energy

The model for the elastic strain energy in covalent crystals, as proposed by Keating [27] (cf. section 2.4) allows the determination of the Keating energy, a quantity

derived from the deviation of bond angles and lengths from their equilibrium values. Hence, minimizing the Keating energy by optimizing atomic positions should yield structural parameters that compensate the strain induced by the dimerization of the Si(001) surface. This can be used to predict the displacements of near surface atoms from their bulk positions to improve the starting positions of the atoms of a model, which in return saves efforts in the computationally more costly calculations of dynamical diffraction theory. This has already been shown for *ab initio* calculations and X-ray diffraction data [28].

Application

Since the Keating energy is based on the deviation of bond lengths and angles from their bulk value, inaccuracies are expected, when facing dangling bonds of a surface or heavily distorted bonds. Since both are to be expected at the reconstructed Si(001) surface, it is reasonable to exclude the topmost layer from a structure optimization with the Keating model (in Figure 5.3 atoms number 1 and 2). In the following, only silicon atoms with four covalent bonds will be considered for any calculation of the Keating energy.

In a first step, the coordinates of the topmost and tenth layer of a bulk terminated surface were fixed. The atoms of the remaining eight layers in between were randomly displaced (up to 0.86 Å in random directions). Then, a *simulated annealing* algorithm optimized the positions to minimize the Keating energy and find the global minimum. At convergence each atom was closer than 0.001 Å to its bulk position, so it can be concluded that the algorithm combined with the Keating energy enables a relaxation of the atomic positions.

Next, the atoms of the topmost layer were fixed at their respective best fit values from the previous IV LEED analysis. Afterward, the eight underlying layers were optimized to minimize the Keating energy. Thereby, the validity of the Keating energy to estimate the displacements of the subsurface layers can be analyzed.

Results

The differences between the LEED and the Keating model are represented in Table 5.2. The overall agreement is very good. The deviations are within the uncertainty of the LEED analysis and are, with one exception, less than 0.1 Å. The deviation of atom 3 in layer 2 is rather high due to the strong distortion of the bonds near the surface, which is expected for the Keating model. Atom number 7 has by margin the biggest deviation. Interestingly, the LEED analysis also resulted in a high uncertainty of the position of this atom with the largest uncertainty of all atoms. Figure 5.7 shows the dependence of the Keating energy from the displacement of a single atom. For all atoms, the Keating energy exhibits a very similar parabolic shape as opposed to the analogues curves of the LEED analysis, which exhibit more differences between the single atoms and often asymmetric shapes (cf. Figure 5.4). A possible explanation lies in the unit cell of the reconstruction (see further discussion

layer	atom	Δr [Å]	$\Delta\alpha$ [°]	Δr_L [Å]
2	3	0.075	28.0	0.141
3	4	0.021	0.0	0.160
	5	0.092	32.6	0.168
4	6	0.018	0.0	0.103
	7	0.158	55.4	0.192
	8	0.066	0.0	0.132
5	1*	0.019	12.5	0.060
	2*	0.040	5.5	0.081
6	3*	0.040	47.5	0.050
7	4*	0.008	0.0	0.027
	5*	0.037	36.5	0.050
8	6*	0.014	0.0	0.028
	7*	0.012	24.4	0.024
	8*	0.014	0.0	0.028
9	1**	0.022	10.9	0.030
	2**	0.044	146.7	0.037

Table 5.2.: Deviations between the best fit LEED model and the surface relaxed by minimization of Keating energy. Δr denotes the total distance between the corresponding atoms, while $\Delta\alpha$ indicates the difference of the directions of the respective displacement from the bulk values between the LEED and Keating model (0 ° equals same; 180 ° equals opposite direction of displacement, so small angles are desirable, cf. Figure 5.6). The atom numbers correspond to Figure 5.3 and Table 5.1. As a reference, the displacement of the respective atoms within the optimized LEED model (Δr_L) is also given.

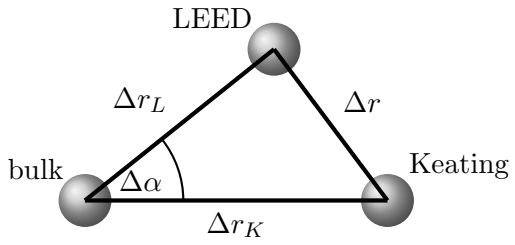

Figure 5.6.: Schematic sketch for the definition of the parameter Δr and $\Delta\alpha$ used in Table 5.2. The three gray spheres represent the positions of the same atom in the three different structures (bulk-terminated surface, LEED optimized model and Keating optimized model).

in chapter 5.5). Notably, the Keating energy increases similarly for lateral and vertical displacements from the relaxed structure.

Big deviations in the direction of the displacement ($\Delta\alpha$) occur especially when the displacements are small, diminishing the significance of these deviations. Notably, the angles for atoms 4,6 and 8 are correct, indicating that the structure optimization guided by the Keating energy indeed respects the symmetry restrictions, since those atoms are only allowed to be displaced vertically. To evaluate the significance of the deviations, the model based on the minimization of the Keating energy was used to calculate IV spectra to shed light on the consequences of these deviations regarding a structural LEED analysis.

The IV spectra of the model derived by the minimization of the Keating energy yield $R_\mathrm{P} = 0.172$. While improving the R factor significantly in comparison to only one or two relaxed layers ($R_\mathrm{P} \approx 0.6$), an optimization of all layers using IV LEED appears to be inevitable to achieve good agreement between experiment and calculation. Nonetheless, the elastic strain model by Keating can be helpful to improve the starting position for an IV LEED analysis for covalent substrates, especially if there are no models of more precise approaches like DFT. The averaged displacement of all

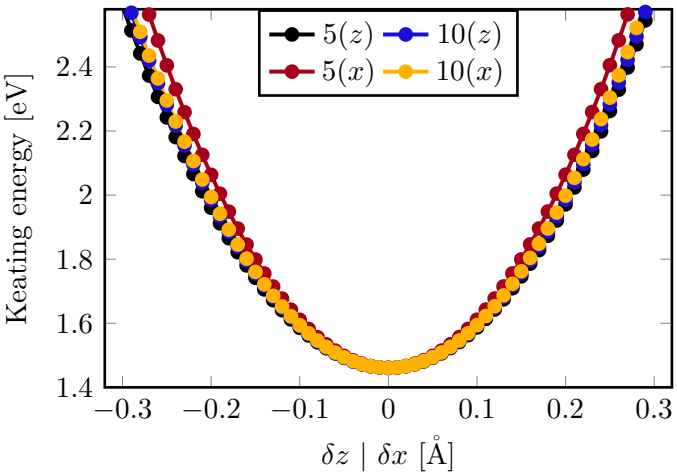

Figure 5.7.: Dependence of the Keating energy from the vertical (δz) and lateral (δx) displacement of a single atom (while holding all other positions constant) exemplarily for two different atoms. The atom numbers correspond to Figure 5.3 and Table 5.1.

atoms of the layers two to nine of the LEED best fit model from their bulk positions is 0.0853 Å, while the averaged displacement between the Keating energy minimized surface and the LEED model is only 0.0462 Å. In other words, approximately half of the way from bulk structure toward the final LEED model for the subsurface layers can be done using the computational much less demanding approach using the Keating energy. Unfortunately, the position of the top layer must be known for this optimization. In practice, an iterative scheme, like optimizing the surface layer by LEED, then relaxing the subsurface layers with the Keating energy, repeated until convergence, could be used.

The tensor approximation also allows an enormous acceleration in the structural optimization for large systems. However, for displacements far away from the reference structure, the approximation loses accuracy, so full dynamical calculations have to be performed repeatedly for reliable results. In this case, a first relaxation using the Keating energy can also be helpful to improve the starting model. In most practical use cases, the tensor approximation yields reliable spectra for a displacement of up to 0.4 Å [10].

Summarizing, the approach using the Keating energy to estimate the displacement of subsurface layers does work in principle. However, the deviation from the optimized model by LEED calculations is still significant. Since the Keating formalism is not easily extended generally toward highly distorted bonds at the surface and unsaturated bonds, it can only be applied reliably to the sub-surface layers. However, these layers feature a rather small displacement and can therefore be treated more efficiently by Tensor LEED. The only case, where the Keating energy might have reasonable application within a LEED optimization, is the investigation of new structure models. Thereby, the Keating energy allows the improvement of many atomic positions to obtain a superior reference structure compared to using bulk positions.

layer	atom	Δx [Å]	Δz [Å]
1	1	0.05	0.010
	2	0.08	0.004
2	3	0.00	0.009
		−0.04	−0.008
3	4	0.03	−0.008
	5	−0.01	0.004
4	7	0.19	0.010
	8	0.03	0.017
5	9(1*)	−0.02	0.005
	10(2*)	0.00	−0.008
6	3*	−0.04	0.022
		−0.03	0.011
7	4*	−0.07	−0.004
	5*	−0.03	0.004
8	7*	0.06	0.001
	8*	0.02	0.001
9	1**	0.05	0.033
	2**	0.07	−0.022

Table 5.3.: Deviations between the optimized LEED models for the c(4 × 2) and the (2 × 1) reconstruction. Δx and Δz denote the lateral displacement in x-direction and the vertical displacement, respectively. Δy was omitted, since all atoms are bound to their respective y bulk values in the (2 × 1) model due to symmetry. The atom numbers correspond to Figure 5.3. For atoms 3 and 3* two values are given, while atoms 6 and 6* are missing, because of multiple, respectively no equivalent atoms in the different models.

5.5. Comparison of the c(4×2) and (2×1) Structure Models

The fast degradation of the surface indicates that the data collected for the LEED analysis could include the diffraction of parts of the surface that are reconstructed differently than the c(4 × 2) superstructure. Since the diffraction pattern transforms into a (2 × 1) periodicity, it is consequential to assume a (2 × 1) reconstruction with a buckled dimer. It should be noted that these two reconstructions have different symmetries. While the c(4 × 2) reconstruction has *p2mm* symmetry, a (2 × 1) reconstruction exhibits only *pm* symmetry. Hence, the number of geometrical parameters remains almost unchanged, due to the loss of the mirror plane, although the size of the unit cell is halved.

An optimized model yields a Pendry R factor of 0.059, which is only slightly worse than the best fit of the c(4 × 2) reconstruction. The deviations between the two models are denoted in Table 5.3. Overall the values are within the uncertainty of the LEED analysis, but apparently the deviation of atom 7 is by far the greatest. In the c(4 × 2) reconstruction, the atom in the layer above (number 4) is bound laterally by symmetry requirements. So any stress acting on atom 4 must be compensated by a displacement of atom 7. However, if one considers a (2 × 1) reconstruction, the different symmetry allows a lateral displacement of atom 4, so part of the stress can be accommodated leading to a much smaller displacement of atom 7. If the positions of two equivalent atoms differ much for the two unit cells, a large insecurity in the LEED analysis is expected, if both unit cells can be found simultaneously on the surface, since the recorded intensity is a result of the incoherent superimposition of diffraction at the two structures.

However, the Keating energy predicts a displacement of atom 7 for the c(4×2) reconstruction much more similar to the LEED result for the (2×1) model. Shirasawa et al. found a displacement for this atom (in a c(4 × 2) reconstruction) much more similar to the here presented values for the Si(001)-c(4 × 2) model [46]. Notably, their uncertainty for this atom was also slightly higher than that for surrounding atoms.

The comparison of the calculated IV spectra of the c(4 × 2) and (2 × 1) reconstruction yields $R_P = 0.044$. Thus, the two models are practically indistinguishable by means of IV LEED. This is due to the small deviations in most positions, so the structure of the dimers in both models is comparable. Furthermore, the influence of adjacent dimers on the IV spectra seems to be negligible. The observation of reflexes originating from a c(4×2) periodicity alone, does not ensure that the whole surface is covered by this reconstruction. An additional presence of disordered domains causing a diffraction pattern of a (2 × 1) is not to be excluded easily. It can be assumed that the distinction between a unit cell consisting of repeating sub-unit cells, which are aligned in a certain way, and a surface that is covered by the same sub-unit cells without any alignment, is generally problematic within IV LEED.

5.6. Conclusion

An optimized structure model for the c(4 × 2) reconstruction of the Si(001) surface was presented, which is overall in very good agreement with previous LEED analyses [39, 46] and DFT calculations [49]. The position of one atom deviates rather strongly, for which the causes remain uncertain, although it was proposed as an effect of the transformation of the c(4 × 2) superstructure to the (2 × 1) reconstruction.

Furthermore, the usefulness of the elastic strain model proposed by P. N. Keating [27] to improve initial positions for a structural LEED analysis was examined. The model predicts overall a satisfying agreement with the LEED results, but has deviations especially for the strongly strained top layers. For the Si(001) surface, the computational effort to reach convergence can approximately be halved, using only full dynamical scattering calculations. However, Tensor LEED is the superior approach to speed up the optimization of many parameters.

Finally, it was shown that the structural analysis by IV LEED is not able to distinguish sufficiently between the c(4 × 2) and (2 × 1) superstructures. Therefore, it is still questionable whether the c(4 × 2) ground state really covers the whole surface at low temperatures or disordered domains are still present.

6. Structural LEED Analysis of Si(111)-(5×2)-Au

The Si(111)-(5×2)-Au reconstruction was first observed more than 50 years ago [3]. Since then, this surface has been studied intensively and many suggestions about its geometrical structure have been made [50–58]. Since the surface can be regarded as a prototype of self-assembled quasi-one-dimensional metallic chains, its atomic structure is of fundamental importance to understand its physical properties. More recently, the Au coverage for the models was revised, leading to the Erwin-Barke-Himpsel-model (EBH [4]), the Abukawa-Nishigaya-model (AN [59]) and the Kwon-Kang-model (KK [5]). Surface X-ray diffraction (SXRD) experiments conducted by Shirasawa et al. [60] could rule out the AN model, while preferring the KK model over the EBH model, supporting the theoretical work of Seino et al. [61]. Due to the geometrical similarity of the EBH and KK models, a clear distinction by experimental means is not easy to achieve. Using low-energy electron diffraction (LEED) for the first time on this complex reconstruction promises to give new insights with its high sensitivity on the geometrical structure.

6.1. Experimental Details

The experiments were conducted using commercial Si(111) wafers (p-doped, resistivity of 1-20 Ω cm). The substrate was cleaned by repeatedly flash annealing the sample with direct current to 1200 °C. After cleaning, the temperature of the sample was held at 750 °C and gold atoms were applied by means of physical vapor deposition. Only a very precise coverage led to an exclusive existence of a (5×2) reconstruction, without reflexes of a (7×7) or $(\sqrt{3} \times \sqrt{3})$ superstructure. After preparation, the sample was cooled down to 105 K using liquid nitrogen. IV LEED data were recorded from 60 eV-240 eV in 1 eV steps. At each energy, a camera using an exposure time of 50 ms per frame averaged 20 frames to obtain the final diffraction pattern.

Figure 6.1 shows the diffraction patterns of the Si(111)-(5×2)-Au reconstruction at two different energies. Reflexes of the superstructure are distinctively visible. Their arrangement suggests the presence of three rotational domains on the surface that superimpose incoherently in the diffraction pattern. The streaks caused by a statistical shift of adjacent unit cells (cf. Figure 6.8) can be seen especially prominent in Figure 6.1 (a) at 82 eV (denoted by a yellow arrow). The pattern exhibits a threefold symmetry due to rotational domains, although the absolute intensities differ for symmetry equivalent beams. This can be seen in Figure 6.2 for an exemplary beam. The effect of different absolute intensities of symmetry equivalent beams is assumed to be caused by a different fraction of the surface, which is covered by the

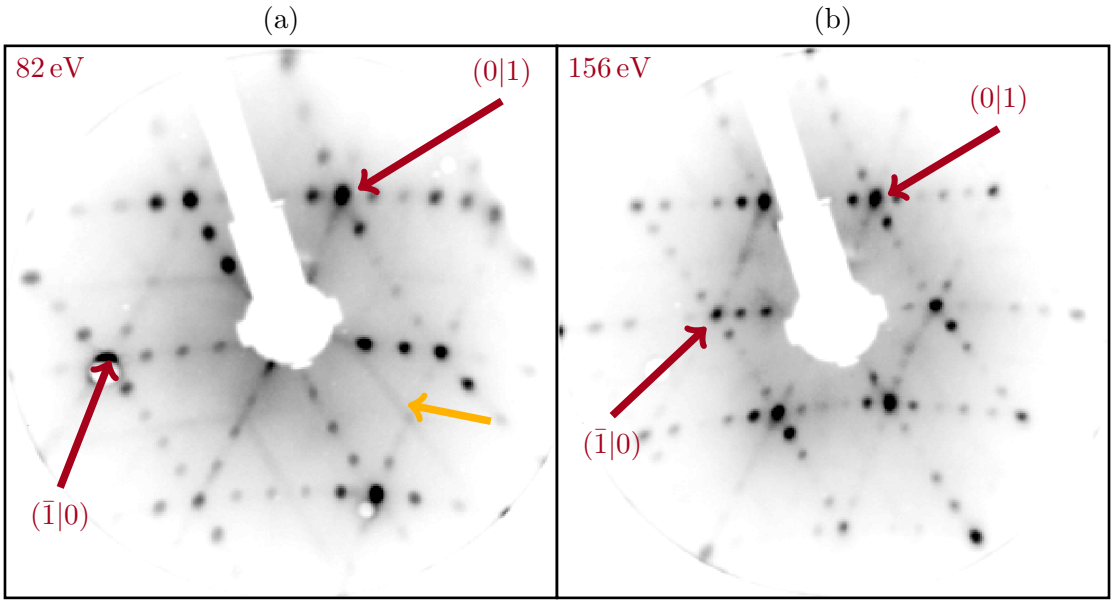

Figure 6.1.: Diffraction patterns of the Si(111)-(5 × 2)-Au reconstruction taken at an electron energies of 82 eV and 156 eV, respectively. Especially at 82 eV the streaks (yellow arrow) caused by the statistical shift of adjacent unit cells of the reconstruction are visible. The distortion of the pattern is caused by the MCP-LEED optics.

respective rotational domains.

While the fractional order spots show a very good agreement in the shape of the IV spectra for symmetry equivalent beams, symmetry equivalent integer order beams exhibit a greater deviation. This is compatible with the assumption of the different share of the respective rotational domains, since the observed reflexes of integer order are a superposition of different beams originating from different rotational domains. In contrast, fractional order beams originate exclusively from a single rotational domain. Altogether, 27 inequivalent beams could be recorded, yielding a total energy range of 3503 eV. The recorded reflexes are shown schematically in Figure 6.3.

6.2. IV LEED Analysis

The CLEED package [16] was used to calculate theoretical spectra. The atomic scattering was simulated by thirteen phase shifts ($l_{\max} = 12$) obtained by the Barbieri-van Hove package [48]. Damping was represented by an imaginary part of the inner potential of 4.9 eV. The angle of incidence of the electron beam was optimized to a value of 1.15°. Furthermore, the isotropic thermal vibrational amplitudes of the atoms were also optimized. The Pendry R factor (R_{P}) [14] was used to evaluate the difference between experimental and calculated spectra and to direct the automatic optimization of parameters.

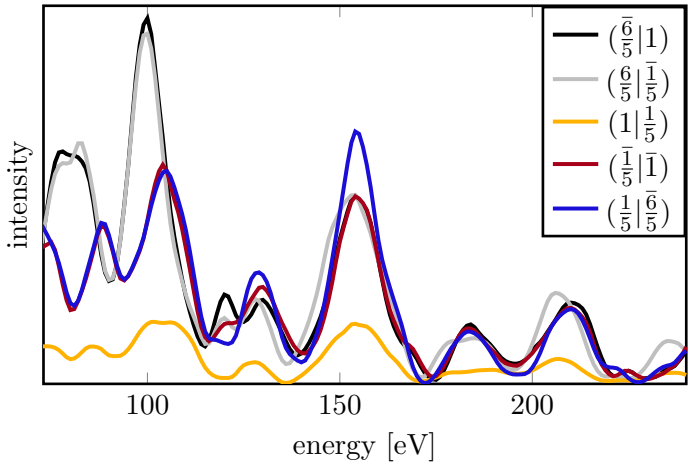

Figure 6.2.: IV curves of symmetry equivalent reflexes (red stars in Figure 6.3). One rotational domain (causing the $(1|\frac{1}{5})$ and the not-evaluated $(\bar{1}|\bar{\frac{6}{5}})$) has a significant lower overall intensity. The differences between the remaining four reflexes is caused mainly by an incident electron beam that is not perfectly perpendicular to the surface.

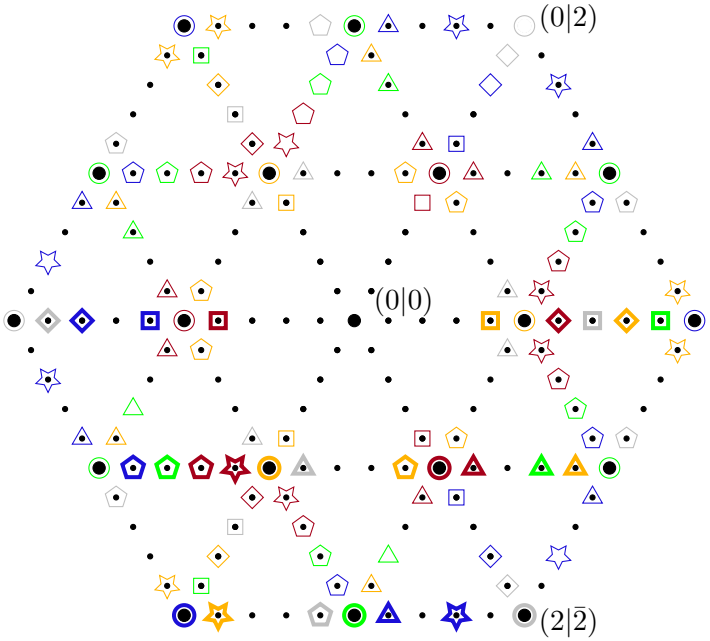

Figure 6.3.: Schematic position of reflexes (black dots) in the diffraction pattern of the Si(111)-(5 × 2). The reflexes used for the LEED analysis (cf. Figure 6.4) are marked by different thick shapes. The final IV curves result from the averaging of symmetry equivalent beams (denoted by thin marks of the same color and shape). Marked reflexes without black dots could not be evaluated due to low intensities or because they were hidden behind the electron gun.

6.2.1. Comparison with the KK and EBH model

Both, the KK and the EBH model can explain the experimental data by XRD, although the KK model is preferred [60]. Furthermore, the AN model could be ruled out. To examine the accordance of the KK and EBH model with experimental LEED data, calculated spectra of both models, each optimized by DFT calculations [49], are compared with the experimental IV spectra. The KK model yields a R_{P} of 0.220, which is overall a satisfactory fit without positions optimized for the LEED analysis. However, the EBH model only yields a R_{P} of 0.399, making it much less conclusive than the KK model. A further discussion can be found in chapter 6.3.

6.2.2. Optimized KK model

The best agreement between experimental and calculated spectra was achieved by an optimized version of the KK model [5] as a starting point, including three silicon bilayers beneath the surface, yielding a R_{P} of 0.117. Figure 6.4 shows the experimental IV curves and calculated spectra of the best fit model. The extrema between experimental and calculated spectra match very well apart from a few exceptions like the $(\bar{1}|0)$ with an exceptional high value of R_{P}. Overall, the integer beams exhibit a worse R_{P} than the beams of fractional order. This might be due to the assumed inequal percentages of the respective rotational domains present on the surface in the experiment, causing the averaging of calculated beams to not correspond to the experiment. The fractional order beams are not affected, since there is no superposition in the diffraction pattern for them.

Figure 6.5 shows a visualization of the optimized model. Atomic positions were optimized, conserving the *pm* symmetry of the nanowires. Due to the shift of the reflection axes of adjacent unit cells, the symmetry was not enforced on the silicon atoms in the center of the honeycomb motif because of the ambiguity. Atoms 8, 9, 14, and 15 were bound according to the symmetry of the nearby gold structure, while atoms 10, 11, 12, and 13 were optimized without any constraints. For the silicon atoms of deeper layers, the same criterion was enforced, depending on their respective positions on the y-axis ($[11\bar{2}]$-direction).

The coordinates for the surface atoms (without underlying silicon bilayers) of the optimized model can be found in Table 6.1, while the coordinates of the silicon bilayers are located in Table B.1 in the appendix. The uncertainties were determined using the variance of R_{P} ($\mathrm{Var}_{(R_{\mathrm{P}})} = R_{\mathrm{P,min}}\sqrt{8V_{\mathrm{i}}/E_{\mathrm{T}}} \approx 0.012$), deduced from the imaginary part of the inner potential V_{i} and the total energy range E_{T} of recorded data. The redundancy for this model is $\rho \approx 1.24$. This indicates that the amount of experimental data supports the number of parameters within this model only scarcely. However, the inclusion of deeper layers contributes to the high number of free parameters ($f = 144$), although their influence on the spectra is rather small and can thus not be compared to a free parameter of a surface atom. Therefore, this model can still be assumed to be supported well by the amount of experimental data. Overall, the LEED-optimized model agrees within the uncertainties with the

#		x [Å]	y [Å]	z [Å]
1	Au	0.00 ± 0.00	5.91 ± 0.24	12.332 ± 0.19
3	Au	1.50 ± 0.21	10.11 ± 0.27	12.392 ± 0.24
5	Au	2.18 ± 0.27	12.99 ± 0.24	12.312 ± 0.16
6	Au	3.84 ± 0.00	6.01 ± 0.26	12.318 ± 0.19
7	Au	3.84 ± 0.00	8.77 ± 0.20	12.518 ± 0.14
8	hc	0.04 ± 0.28	-1.40 ± 0.21	11.657 ± 0.05
10	hc	-1.81 ± 0.55	0.02 ± 0.25	11.668 ± 0.07
11	hc	2.12 ± 0.51	0.04 ± 0.27	11.710 ± 0.07
12	hc	-2.01 ± 0.51	2.28 ± 0.25	11.741 ± 0.07
13	hc	1.97 ± 0.53	2.30 ± 0.25	11.741 ± 0.07
14	hc	0.00 ± 0.00	3.68 ± 0.28	11.743 ± 0.06
15	hc	3.84 ± 0.00	3.66 ± 0.26	11.730 ± 0.06
17	nw	1.65 ± 0.25	7.52 ± 0.22	11.913 ± 0.08
18	nw	0.00 ± 0.00	11.96 ± 0.23	11.838 ± 0.05
19	nw	3.84 ± 0.00	11.10 ± 0.25	11.936 ± 0.04

Table 6.1.: Atomic coordinates of the best fit structure. The coordinate system as well as the atom numbers are given in Figure 6.5. Next to the atom numbers, an indication to which group this atom can be counted, is given (Au = gold atom, hc = honeycomb motif, nw = silicon atom within the nanowire). $z = 0$ equals to the top of the fourth silicon bilayer beneath the surface. Atoms restricted by symmetry (2, 4, 9, 16) are omitted. Uncertainties of atoms bound on a mirror plane are denoted with ± 0.00 Å.

KK model derived by DFT [49]. A visual comparison of both models as well as detailed atomic displacements can be found in Figure B.1 and Table B.2 in the appendix.

6.2.3. Detailed analysis

Due to the reconstruction on the surface, displacements are expected to occur also in the deeper silicon layers. To ensure that enough layers for the optimization were included, different numbers of layers were used. Figure 6.6 displays the dependence of the Pendry R factor on the number of silicon layers beneath the surface used within the optimization. Using only one reconstructed silicon bilayer beneath the surface yields an R_{P} of 0.390, while using two bilayers already results in $R_{\mathrm{P}} = 0.136$. Three bilayers (as used in the best fit) yield a R_{P} of 0.117. Displacements of the fourth bilayer improved the best fit only to $R_{\mathrm{P}} = 0.115$, which can be regarded as insignificant, since the improvement is smaller than the variance of R_{P} for the best fit using three bilayers. Due to the already very small displacements from bulk positions in this depth (cf. Figure 6.6), the influence of a reconstruction of even deeper layers was not examined.

A closer look at Table 6.1 exhibits dependencies in the magnitude of the uncertainty corresponding to the position of the atom within the unit cell. While the uncertainties of the y-coordinates ($[11\bar{2}]$-direction) are uniform, the uncertainties of the x-coordinates ($[1\bar{1}0]$-direction) of the silicon atoms in the middle of the honeycomb motif (atom numbers 10, 11, 12, and 13) are distinctly greater than the uncertainties of other silicon atoms or the gold atoms. Figure 6.7 displays the dependence of

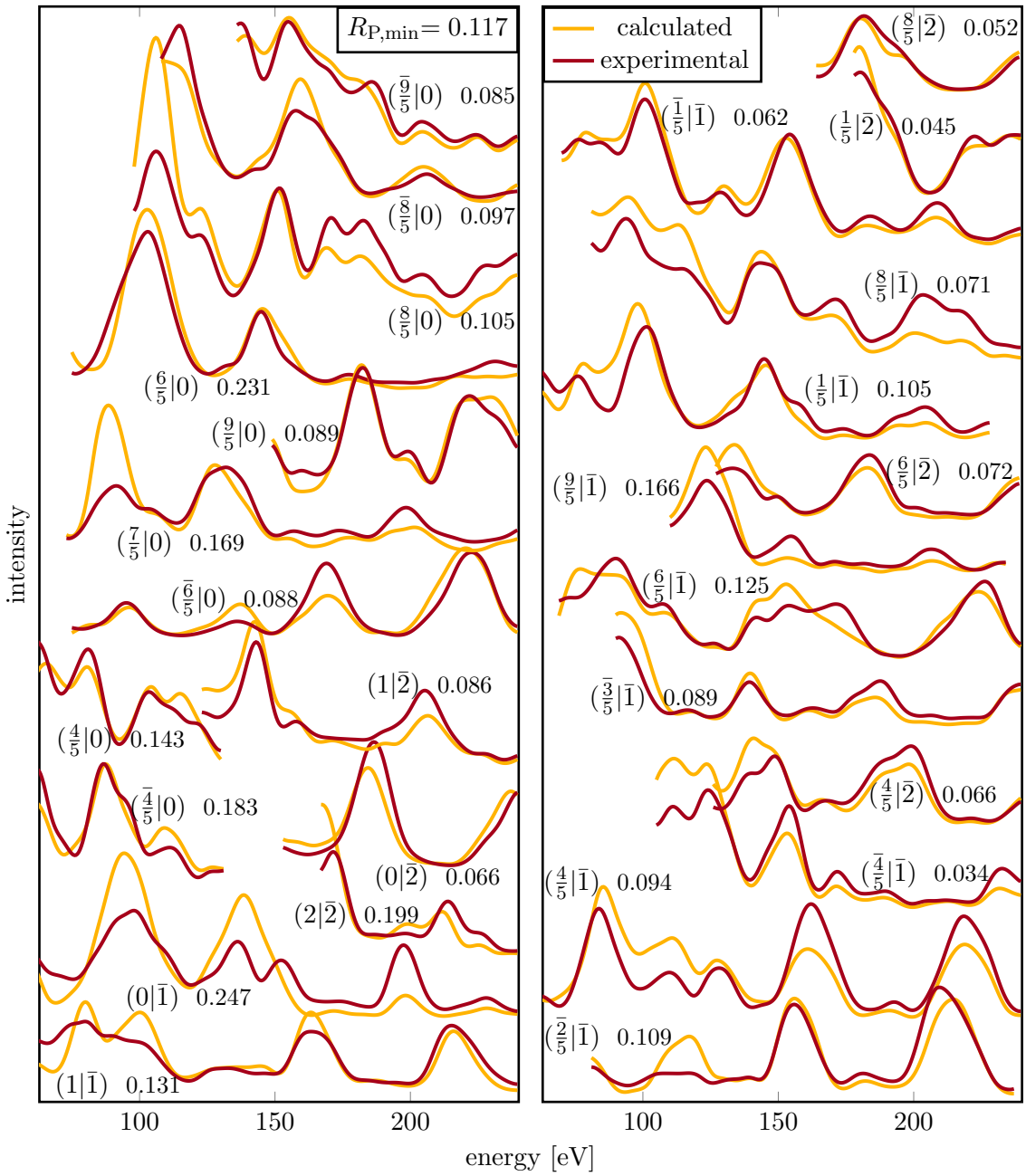

Figure 6.4.: Calculated IV spectra (yellow) of the best fit model in comparison with the experimental spectra (red). The different beams are shifted and stretched along the ordinate for better visibility. For each pair the index of the respective beam is given as well as the Pendry R factor. The overall Pendry R factor is 0.117.

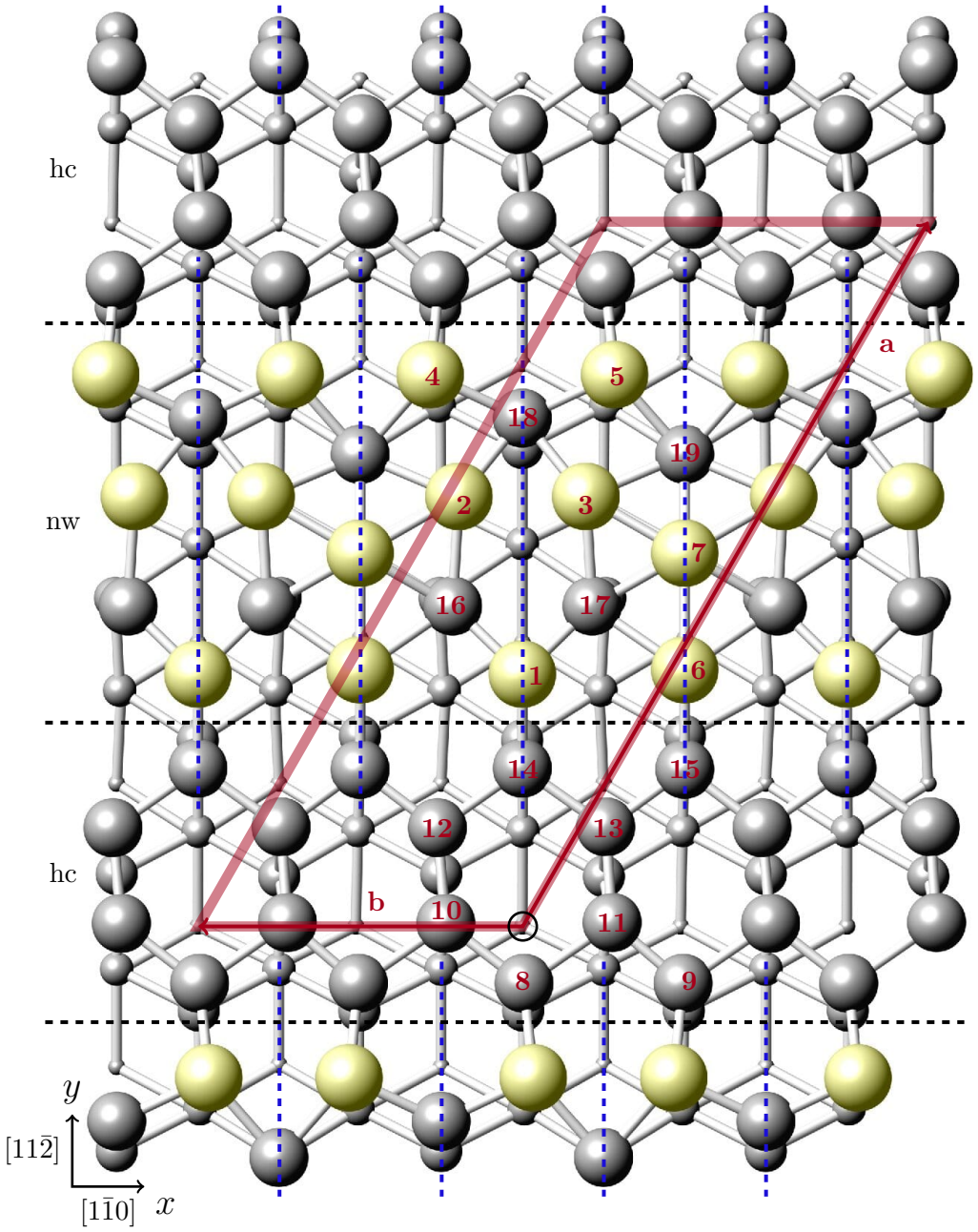

Figure 6.5.: Structure model of the reconstructed Si(111)-(5×2)-Au surface. The positions optimized by LEED coincide well with the established KK model [5]. The gold atoms are depicted with yellow spheres while the silicon atoms are represented by gray spheres. The diameter decreases with increasing distance to the surface for illustration purposes. Bonds toward gold atoms are drawn whenever atomic distances are in the range of the atomic distance in the silicon bulk and do not convey chemical meaning. The unit cell is marked by a red rhomboid, while atoms are denoted with red numbers. The origin of the coordinate system is marked by a black circle. Coordinates can be found in Table 6.1. The numbering of atoms is not oriented on the unit cell but on the axes of reflection (blue dashed lines) of the *pm* symmetry within nanowires (nw) that shifts at the honeycomb motif (hc).

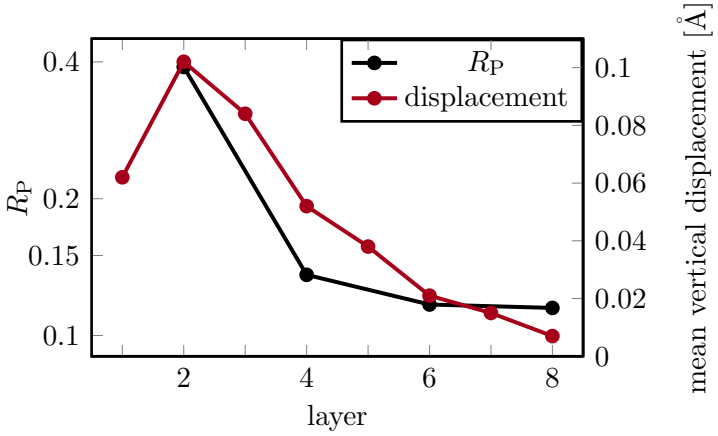

Figure 6.6.: R_P as a function of the number of optimized layers and averaged vertical displacement per layer for the LEED optimized model including four bilayers. Layer 1 corresponds to the upper layer of the first bilayer below the surface.

R_P on the displacement of single atoms. It can be seen that a displacement of the silicon atom in the honeycomb motif in $[1\bar{1}0]$-direction (δx) affects R_P only slightly, which causes a high uncertainty. Since the best fit model incorporates only one possible alignment of adjacent unit cells in y ($[1\bar{1}0]$)-direction, while in the experiment both possibilities are expected to occur (cf. Figure 6.8), discrepancies between calculation and experiment are anticipated. Therefore, these uncertainties hint at slightly different positions within the honeycomb motif for the respective alignments of the nanowires. An approach using both possible alignments and superimpose the respecting beams incoherently for the calculations would be correct, but increases the computational effort significantly. Therefore, the exact positions of atoms 10, 11, 12, and 13 within the here-presented model are to be treated with caution.

On the other hand, their vertical positions have comparable uncertainties to the other silicon atoms, which makes their vertical position much more reliable than their lateral position. However, all the gold atoms have a considerable increased vertical uncertainty compared to the silicon atoms in the surface layer. Their optimized radial root mean square displacements are also with 0.157 Å greater, than the radial root mean square displacements for either the silicon atoms within the honeycomb motif, or the silicon atoms embedded within the gold atoms, with 0.122 Å and 0.124 Å, respectively. An explanation for this behavior could be a less rigid bonding compared to the silicon atoms.

Surprisingly, the vertical and lateral uncertainties of the gold atoms are comparable. In Figure 6.7, it can be seen that a lateral displacement affects R_P comparably to a vertical displacement. Typically, a difference is expected due to the heightened sensitivity of the backscattered electrons to vertical positioning, as can be seen for the silicon atoms in Figure 6.7. This behavior could hint at not well-defined positions for the gold atoms, causing this insensitivity. A reason for this vertical uncertainty could be the interaction with randomly distributed silicon adatoms, thus having only marginal influence on the diffraction pattern.

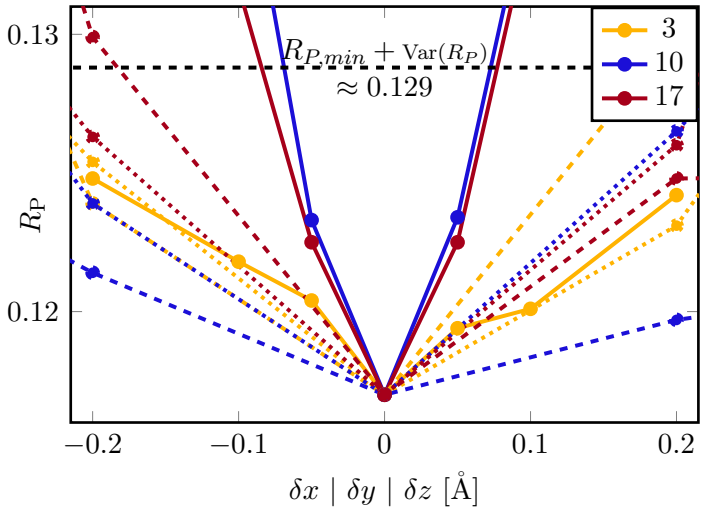

Figure 6.7.: Dependence of the Pendry R factor (R_P) from the displacement of a single atom relative to its best fit position (δx dashed, δy dotted, δz solid) while holding all other positions constant. The atoms number 3, 10, and 17 represent a gold atom (yellow), a silicon atom from the honeycomb motif (blue), and a silicon atom from the nanowire (red), respectively.

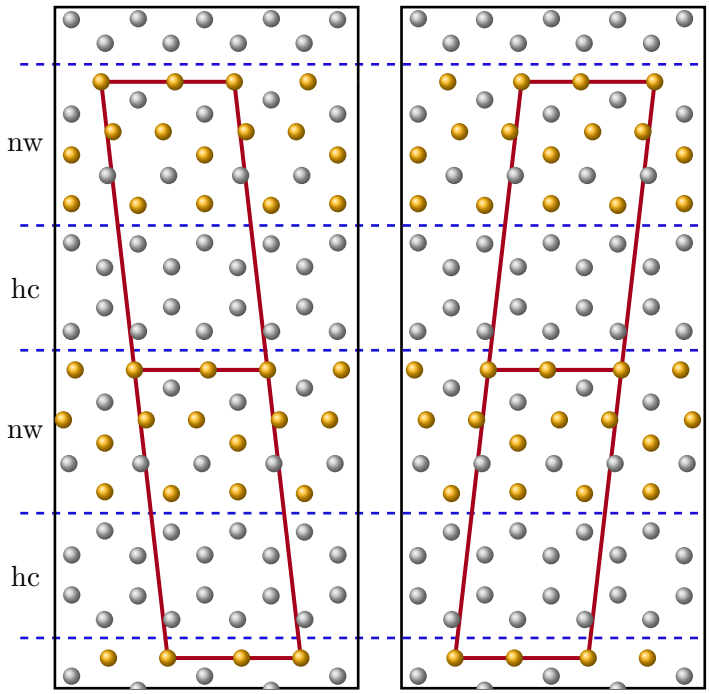

Figure 6.8.: Schematic sketch of two possible alignments of adjacent nanowires (nw) on the Si(111)-(5×2)-Au surface, separated by the silicon honeycomb motif (hc). Unit cells are denoted in red to highlight the different lateral periodicity. Notably, the two alignments are mirror-images of each other, so they are expected to be equally thermodynamically stable. When both alignments of adjacent nanowires occur statistically, streaks are expected in the diffraction pattern instead of sharp (×2) reflexes.

model	R_P	Var(R_P)
KK (*DFT*)	0.220	0.023
KK* (*LEED optimized*)	0.136	0.014
EBH (*DFT*)	0.399	0.042
EBH* (*LEED optimized*)	0.166	0.017
KK* (*missing Au*)	0.168	0.017
KK*(*Si substitution*)	0.147	0.015

Table 6.2.: R_P values for the different examined models and their variance. The models with a missing gold atom and a silicon atom instead of the gold atom are based on the KK model optimized by LEED. Further information of the models can be found in the text.

6.3. Alternative Models

Although the KK model is favored by DFT calculations and diffraction data from SXRD, the EBH model could not be ruled out confidently, due to its similarity to the KK model. To examine the differences between the models in a LEED analysis, also the EBH model was used to calculate LEED spectra and compare the results with the experimental spectra.

To speed up calculations in the optimization process, only two silicon bilayers were used. Additional to the EBH model obtained by DFT calculation, the EBH model was geometrically optimized to fit the LEED data. In the following, the models derived by DFT will be called KK and EBH, respectively. The LEED optimized versions will be denoted by an asterisk (KK* and EBH*). The Pendry R factors for the KK, EBH, KK*, and EBH* models can be found in Table 6.2. The KK* has the lowest R_P with 0.136. The comparison of the both models obtained by DFT is clearly in favor of the KK model with $R_P = 0.22$, compared to the EBH model yielding 0.399. This discrepancy means that the EBH can be ruled out with the LEED data. However, the EBH* model results in $R_P = 0.166$, which can be interpreted as a fine fit. To analyze the significance of this result, displacements of the surface atoms, caused by the optimization process, are further evaluated. As explained above, the position of the silicon atoms within the honeycomb motif are rather ambiguous, due to the statistical alignment of adjacent unit cells. In the following, only the gold atoms and the silicon atoms 16, 17, 18, and 19 within the nanowires are considered. To have a measure for the deviation of two models, the absolute displacement of corresponding atoms can be averaged over these atoms. The comparison of the EBH with the KK model (omitting atom 7 for the KK model) yields an average displacement per atom of 0.165 Å, illustrating the similarity of the two models. Nonetheless, the R_P between the KK and EBH model is with 0.285 quite high, making a clear distinction of the models with LEED possible. Comparing the KK model with the KK*, an average displacement of 0.096 Å per atom results, which lies within the average of the uncertainties given in Table 6.1 for these atoms. A comparison between the EBH and EBH* model yields an average displacement of 0.245 Å per atom, which is already a very substantial deviation. Therefore, it is doubtful, whether this optimized model can still be termed *EBH* model. Indeed, comparing the EBH* with the KK model yields an averaged displacement of 0.122 Å per atom, proving that the EBH* model is closer to the corresponding coordinates of

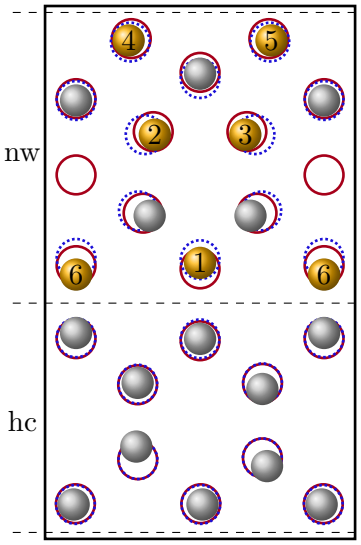

Figure 6.9.: Schematic arrangement of the surface atoms (gray and yellow for silicon and gold, respectively) for the EBH* model. The atom numbers are in analogy to Figure 6.5. Atomic positions derived by DFT are denoted by circles for the KK model (red) and the EBH model (blue, dotted). Differences between the EBH and KK models can mainly be found around the missing gold atom (empty red circle) within the nanowire (nw), while the honeycomb structure (hc) is virtually identical. The deviation of the positions within the honeycomb motif in the EBH* model is expected to originate in the statistical shift of adjacent unit cells (cf. Figure 6.8) that was not included in the LEED analysis.

the KK model than the EBH model. Figure 6.9 displays the schematic arrangement of the surface layer for the KK, EBH and EBH* model. It can be seen nicely for the EBH* model, how the surface atoms are displaced from the positions of the EBH model toward the positions of the KK model.

To further investigate the influence of the additional gold atom 7 (cf. Figure 6.5) in the KK* model, this atom was omitted, respectively substituted by a silicon atom. The Pendry R factor for the KK* model with the missing gold atom is 0.168, supporting the view that the EBH* model is rather a KK model without the additional gold atom, due to their similar R_P values ($R_{P(EBH^*)} = 0.166$). Indeed, the comparison of the IV curves of the EBH* model and the KK* model without the additional gold atom yields $R_P = 0.068$, while the difference between the KK* model and the KK* model missing the gold atom is greater with $R_P = 0.098$. Furthermore, substituting the gold atom 7 in the KK* model with a silicon atom yields $R_P = 0.147$ in comparison with the experimental spectra, thus being comparable to the KK* model. While this gives no argument for the stability of such structure, it shows that a scatterer is strongly needed in this position to reproduce the experimental spectra well.

Since only one preparation of this reconstruction was investigated in-depth, lower coverages could in principle allow the reconstruction as per EBH model, albeit only a very small window in the coverage for an exclusive (5×2) reconstruction was found within this thesis. Because of the different coverages of the EBH and KK model, it is therefore not convincing that the EBH model could be found at lower coverages.

6.4. Conclusion

A structural LEED analysis on the Si(111)-(5 × 2)-Au surface reconstruction was conducted, yielding a slightly optimized version of the established KK model [5]

with a conclusive agreement between experiment and dynamical diffraction theory. Furthermore, the EBH model, which is also able to explain X-ray diffraction data satisfactorily, can not explain the electron diffraction data and can therefore be ruled out. Additionally, a structure optimization by LEED of the EBH model leads toward a geometry which has more resemblance with the KK model. Moreover, it was shown that the presence of a scatterer at the location of the additional gold atom is necessary to describe the experimental LEED data satisfactorily. However, the positions obtained for the geometry of the honeycomb motif of silicon atoms are ambiguous, which is expected to originate in the incoherent superposition of diffracted beams from the different alignments of adjacent nanowires.

7. An Alternative Approach to Calculate LEED Intensities

With the advent of structural analyses by LEED, multiple programs were developed describing diffraction with varying success [20–25]. Differences were found mainly in the effects included, approximations that were made, and how propagation was described (spherical waves, plane waves, Bloch waves, or combinations of those), leading to specialized programs, which were not universally applicable to every surface [17]. The approach to divide the surface in layers, calculate multiple scattering within the layers, and then stack those layers (cf. section 2.3.8) achieved most success and has been adopted more recently to improve user friendliness or speed up the search process of optimized geometries [16, 62].

However, while this approach is efficient for smaller unit cells and well-separated layers, it also limits the possible surfaces to be investigated. This is due to the scaling of computational time according to $L^3N^3g^2$, with the number of spherical waves used $L = (l_{\max} + 1)^2$, the number of scatterers per unit cell N and the number of beams g [17], making calculations for very large unit cells (increasing N and g) or vicinal surfaces too slow to be feasible. Treatment of large unit cells can somewhat be improved by using the *Reverse-Scattering Perturbation* method, achieving computational time proportional to $L^2N^2g^2$, and the Tensor approximation to reduce the number of full dynamical calculations necessary to optimize a given structure. However, especially when analyzing vicinal surfaces, this method is still very time-consuming, since the layers are packed too close together to perform efficient calculations. This unfavorable scaling of computational time originates in the matrix inversion necessary for the self consistent formalism and the high number of diffracted beams in plane wave representation for large unit cells.

Therefore, in order to extinguish the drawbacks for large reconstructions and vicinal surfaces, a different approach to calculate multiple scattering is presented in this chapter. A similar approach had already been considered at the very beginning of structural analysis by LEED [24]. However, due to computational limits at that time, only a perturbation scheme could be used. In the last forty years, those limits have changed drastically, making a reconsideration of this attempt worthwhile.

In this alternative approach, paths of the electron are specifically focused instead of diffraction of surface layers. The foundations to describe the atomic scattering and the propagation of spherical waves within the crystal are the same, so it is expected to achieve virtually identical spectra. Since different approximations are made, small deviations can emerge, but the spectra should converge to the same results.

7.1. Concepts for a Path Approach

To improve the scaling with computational time for vicinal surfaces, it can help to avoid the explicit use of layers. This leads directly to the elimination of plane waves used for the description of propagation between layers. Plane waves are only used as incident waves and as final diffracted waves that reach the screen. Between single scattering events, only the spherical wave representation is used. Furthermore, the self-consistency is not included to avoid computationally costly matrix inversions. This can be done by interpreting the scattering as an summation of *all* possible paths that the electron can take within the surface due to multiple scattering.

Path Summations

The foundation of this approach is the *path integral formulation* of quantum mechanics. It allows the calculation of the probability for a given event (an electron from the source gets scattered in such a way that it hits the detector afterward) by a summation over all possible paths that the electron could have taken [63]. The observed probability P for a given outcome X is therefore

$$P(X) = |\Psi_{(X)}|^2 \qquad \text{with} \tag{7.1}$$

$$\Psi_{(X)} = \sum_n \Phi_{n(X)} \tag{7.2}$$

as the summation over all probability amplitudes that lead to the outcome X, denoted by $\Phi_{(X)}$.

In a LEED experiment, Φ is the wave function of a LEED electron taking one possible path. In the experiment, the intensity of a reflex is proportional to the number of electrons diffracted into this direction. Thus, relative intensities on the LEED screen can be calculated using the summation from equation 7.2, as the probability defines the distribution of the electrons on the screen. Since the size and shape of the unit cell is given as input to a calculation, directions in which reflexes can be found are known, so it is sufficient to calculate the probability only for the relevant reflexes and not for the whole screen.

Figure 7.1 illustrates two scattering paths that leave the crystal in the same direction. Thus, these wave functions need to be added to calculate the probability of an electron getting scattered into this direction by the surface. Since the number of atoms within the surface and the number of scattering events can be virtually infinite, this approach can only be calculated if certain approximations are made, which are described in the following in more detail.

Lattice periodicity

Crystalline surfaces exhibit a lateral periodicity, which can be used to simplify the summation of paths. Since the atoms within each unit cell are identical, the scattering of each unit cell must also be the same. Consequently, it is sufficient to consider

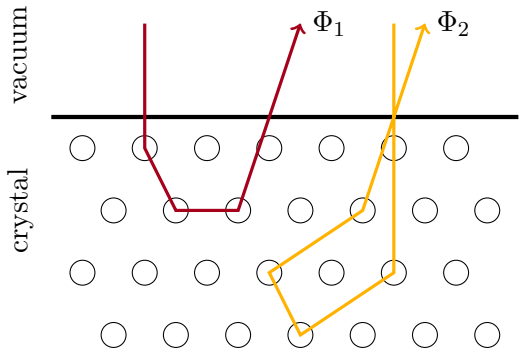

Figure 7.1.: Illustration of two different scattering paths, which have the same angle of incidence and leave the crystal in the same direction with the probability amplitudes Φ_1 and Φ_2 and thus contribute to the same reflex. The number of possible paths is, however, infinite due to the high number of atoms within the surface and the number of scatterings per path ranging from one to infinity.

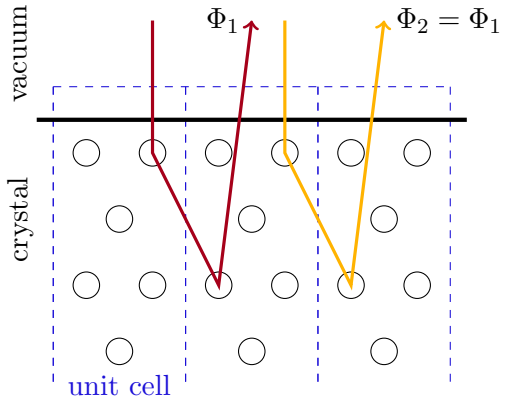

Figure 7.2.: Illustration of two different scattering paths that have the same probability amplitude $\Phi_1 = \Phi_2$ due to lateral translation symmetry. Independent of the number of scatterings or whether adjacent unit cells are involved, paths that are identical under the translations of the surface periodicity must have the same probability.

only those paths that experience their first scattering event in a single unit cell. Of course, the electrons can be scattered into adjacent unit cells; however, the whole scattering of the surface can be described by those paths that are initiated in one single unit cell due to the lateral translation symmetry. This is depicted in Figure 7.2. Notably, if the angle of incidence of the electrons is not perpendicular to the surface, a phase shift is expected to occur due to the different paths outside the surface of a wave front.

Limitation of the possible paths

The probability amplitude decreases exponentially with the distance traveled within the surface due to inelastic effects, which are modeled by the imaginary part of the inner potential. These inelastic effects can be interpreted as additional possible paths that do not contribute toward the intensity on the LEED screen (inelastically scattered electrons are repelled by the grids) and thus decreasing the probability (amplitude) of the LEED electron. However, this limits the crystal effectively in depth, so only a finite number of atoms within each surface unit cell must be considered. Additionally, it limits the number of scattering events per path, since infinite scattering events also require an infinite path traveled. The scattering can not compensate for this decrease due to flux conservation, i.e., the scattered amplitude can not be greater than the incident amplitude. Therefore, it is sufficient to evaluate

only paths up to a certain length and treat the multiple scattering only up to a finite order. Though, in advance of the calculation, it is not obvious which accuracy is sufficient.

Treatment of the bulk

The abandonment of the layer-centered approach comes at the cost of the loss of the highly efficient layer-doubling method. Therefore, it is necessary to include enough atoms in the surface unit cell, so no difference between the diffraction of the considered slab and a semi-infinite crystal results. In the following, it is, however, shown that the inclusion of that many atoms is within the capabilities of today's computers.

Incoming and departing waves

As the incoming and departing waves can be interpreted as plane waves due to their well-defined directions, it is most convenient to describe this first and last part of a path in terms of plane waves. This simplifies the treatment of phase shifts occurring at non-perpendicular angles to the surface for incident and departing waves. Nonetheless, it must be defined how the many spherical waves superimpose to gain correct probability amplitudes of the diffracted electrons. Since every atom within a unit cell forms a Bravais layer with the equivalent atoms in adjacent unit cells, the departing equivalent spherical waves of these atoms must interfere in such way that only in the directions of the various beams, defined by the shape and size of the unit cell, constructive interference occurs. The amplitudes of these plane waves of every Bravais layer can then be added straightforwardly.

7.2. Implementation

While the previous section discussed mostly the concepts for this new approach, here, the concrete implementation of these thoughts to perform the calculations are presented. First, a rough overview of the structure of the program is given. Afterward, some important details for the here-presented formalism that need to be considered are discussed. In the following, the program developed within this thesis calculating LEED intensities according to the path based approach is called *PathLEED*.

7.2.1. Structure of the program

The calculations can be separated into three different parts, which are discussed in the following: the evaluation of input parameters, the calculation of energy independent quantities, and finally an energy loop, yielding the final IV spectra.

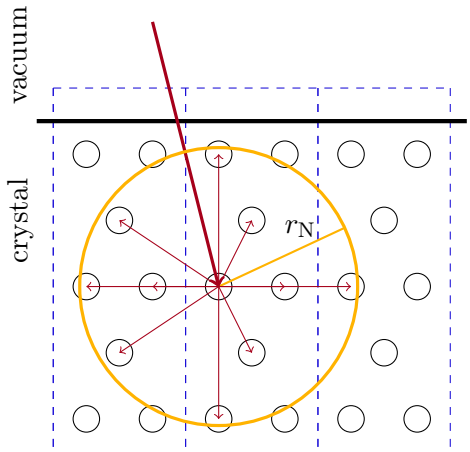

Figure 7.3.: Illustration of the radius r_N defining which atoms are counted as neighbors and therefore receive scattered electrons from the considered atom. Since the scattering cross sections are large and the atoms densely packed, the number of neighbors within r_N is expected to be treatable. Notably, atoms in greater distance than r_N can still be reached by multiple scattering.

Input

The inputs necessary to perform a calculation are, firstly, the atomic positions within the unit cell (x,y,z-coordinates) and the lattice vectors **a** and **b** defining the unit cell. Furthermore, the inner potential consists of two parameters for the imaginary and the real part. Obviously, also the energy range for which the spectra are desired must be set. Then, the angle of incident of the electrons as well as the desired value for the maximum angular quantum number l_{max} used for the spherical waves is needed. Since no self-consistent formalism is used, a criterion, determining the precision of the calculation, must be defined. This can be done by setting a maximum number for the scattering events per path or a (probability) cutoff value, so only paths with probability amplitudes higher than that value are considered. Finally, it must be defined to which neighbors an electron is scattered due to a single scattering event. In principle, it can be scattered to any other atom in the surface; however, due to the attenuation, great distances are very unlikely. Therefore, the radius r_N is introduced, which defines the maximum distance that is considered in between two scattering events; the electron can be scattered to any atom within this radius but not to the outside. Figure 7.3 depicts the definition of the radius r_N schematically. More accurately, this limitation should rather be an attenuation ratio, since r_N is expected to change with the electron energy, as the mean free path is also dependent from the energy. However, this has not been implemented yet. If the radius is large enough, results should be identical either way. Since the scattering cross sections are large and the atoms densely packed, an appropriate value for r_N is expected to lie within a few nanometers. Notably, atoms at greater distances than r_N can still be reached by multiple scattering.

Energy independent calculations

The spherical harmonics Y_l^m and Gaunt coefficients γ necessary for the calculation of the propagator are independent from the energy. Therefore, they can be calculated in advance of the actual calculation of the IV spectra. γ depends only on $l_{\max}$, while,

for the calculation of Y_l^m, the relative angles between the atoms are needed. For this purpose, all atomic distances and angles for atoms within r_N are also determined in advance of the energy loop.

Energy dependent calculations

The Hankel functions depend on the wave vector of the electron; therefore, the propagators must be recalculated for every step of the energy range of the spectra. Since the propagation within the surface is energy dependent, the multiple scattering formalism must also be performed for every energy step. Furthermore, the directions of the beams scattered to the detector are also dependent on the used electron energy.

7.2.2. Multiple scattering formalism

To calculate the scattering amplitudes by an explicit summation of the single paths, a scheme is needed to determine which of the infinite number of paths (due to possible infinite multiple scattering) must be considered. Since the number of possible paths diverges fast with the number of scatterings (N^s paths for an average of N neighbors and s scatterings per path), unlikely paths must be disregarded efficiently. The radius r_N already filters paths with a long distance between two scattering processes. However, this still yields far too many paths, which causes high computational times.

Path summation

In a first step, a set of the most probable paths, which are assumed to describe the scattering sufficiently is determined. This can be done recursively using a function that appends an additional scattering event to a path already in the set of relevant paths. Then, the new probability amplitude is evaluated, and if it is higher than a cutoff criterion ϵ, this new path gets added to the set. Therefore, every atom within the surface is represented by the triple of integers (n_i, n_x, n_y), which give the number of the atom within the unit cell n_i and the number the lateral lattice vectors $\mathbf{a}$ and $\mathbf{b}$ are added ($n_x and n_y$), respectively. In this way, any scattering path can be described by a succession of these triples. Notably, the propagator for the path from atom (i, n_x, n_y) to $(j, n_x + \delta_x, n_y + \delta_y)$ is independent from the actual values of n_x and n_y due to translational symmetry. Therefore, it is sufficient to calculate only propagations starting from one unit cell.

The set of relevant paths contains initially only the kinematic paths with a single scattering event. So it is iterated over all possible paths (with the maximum propagation distance per step r_N), but only those with a final amplitude greater than ϵ are kept. This method finished in a reasonable time when the criterion was chosen such that approximately the million most probable paths resulted.

However, the creation of the set of paths in this manner is rather time consuming. If a set is obtained that can describe the scattering at each energy, the evaluation of multiple scattering amplitudes is very fast, as only matrix multiplication is executed.

In practice, for a structure optimization, this fast evaluation would be a desirable property. The changes in positions and vibrational amplitudes are rather small in a structure optimization; therefore, it can be assumed that the set of paths is still valid. In that fashion many configurations could be evaluated very fast. However, the validity of this path approach could not be proven yet, since the spectra calculated by PathLEED do not match those of the established approach by layer stacking, which has shown its validity in comparison with experimental data, satisfactorily. The reason is still under investigation. Therefore, it is also still uncertain if the approximately one million most probable paths describe the scattering sufficiently.

Scattering order summation

To speed up the time it takes to calculate the theoretical IV spectra of the path approach from scratch, a summation scheme can be applied, resulting in a computational time linear to the highest scattering order considered. However, this comes at the downside of losing the information on how the final amplitudes are composed of the contribution of single paths. For the comparison with the layer stacking and to proof the validity of the path approach, this loss of information is however unproblematic. The ansatz of the summation scheme is based on the translational symmetry, such that the scattered amplitude for a given scattering order must be equal for all symmetry equivalent atoms (except a phase factor for a non-perpendicular incident wave). The scattered amplitude for atom i after one scattering event $\mathrm{F}_i^{(1)}$ (the superscript denotes the scattering order O_s) is given by

$$\mathrm{F}_i^{(1)} = {}_i\overline{T}\; A_i \;, \tag{7.3}$$

with the scattering matrix ${}_i\overline{T}$ of atom i and incoming amplitude A_i on atom i (cf. chapter 2.3.8). The atom i scatters the amplitude $\mathrm{F}_i^{(1)}$ now to all of its neighbors a within the scattering sphere of radius r_N. Conversely, all its neighbors scatter toward atom i. Therefore, the amplitude of the next scattering order of atom i is defined by

$$\mathrm{F}_i^{(2)} = \sum_a {}_i\overline{T}\; {}^i_a\overline{G}\; {}_a\overline{T} A_a = \sum_a {}_i\overline{T}\; {}^i_a\overline{G}\; \mathrm{F}_a^{(1)} \;, \tag{7.4}$$

with the propagator ${}^i_a\overline{G}$ from atom a to atom i (cf. chapter 2.3.6). This equation expresses that the second scattering order of atom i consists of all contributions from the first scattering order of neighboring scatterers, which propagate to atom i and get scattered there.

Equation (7.4) allows the calculation of the amplitudes of the next scattering order generally with the recurrence relation

$$\mathrm{F}_i^{(O_\mathrm{s})} = \sum_a {}_i\overline{T}\; {}^i_a\overline{G}\; \mathrm{F}_a^{(O_\mathrm{s}-1)} \;. \tag{7.5}$$

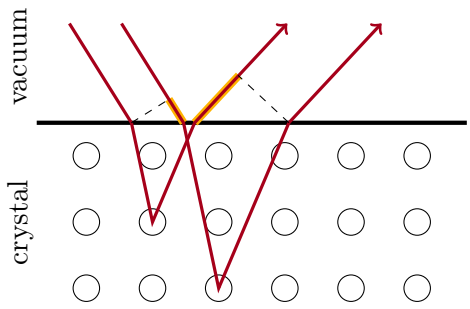

Figure 7.4.: Illustration of two paths including the refraction occurring at the surface due to the potential step. The path differences outside the surface are highlighted in yellow. The path inside the surface must also be taken into account, due to its effect on the phase and amplitude (caused by the attenuation of the imaginary part of the potential.

Combined with equation (7.3), this allows to calculate the amplitudes to an arbitrary high scattering order, with the same computational effort per scattering order, which indicates a linear scaling with the computational time. Expanding these sums shows that this is indeed equal to the set of all possible paths containing only propagations within r_N. Notably, this scheme is somewhat related to the modified propagator used to calculate propagation between layers in the layer-based approach [17]. However, this scheme yields the IV curves faster than the direct path summation while being equivalent. Therefore, this scheme is used in the calculations in the following section.

Notably, the spectra calculated by the direct method, using the approximately one million most probable paths, are virtually identical to the spectra calculated by the scattering order summation, which considers all possible paths within r_N up to a given scattering order. This suggests, that the direct method is indeed a viable approach to calculate LEED intensities.

Refraction

To correctly determine the amplitude and phase of the single paths, also the way from the vacuum to the first scattering, and the way from the last scattering back to the vacuum must be considered. Due to the well-defined direction of the incident and the diffracted waves, the description as plane waves is most convenient for these parts of the path. The potential step at the surface due to the real part of the inner potential causes a refraction of the electron wave, changing its energy and direction. The change in direction is a consequence of the conservation of momentum parallel to the surface, while increasing the norm of the momentum (and hence the norm of the wave vector). Figure 7.4 displays two paths including refraction at the surface. The path outside the surface affects the relative phase of different paths and must thus be considered. The path inside the surface, either before the first or after the last scattering event, causes also an attenuation due to the imaginary part of the potential. Those segments of the paths are described by plane waves.

The attenuated incident plane wave is expanded into spherical waves at the position of the first scattering event, to enable the application of the formalism described in section 2.3. The spherical waves, scattered by the last atom in the path, can be added since they are partial waves, to obtain the amplitude of the resulting plane

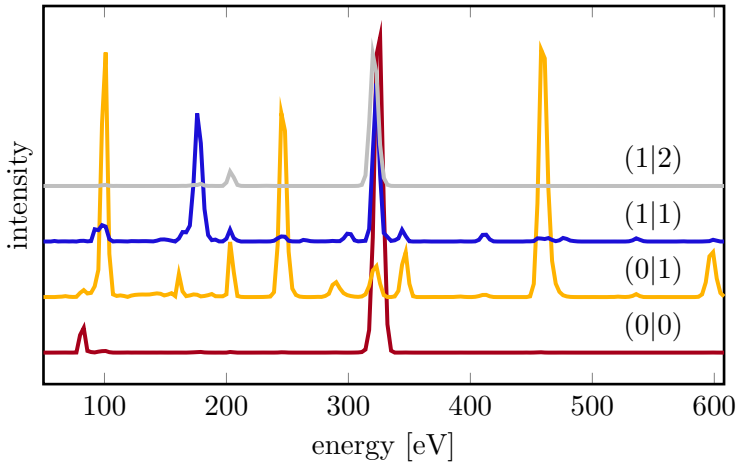

Figure 7.5.: Four exemplary IV spectra calculated by PathLEED with the parameters $r_N = 24\,\text{Å}$ and $O_s = 10$. All spectra diverge at certain energies. The most prominent peak can be found in all spectra at approximately 325 eV. Increasing the scattering order increases the intensity of the peaks further.

wave.

7.3. Comparison with CLEED

The CLEED package was used as a reference to check how PathLEED performs against the layer-based approach. To enable the comparison between the traditional layer approach and the here-presented approach focusing on next neighbors, the Ag(001) surface was chosen as a testing structure. This decision is based on the outstanding agreement that has been achieved between experiment and theory for this surface [38]. However, no relaxation of the top layers were included. Both programs used the same set of phase shifts, while limiting the number of spherical waves to $l_{max} = 4$, accelerating the calculation of spectra to enable fast comparisons upon variation of other parameters. Furthermore, thermal vibrational amplitudes were set to zero.

7.3.1. Comparison of IV spectra

Figure 7.5 displays four exemplary spectra obtained from PathLEED. The spectra are dominated by peaks that diverge when increasing the scattering order. Of course, this is highly problematic since the spectra should converge with an increase in the scattering order. Therefore, this hints at paths with amplitudes not being attenuated strong enough, while being scattered repeatedly.

While the exact origin of this flawed calculation is difficult to determine, a simple modification of the scattering matrix (and thus decreasing the scattered amplitudes) according to

$$\overline{T}' = \frac{1}{2}\,\overline{T} \tag{7.6}$$

already yields spectra that are comparable to spectra calculated by CLEED as shown in Figure 7.6. For r_N and O_s values of 18 Å and 7 were chosen, respectively. The

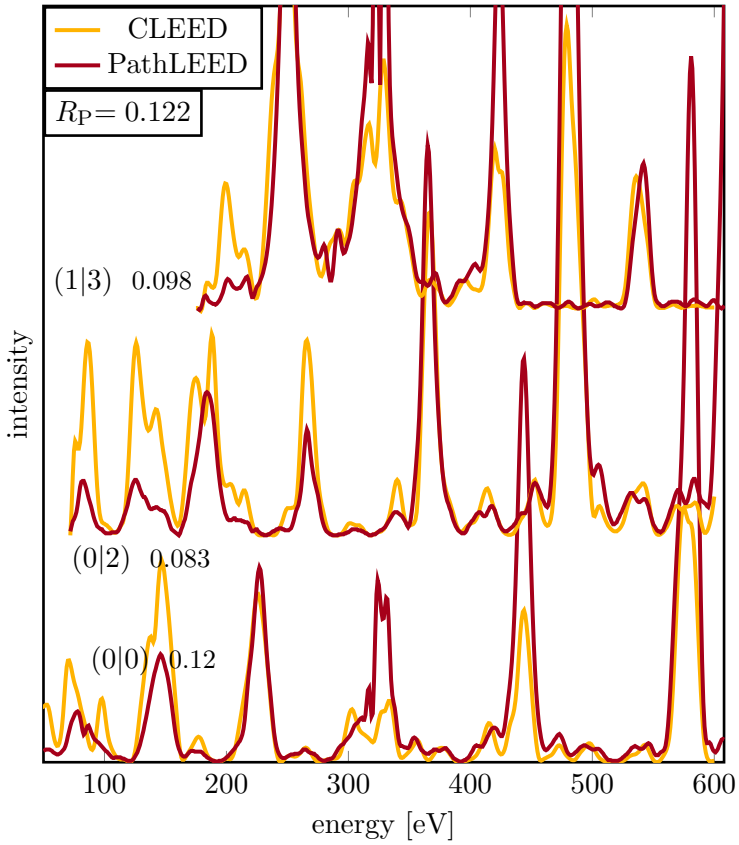

Figure 7.6.: Three exemplary IV spectra calculated by CLEED and PathLEED, respectively. Used parameters are $r_N = 18$ Å and $O_s = 7$. A good agreement is apparent, yielding an overall Pendry R factor of 0.122. The R_P values for the single spectra are denoted next to the spectra. However, some deviations are evident.

overall Pendry R factor (for smoothed spectra according to equation (2.5)) is 0.122, confirming the good match in peak positions. However, at distinct energies, the PathLEED spectra are still non-convergent for an increase in the scattering order O_s. Furthermore, at low energies the intensities of CLEED are substantially higher, while being lower at high energies compared to PathLEED.

To compare the spectra in more detail, the Y-functions as used in the definition of R_P are depicted in Figure 7.7. They exhibit a good agreement between the calculations regarding the position of the extrema in the spectra. The apparent deviations are mainly due to differences in relative intensities.

In conclusion, the positions of the peaks are calculated correctly, indicating that PathLEED can indeed simulate multiple scattering. However, strong deviations in predicted intensities can be seen between the programs. Furthermore, spectra calculated by PathLEED diverge at certain energies, when increasing the considered scattering orders. This could hint at a problem within the calculation of the propagators and/or scattering amplitudes. The intensity at energies below 100 eV is distinctly below that of the CLEED calculation. The rather strong backscattering at this energy (cf. Figure 2.17) should indeed lead to higher intensities in this energy regime. To investigate the exact reasons for the deviations from the established calculation, the dependence of the spectra from possible parameters is examined in the following.

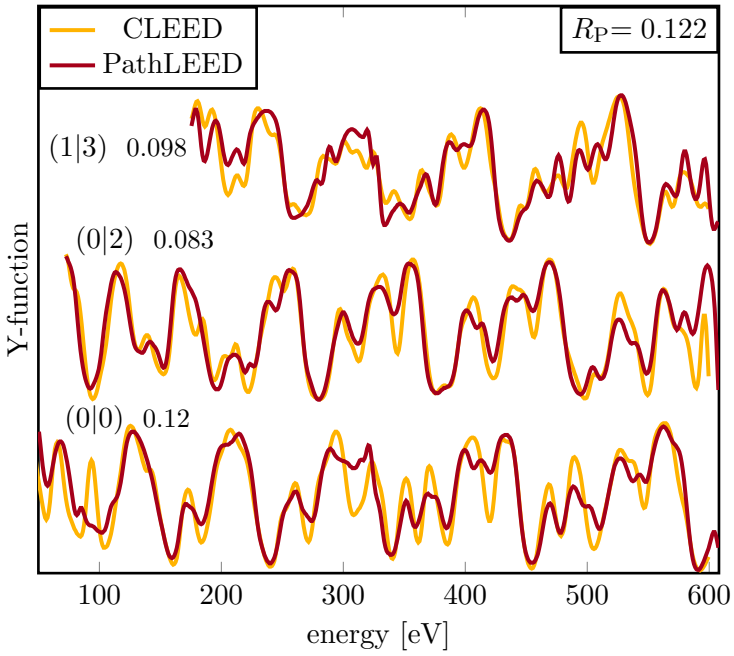

Figure 7.7.: The Y-functions of the spectra plotted in Figure 7.6. Due to the logarithmic derivative in the definition of the Y-functions, they allow a detailed comparison of peak position, while relative differences in peak intensity are not as prominent. Indeed, the kinematic as well as multiple scattering peak positions are reproduced satisfactorily, save minor exceptions. The deviations in the amplitude of the Y-functions are caused by the differences in relative intensities.

parameter	value ref.	value alt.	R_P
r_N	18 Å	24 Å	0.002
n_L	14	16	0.000
l_{max}	4	8	0.100
O_s	7	12	0.009

Table 7.1.: Resulting Pendry R factors R_P between spectra calculated by PathLEED with the reference (ref.) and alternated (alt.) value for the parameters r_N (radius of scattering), n_L (number of layers), l_{max} (maximum angular quantum number l considered) and O_s (scattering order). Only increasing l_{max} leads to significantly changed spectra.

7.3.2. Dependence on parameters

To analyze, whether the difference observed between CLEED and PathLEED originates in errors within the program or the choice of parameters, these parameters are varied to examine their influence on the spectra. Therefore, the above presented calculation was taken as reference and all parameters were increased individually, to check if the spectra were already converged. Thereby, only one parameter at a time was changed, leaving the others constant. To evaluate the differences, Pendry R factors were calculated. Results can be seen in Table 7.1.

For the calculation of the reference spectra, 14 layers were used, implying a thickness of the slab of approximately 26 Å. While an increase in the number of layers n_L or the radius for which propagation was assumed (r_N) did not change the spectra, increasing l_{max} had an apparent influence. This is not surprising as the initial value of $l_{max} = 4$ was rather small. However, the spectra are converged with $l_{max} = 8$, since a further increase does not exhibit further changes. Values of $l_{max} \geq 8$ also

caused the aforementioned divergences, while having discrepancies with the spectra calculated by CLEED comparable to the discrepancies seen in Figure 7.6. Also, a small increase in the scattering order O_s does not alter the spectra significantly. However, a closer look at the spectra exhibits small spikes in regions where divergences were observed before the modification of the scattering matrix. A further increase of O_s leads to strong peaks at those energies, while leaving the remaining parts unchanged.

Summarizing, this indicates that PathLEED can indeed be used to calculate dynamical diffraction of electrons, since the spectra converge fast enough for the chosen parameter of approximation to be manageable for today's computers. However, unknown problems within the program written within this thesis prevent a satisfactory agreement with established programs. Since the positions of the multiple scattering peaks can be predicted correctly, the basic aspects appear to be working. Additionally, spectra that are expected to be equivalent due to symmetry are indeed equal, indicating a correct implementation of the spatial components. Thus, the occurring divergences indicate a wrong quantitative calculation of the scattering and or propagation.

7.3.3. Computational effort

Despite the problems discussed above, the program is expected to work sufficiently to estimate the dependencies of computational time from the size of the unit cell. Therefore, the unit cell of the bulk-terminated Ag(001) surface is enlarged artificially by an alternating doubling of the lengths of the lattice vectors $\mathbf{a}$ and $\mathbf{b}$, thus doubling the number of atoms within each unit cell. The spectra are not changed since the surface remains unchanged (although the indices of the beams are modified), but the calculation gets increasingly demanding.

Figure 7.8 shows the relative time increase as a function of the number of primitive unit cells within the unit cell used for the computation x. The unit cells were enlarged as (2×1), (2×2) and (4×2) "reconstructions". Therefore, the number of primitive unit cells per artificially enlarged unit cell was 2, 4 and 8, respectively. The respective computing times were normalized to the computing time for the primitive unit cell (1×1). Notably, also, the unit cell for the bulk atoms was enlarged within CLEED. This would not be the case for a large reconstruction. However, in the case of a vicinal surface, also the bulk unit cell becomes large (in fact, due to the small layer spacings, the computing time would increase even more drastically, since the surface can not be divided into well-separated layers). Therefore, the yellow circle denotes the relative time increase, if only the two topmost layers are enlarged, yielding approximately a proportionality of x^2 to the computing time. However, in a real reconstruction one would need more than one enlarged layer, leading to a result in between these two approximations (yellow triangle for four layers).

While CLEED exhibits a proportionality between N^2 and N^3, the here-presented approach has only a computational time increase proportional to N. This is due to the fact that every atom in the surface has approximately the same number of con-

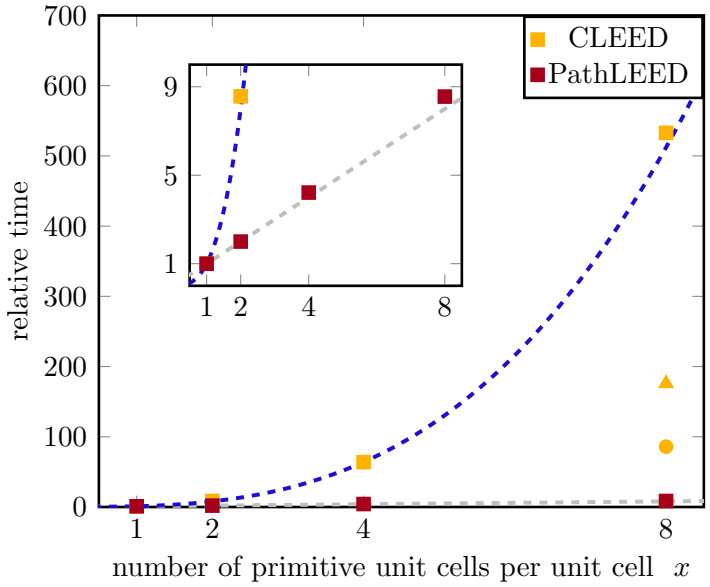

Figure 7.8.: Plot of the time a calculation with larger unit cell takes compared to the time for the primitive unit cell. The measured data are marked by squares. The dashed lines depict a proportionality to x (gray) and x^3 (blue), respectively. The yellow circle and triangle denote the time increment if only the two and four top layers were enlarged in a CLEED calculation, respectively.

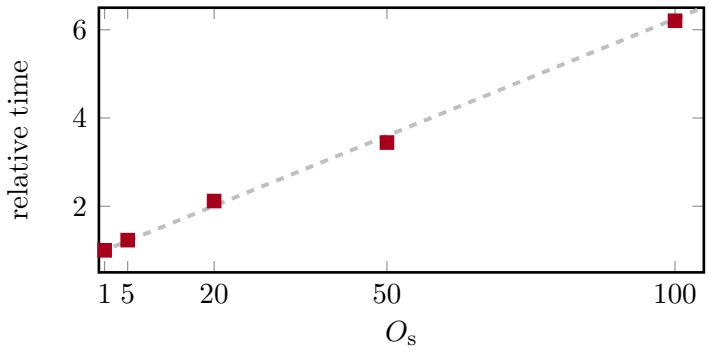

Figure 7.9.: Dependence of the calculation time from the scattering order. The time increase is normalized on the time for the calculation of a single scattering per path. The dashed line is a guide to the eye to illustrate the linear dependence.

sidered neighbors. Therefore, the amplitude calculation must be performed N-times, but does not get more complex for a larger surface. In the case of very large unit cells (larger than the typical distance traveled by a LEED electron), the traditional approach to calculate the scattering within each Bravais layer gets rather pointless, due to the large distance between scatterers in each (Bravais) layer. Furthermore, the stacking of layers by plane waves becomes expensive, since more different beams must be considered each time. However, in the case of small unit cells, layer stacking is very efficient and outperforms PathLEED significantly. For the (1×1) unit cell, CLEED is faster by a factor of approximately 8. While this is also partly due to the non-optimized state of the path-based program, no significant advantages for small unit cells are expected. Nonetheless, PathLEED in its unoptimized version supersedes CLEED already at a unit cell size four times bigger.

Figure 7.9 exhibits the aforementioned linear dependence of the calculation time from the included scattering order. Hence, within this approach the inclusion of high enough scattering orders is not computationally costly. However, it is still uncertain, whether the approach of direct path summations without the recurrence

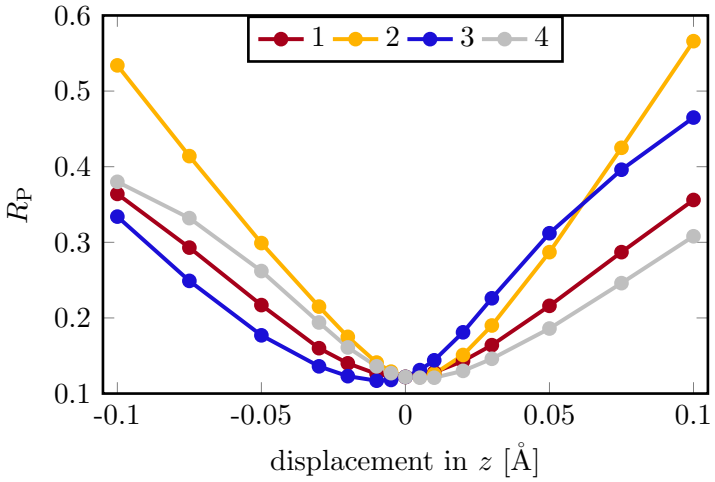

Figure 7.10.: Dependence of the Pendry R factor on the variation of the vertical position of the top four layers. R_P was determined for the spectra of the bulk-terminated Ag(001) surface calculated by CLEED and the spectra calculated with the here-presented program for a surface with a vertical displacement of a single layer.

relation yields adequate results within a reasonable time frame.

7.3.4. Variation of structural parameter

To further evaluate, whether the path-based approach is valid, the influence on varied geometrical parameters is examined. Therefore, a single layer is displaced vertically. The resulting spectra calculated with PathLEED are then compared to the spectra of CLEED for the bulk-terminated surface using the Pendry R factor. Figure 7.10 displays the results of this procedure for the top four layers and different displacements. All curves exhibit a similar shape with a single minimum in R_P around the bulk-terminated structure and a mostly positive curvature. For layer 3, the exact position of the minimum is at a displacement of -0.01 Å. This deviation is expected to originate in the discrepancies of the spectra mentioned above and thus to be interpreted as statistical fluctuation of R_P.

However, the shape of the curves implies that a geometrical optimization with the current state of the program is already possible. This further supports the assumption that qualitatively, the calculations are correct, but unknown errors in the program lead to wrong quantitative results for the scattered amplitudes. A comparison of the spectra for displaced layers by ± 0.1 Å, calculated by CLEED and PathLEED, yields R_P values around 0.16, indicating that the program also works qualitatively for displaced surfaces.

7.4. Hardware Considerations

With the advent of structural analysis by LEED in the seventies, programs had to be developed in such a way that calculations would converge in a reasonable time and limitations regarding memory had to be considered. The CRAY-1 supercomputer, first installed in 1976, had an 80 MHz processor and memory up to 8.4 MB. Today, multiprocessor units with a clock rate of over 3 GHz each and *random access*

memory (RAM) sizes beyond 16 GB can be found in consumer electronics. While the improvement of processors mainly speeds up the calculation (especially, if parallel computing is performed, which is easily done for LEED calculations due to the independence of the energy steps), the tremendous increase of accessible RAM may allow approaches that were impractical previously.

This is indeed the fact for the here-presented approach. At each energy step, at first, the scattering and propagation matrices are calculated for each atom and their distance to a neighbor, respectively. Using double-precision floating-point format leads to a size of 16 B for each (complex) element of the propagator matrix. In the case of the artificial enlarged Ag(001)-(4×2) surface calculated above the $N = 8{\cdot}14 = 112$ atoms per (4×2)-cell with an average number of neighbors of approximately $n_\mathrm{N} \approx 1100$ within r_N requires 123200 matrices with a size of $L^2 = (l_\mathrm{max}^2)^2$ each. For $l_\mathrm{max} = 9$, those matrices only for the propagators occupy a total of 19.712 GB, which would have been an absurd demand at the time of the initial development of LEED programs. The use of symmetries in the deeper layers can, however, reduce this number significantly, but nonetheless, this approach was plainly not possible in the seventies due to hardware constraints. Nowadays, the accessible hardware allows these calculations that could facilitate the analysis of large reconstructions and vicinal surfaces.

7.5. Prospects for the Path Approach

The here-presented program PathLEED in its current form is rather rudimentary and aims only to show the feasibility of this approach and hint at the possible benefits. In this section, potential improvements that are viable within the path-based approach are discussed.

Efficient calculations

The time for a full dynamical calculation could be reduced drastically by exploiting the symmetries of the crystal. Since PathLEED uses many layers, which have to be included into the multiple scattering formalism, a high number of propagators has to be calculated. However, due to the periodicity of the crystal, many distances (length and direction) occur repeatedly between different atoms and thus the propagators of those distances must be equal. This can be used to reduce the number of calculated propagators and therefore speed up the calculation as well as reduce the amount of necessary memory. Indeed, the calculation of propagators is currently the most time-consuming step. Additionally, those symmetries can also be used to accelerate the calculation of the spherical waves and Hankel functions, which are the components for the propagators. In its current form, the program uses only simple loops that make the programming code very clear at the cost of many unnecessary repetitions.

Furthermore, it could be worthwhile to calculate as much as possible before launching the loop over the energy. In the definition of the propagator (equation (2.51)),

the summation over m_r is independent of the electron energy and could thus be evaluated in advance, instead of recalculating it at every energy step.

These possible improvements were not applied yet, since they would complicate the search for errors, causing the discrepancies toward CLEED.

Parameter optimization

The approach based on the summation of single paths does not only promise improved handling of large unit cells and vicinal surfaces. It also enables new possibilities for efficient schemes for the optimization of parameters. For example, the addition of a single atom to an already calculated model can be treated easily. Since the amplitudes for all possible paths *not* containing the additional atom are already known, only those paths containing this very atom must be considered, which is less expensive. For LEED at large unit cells, this feature is valuable, since the influence of a single atom on the spectra is rather small (cf. chapter 6). This could allow the easy addition of atoms in various locations to an existing model and thus simplify the exploration of new structural models.

Furthermore, due to the information how distinct paths contribute toward the intensity of peaks in the spectra, it could be possible to develop new algorithms that exploit this connection for directed search algorithms. This would allow an acceleration in the time consuming optimization process.

Besides, comparable to the Tensor approximation, in the path-based approach, once a full dynamical calculation was performed, small deviations from this reference structure can be approximated, thus allowing a fast exploration of the parameter space. This can be done by the introduction of a shift in the phase and change in the modulus, depending on the directions of the electron and displacement. Subsequently, those variations in the amplitude must only be added to the already calculated amplitude for the corresponding path in the reference structure.

7.6. Conclusion

An alternative approach for LEED intensity calculations was proposed, which was, in the beginning of structural analyses by LEED, impossible due to the demands on the computer hardware. Thereby, many single paths are calculated within spherical wave representation and superimposed outside the surface. While being rather inefficient for small unit cells with well-separated layers, the presented linear dependence of computational time from the number of atoms per unit cell makes it a valuable approach for large unit cells. Furthermore, the explicit avoidance of layer stacking makes structural LEED analyses of vicinal surface conceivable. Additionally, a recurrence relation was proposed to allow the inclusion of higher scattering orders within this framework, while scaling only linearly with the computational effort. However, the resulting spectra do not agree well enough with the spectra of established programs. While the positions of multiple scattering peaks are pre-

dicted correctly, relative intensities are wrong. Due to the good convergence with the parameters used for approximations, this difference is believed to originate from unknown errors in the program code that could not be corrected yet.

Summarizing, the here-presented approach could show its value for large unit cells and vicinal surfaces. Nonetheless, the implemented calculations must be reviewed to find the source of the discrepancy to established calculations.

8. Summary & Outlook

In this thesis, structural LEED analyses for the clean Si(001) surface as well as the Si(111)-(5×2)-Au reconstructions were performed. Furthermore, an alternative approach was proposed to calculate the multiple scattering that could make the LEED analysis of very large reconstructions and vicinal surfaces feasible.

The structural analysis of the Si(001) surface was in good agreement with previous results [39, 46] and DFT calculations [49]. However, the limited means to distinguish between different alignments of similar adjacent unit cells was exhibited, making a structural LEED analysis suboptimal for the distinction between the (2×1) and $c(4 \times 2)$ reconstructions. Additionally, the validity of the use of elastic strain energy as proposed by Keating was shown to improve the starting position for a structural analysis of covalent crystalline surface by LEED.

In the second part, the viability of the Kwon-Kang (KK) model for the Si(111)-(5×2)-Au reconstruction was confirmed. Furthermore, the model proposed by Erwin, Barke and Himpsel (EBH) could be ruled out due to the discrepancy with the experimental data. An optimization of the EBH model to fit the LEED data resulted in a geometry with more resemblance to the KK model. Thereby, the higher structural sensitivity of LEED over XRD within a structural analysis could be exhibited impressively.

The last part covered the possible enhancement of the traditional approach to calculate LEED intensities for material systems with large unit cells or vicinal surfaces. While it was shown that the computational time within this approach scaled only linearly with the number of atoms per unit cell, discrepancies of unknown source to spectra calculated by the established approach remained. However, the convergence for the parameters used as approximation was satisfactorily, why it is plausible to assume the flaws in the program, not the approach itself.

Summarizing, the strengths of LEED in the structural analysis of silicon surfaces was shown. To boost the analysis of very large reconstructions and or especially vicinal surfaces, further development in the calculation of LEED intensity is promising, utilizing the increase of computational power that was developed in the past decades.

Bibliography

[1] R. E. Peierls, **Quantum Theory of Solids**. Oxford University Press, 1955.

[2] F. D. M. Haldane, **Luttinger liquid theory of one-dimensional quantum fluids. i. properties of the luttinger model and their extension to the general 1d interacting spinless fermi gas**, *Journal of Physics C: Solid State Physics*, vol. 14, no. 19, pp. 2585–2609, 1981. DOI: 10.1088/0022-3719/14/19/010.

[3] H. E. Bishop and J. C. Rivière, **Segregation of gold to the silicon (111) surface observed by auger emission spectroscopy and by LEED**, *Journal of Physics D: Applied Physics*, vol. 2, no. 12, pp. 1635–1642, 1969. DOI: 10.1088/0022-3727/2/12/302.

[4] S. C. Erwin, I. Barke, and F. J. Himpsel, **Structure and energetics of si(111)-(5 × 2)-au**, *Phys. Rev. B*, vol. 80, p. 155 409, 15 2009. DOI: 10.1103/PhysRevB.80.155409.

[5] S. G. Kwon and M. H. Kang, **Identification of the au coverage and structure of the au/si(111)-(5 × 2) surface**, *Phys. Rev. Lett.*, vol. 113, p. 086 101, 8 2014. DOI: 10.1103/PhysRevLett.113.086101.

[6] M. Jałochowski, M. Stróżak, and R. Zdyb, **Gold-induced ordering on vicinal si(111)**, *Surface Science*, vol. 375, no. 2, pp. 203–209, 1997, ISSN: 0039-6028. DOI: https://doi.org/10.1016/S0039-6028(97)80009-X.

[7] P. Segovia, D. Purdie, M. Hengsberger, and Y. Baer, **Observation of spin and charge collective modes in one-dimensional metallic chains**, *Nature*, vol. 402, no. 6761, pp. 504–507, 1999. DOI: 10.1038/990052.

[8] J. N. Crain *et al.*, **Fractional band filling in an atomic chain structure**, *Phys. Rev. Lett.*, vol. 90, p. 176 805, 17 2003. DOI: 10.1103/PhysRevLett.90.176805.

[9] C. Davisson and L. H. Germer, **The scattering of electrons by a single crystal of nickel**, *Nature*, vol. 119, no. 2998, pp. 558–560, 1927. DOI: 10.1038/119558a0.

[10] K. Heinz, **Low-energy electron diffraction**, in *Surface and Interface Science*, K. Wandelt, Ed., Wiley VCH, 2012, ch. 3.2.1, pp. 93–149.

[11] J. B. Pendry, **Ion core scattering and low energy electron diffraction. i**, *Journal of Physics C: Solid State Physics*, vol. 4, no. 16, pp. 2501–2513, 1971. DOI: 10.1088/0022-3719/4/16/015.

[12] M. P. Seah and W. A. Dench, **Quantitative electron spectroscopy of surfaces: A standard data base for electron inelastic mean free paths in solids**, *Surface and Interface Analysis*, vol. 1, no. 1, pp. 2–11, 1979. DOI: https://doi.org/10.1002/sia.740010103.

[13] J. Bahlmann, **Iv-leed untersuchungen an ag(001): Experimentelle einflüsse und datenanalyse**, Masterarbeit, Universität Osnabrück, 2017.

[14] J. B. Pendry, **Reliability factors for leed calculations**, *J. Phys. C: Solid St. Phys.*, vol. 13, pp. 937–44, 1980.

[15] T. Fauster, L. Hammer, K. Heinz, and A. Schneider, **Oberflächenphysik: Grundlagen und Methoden**. Oldenbourg, 2013, ISBN: 9783486721355.

[16] G. Held, private communication.

[17] M. V. Hove, W. Weinberg, and C.-M. Chan, **Low-Energy Electron Diffraction**. Springer, 1986, ISBN: 978-3-642-82723-5.

[18] M. V. Hove and S. Tong, **Surface Crystallography by LEED**. Springer, 1979, ISBN: 978-3-642-67197-5. DOI: 10.1007/978-3-642-67195-1.

[19] P. Waterman, **Matrix formulation of electromagnetic scattering**, *Proceedings of the IEEE*, vol. 53, no. 8, pp. 805–812, 1965. DOI: 10.1109/PROC.1965.4058.

[20] D. W. Jepsen, P. M. Marcus, and F. Jona, **Low-energy-electron-diffraction spectra from [001] surfaces of face-centered cubic metals: Theory and experiment**, *Phys. Rev. B*, vol. 5, pp. 3933–3952, 10 1972. DOI: 10.1103/PhysRevB.5.3933.

[21] D. W. Jepsen, **New transfer-matrix method for low-energy-electron diffraction and other surface electronic-structure problems**, *Phys. Rev. B*, vol. 22, pp. 5701–5715, 12 1980. DOI: 10.1103/PhysRevB.22.5701.

[22] H. Davis, J. Noonan, and L. Jenkins, **Determination of a cu(110) surface contraction by leed intensity analysis**, *Surface Science*, vol. 83, no. 2, pp. 559–571, 1979, ISSN: 0039-6028. DOI: https://doi.org/10.1016/0039-6028(79)90063-3.

[23] R. Feder and J. Kirschner, **Spin-polarized low-energy electron diffraction: Theory, experiment and analysis of results from w(001)(1 × 1)**, *Surface Science*, vol. 103, no. 1, pp. 75–102, 1981, ISSN: 0039-6028. DOI: https://doi.org/10.1016/0039-6028(81)90100-X.

[24] R. S. Zimmer and B. W. Holland, **A new iterative perturbation scheme for LEED calculations**, *Journal of Physics C: Solid State Physics*, vol. 8, no. 15, pp. 2395–2400, 1975. DOI: 10.1088/0022-3719/8/15/013.

[25] N Masud, C. G. Kinniburgh, and J. B. Pendry, **MEED intensity calculations for aluminium (110) and (100) surfaces using the chain method**, *Journal of Physics C: Solid State Physics*, vol. 10, no. 1, pp. 1–10, 1977. DOI: 10.1088/0022-3719/10/1/005.

[26] P. J. Rous *et al.*, **Tensor leed: A technique for high-speed surface-structure determination**, *Phys. Rev. Lett.*, vol. 57, pp. 2951–2954, 23 1986. DOI: 10.1103/PhysRevLett.57.2951.

[27] P. N. Keating, **Effect of invariance requirements on the elastic strain energy of crystals with application to the diamond structure**, *Phys. Rev.*, vol. 145, pp. 637–645, 2 1966. DOI: 10.1103/PhysRev.145.637.

[28] J. S. Pedersen, **Surface relaxation by the keating model: A comparison with ab-initio calculations and x-ray diffraction experiments**, *Surface Science*, vol. 210, no. 1, pp. 238–250, 1989, ISSN: 0039-6028. DOI: https://doi.org/10.1016/0039-6028(89)90114-3.

[29] R. J. Hamers, R. M. Tromp, and J. E. Demuth, **Scanning tunneling microscopy of si(001)**, *Phys. Rev. B*, vol. 34, pp. 5343–5357, 8 1986. DOI: 10.1103/PhysRevB.34.5343.

[30] H. Over *et al.*, **Surface atomic geometry of si(001)-(2×1): A low-energy electron-diffraction structure analysis**, *Phys. Rev. B*, vol. 55, pp. 4731–4736, 7 1997. DOI: 10.1103/PhysRevB.55.4731.

[31] T. Yokoyama and K. Takayanagi, **Anomalous flipping motions of buckled dimers on the si(001) surface at 5 k**, *Phys. Rev. B*, vol. 61, R5078–R5081, 8 2000. DOI: 10.1103/PhysRevB.61.R5078.

[32] T. Shirasawa, S. Mizuno, and H. Tochihara, **Electron-beam-induced disordering of the si(001)-c(4×2) surface structure**, *Phys. Rev. Lett.*, vol. 94, p. 195 502, 19 2005. DOI: 10.1103/PhysRevLett.94.195502.

[33] T. Uda *et al.*, **Ground state of the si(001) surface revisited – is seeing believing?**, *Progress in Surface Science*, vol. 76, no. 6, pp. 147–162, 2004, ISSN: 0079-6816. DOI: https://doi.org/10.1016/j.progsurf.2004.05.015.

[34] Y. J. Li *et al.*, **Origin of p(2×1) phase on si(001) by noncontact atomic force microscopy at 5 k**, *Phys. Rev. Lett.*, vol. 96, p. 106 104, 10 2006. DOI: 10.1103/PhysRevLett.96.106104.

[35] K. Takayanagi, Y. Tanishiro, M. Takahashi, and S. Takahashi, **Structural analysis of si(111)-7×7 by uhv-transmission electron diffraction and microscopy**, *Journal of Vacuum Science and Technology A*, vol. 3, 1984.

[36] J. Kautz, M. W. Copel, M. S. Gordon, R. M. Tromp, and S. J. van der Molen, **Titration of submonolayer au growth on si(111)**, *Phys. Rev. B*, vol. 89, p. 035 416, 3 2014. DOI: 10.1103/PhysRevB.89.035416.

[37] H. Li *et al.*, **Multilayer relaxation of clean ag{001}**, *Phys. Rev. B*, vol. 43, pp. 7305–7307, 9 1991. DOI: 10.1103/PhysRevB.43.7305.

[38] L. Hammer, Friedrich-Alexander-Universität Erlangen-Nürnberg, private communication.

[39] S. Mizuno, T. Shirasawa, Y. Shiraishi, and H. Tochihara, **Structure determination of si(001)-c(4 × 2) surfaces at 80 k and electron beam effect below 40 k studied by low-energy electron diffraction**, *Phys. Rev. B*, vol. 69, p. 241 306, 24 2004. DOI: 10.1103/PhysRevB.69.241306.

[40] F Jona, H. D. Shih, D. W. Jepsen, and P. M. Marcus, **On the structure of reconstructed si(001)2×1 and ge(001)2×1 surfaces**, *Journal of Physics C: Solid State Physics*, vol. 12, no. 12, pp. L455–L461, 1979. DOI: 10.1088/0022-3719/12/12/002.

[41] J. Ihm, M. L. Cohen, and D. J. Chadi, **(2 × 1) reconstructed si(001) surface: Self-consistent calculations of dimer models**, *Phys. Rev. B*, vol. 21, pp. 4592–4599, 10 1980. DOI: 10.1103/PhysRevB.21.4592.

[42] W. S. Yang, F. Jona, and P. M. Marcus, **Atomic structure of si{001}2×1**, *Phys. Rev. B*, vol. 28, pp. 2049–2059, 4 1983. DOI: 10.1103/PhysRevB.28.2049.

[43] I. P. Batra, **Atomic structure of the si(001)-(2 × 1) surface**, *Phys. Rev. B*, vol. 41, pp. 5048–5054, 8 1990. DOI: 10.1103/PhysRevB.41.5048.

[44] A. Ramstad, G. Brocks, and P. J. Kelly, **Theoretical study of the si(100) surface reconstruction**, *Phys. Rev. B*, vol. 51, pp. 14 504–14 523, 20 1995. DOI: 10.1103/PhysRevB.51.14504.

[45] R. Felici *et al.*, **Room temperature si(001)-(2 × 1) reconstruction solved by x-ray diffraction**, *Surface Science*, vol. 375, no. 1, pp. 55–62, 1997, ISSN: 0039-6028. DOI: https://doi.org/10.1016/S0039-6028(97)80005-2.

[46] T. Shirasawa, S. Mizuno, and H. Tochihara, **Structural analysis of the c(4 × 2) reconstruction in si(001) and ge(001) surfaces by low-energy electron diffraction**, *Surface Science*, vol. 600, no. 4, pp. 815–819, 2006, ISSN: 0039-6028. DOI: https://doi.org/10.1016/j.susc.2005.11.031.

[47] M. Nishizawa *et al.*, **Origin of type-C defects on the si(100)-(2 × 1) surface**, *Phys. Rev. B*, vol. 65, p. 161 302, 16 2002. DOI: 10.1103/PhysRevB.65.161302.

[48] A. Barbieri and M. V. Hove, private communication.

[49] S. Sanna, Justus-Liebig-Universität Gießen, private communication.

[50] L. E. Berman, B. W. Batterman, and J. M. Blakely, **Structure of submonolayer gold on silicon (111) from x-ray standing-wave triangulation**, *Phys. Rev. B*, vol. 38, pp. 5397–5405, 8 1988. DOI: 10.1103/PhysRevB.38.5397.

[51] R. Feidenhans'L, F. Grey, J. Bohr, M. Nielsen, and R. Johnson, **Investigation of the au/si (111) surface structures by x-ray diffraction**, *Journal de Physique Colloques*, vol. 50, no. C7, pp. 175–179, 1989. DOI: 10.1051/jphyscol:1989717.

[52] A. A. Baski, J. Nogami, and C. F. Quate, **Si(111)-5×1-au reconstruction as studied by scanning tunneling microscopy**, *Phys. Rev. B*, vol. 41, pp. 10 247–10 249, 14 1990. DOI: 10.1103/PhysRevB.41.10247.

[53] T. Hasegawa, K. Takata, S. Hosaka, and S. Hosoki, **Au-induced reconstructions of the si(111) surface**, *Journal of Vacuum Science & Technology A*, vol. 8, no. 1, pp. 241–244, 1990. DOI: 10.1116/1.577075.

[54] J. O'Mahony *et al.*, **The au-induced 5×2 reconstruction on si(111)**, *Surface Science Letters*, vol. 277, no. 1, pp. L57–L62, 1992. DOI: https://doi.org/10.1016/0167-2584(92)90111-H.

[55] L. D. Marks and R. Plass, **Atomic structure of si(111)-(5 × 2)-au from high resolution electron microscopy and heavy-atom holography**, *Phys. Rev. Lett.*, vol. 75, pp. 2172–2175, 11 1995. DOI: 10.1103/PhysRevLett.75.2172.

[56] S. C. Erwin, **Self-doping of gold chains on silicon: A new structural model for si(111) -(5 × 2)-au**, *Phys. Rev. Lett.*, vol. 91, p. 206 101, 20 2003. DOI: 10.1103/PhysRevLett.91.206101.

[57] S. Riikonen and D. Sánchez-Portal, **First-principles study of the atomic and electronic structure of the si(111)-(5 × 2)-au surface reconstruction**, *Phys. Rev. B*, vol. 71, p. 235 423, 23 2005. DOI: 10.1103/PhysRevB.71.235423.

[58] F.-C. Chuang, C.-H. Hsu, C.-Z. Wang, and K.-M. Ho, **Honeycomb chain structure of the au/si(111)-(5 × 2) surface reconstruction: A first-principles study**, *Phys. Rev. B*, vol. 77, p. 153 409, 15 2008. DOI: 10.1103/PhysRevB.77.153409.

[59] T. Abukawa and Y. Nishigaya, **Structure of the si(111)-(5 × 2)-au surface**, *Phys. Rev. Lett.*, vol. 110, p. 036 102, 3 2013. DOI: 10.1103/PhysRevLett.110.036102.

[60] T. Shirasawa *et al.*, **Identification of the structure model of the si(111)-(5 × 2)-au surface**, *Phys. Rev. Lett.*, vol. 113, p. 165 501, 16 2014. DOI: 10.1103/PhysRevLett.113.165501.

[61] K. Seino and F. Bechstedt, **First-principles calculations of energetics and electronic structure for reconstructed si(111)-(5 × n)-au surfaces**, *Phys. Rev. B*, vol. 90, p. 165 407, 16 2014. DOI: 10.1103/PhysRevB.90.165407.

[62] V. Blum and K. Heinz, **Fast leed intensity calculations for surface crystallography using tensor leed**, *Computer Physics Communications*, vol. 134, no. 3, pp. 392–425, 2001, ISSN: 0010-4655. DOI: https://doi.org/10.1016/S0010-4655(00)00209-5.

[63] R. P. Feynman and H. Albert R, **Quantum Mechanics and Path Integrals**. 1965.

[64] K. Kopitzki and P. Herzog, **Einführung in die Festkörperphysik** (Lehrbuch Physik). Teubner, 2004, ISBN: 9783519430834.

[65] K. Oura, V. Lifshits, A. Saranin, A. Zotov, and M. Katayama, **Surface Science: An Introduction** (Advanced Texts in Physics). Springer Berlin Heidelberg, 2003, ISBN: 9783540005452.

[66] F. Timmer, **Diffraction studies on ordering of quasi-one-dimensional structures and nanowires on silicon surfaces induced by metals**, Ph.D. dissertation, Universität Osnabrück, 2017.

[67] E. A. Soares, C. M. C. de Castilho, and V. E. de Carvalho, **Advances on surface structural determination by LEED**, *Journal of Physics: Condensed Matter*, vol. 23, no. 30, p. 303 001, 2011. DOI: 10.1088/0953-8984/23/30/303001.

[68] M. L. Viana *et al.*, **Novel genetic algorithm search procedure for leed surface structure determination**, *Journal of Physics: Condensed matter*, vol. 26, no. 22, p. 225 005, 2014. DOI: 10.1088/0953-8984/26/22/225005.

[69] CRAY Research, Inc., **Cray-1 computer system hardware reference manual 2240004**, 1977. [Online]. Available: http://bitsavers.trailing-edge.com/pdf/cray/CRAY-1/2240004C_CRAY-1_Hardware_Reference_Nov77.pdf, accessed 17. March 2022.

A. Mathematical Functions

Spherical Bessel function

The spherical Bessel functions of the first and second kind j_l and y_l are derived by the Bessel functions, which are the canonical solutions to the differential equation

$$x^2\frac{\mathrm{d}^2y}{\mathrm{d}x^2} + x\frac{\mathrm{d}y}{\mathrm{d}x} + (x^2 - \alpha^2)y = 0 \ .$$

The Bessel functions of the first kind J_α can be expressed generally as

$$J_{\alpha(x)} = \sum_{m=0}^{\infty} \frac{(-1)^m}{m!\Gamma_{(m+\alpha+1)}} \left(\frac{x}{2}\right)^{2m+\alpha} \ ,$$

with the gamma function $\Gamma_{(z)}$. The Bessel functions of the second kind Y_α are related to J_α by

$$Y_{\alpha(x)} = \frac{J_{\alpha(x)}\cos\alpha\pi - J_{-\alpha(x)}}{\sin\alpha\pi} \ .$$

The spherical Bessel functions can be expressed as

$$j_{l(x)} = \sqrt{\frac{\pi}{2x}} J_{l+\frac{1}{2}(x)} \qquad \text{and}$$
$$y_{l(x)} = \sqrt{\frac{\pi}{2x}} Y_{l+\frac{1}{2}(x)} \ .$$

Spherical Hankel function

The spherical Hankel functions of the first and second kind $\mathrm{h}_l^{(1)}$ and $\mathrm{h}_l^{(2)}$ are related to the spherical Bessel functions by

$$\mathrm{h}_l^{(1)}{}_{(x)} = j_{l(x)} + iy_{l(x)} \qquad \text{and}$$
$$\mathrm{h}_l^{(2)}{}_{(x)} = j_{l(x)} - iy_{l(x)} \ .$$

However, for the Hankel functions of integer order exist closed forms, since the Bessel functions of half-integer order can be expressed in terms of trigonometric functions:

$$\mathrm{h}_l^{(1)}{}_{(x)} = (-i)^{l+1} \ \frac{e^{ix}}{x} \sum_{m=0}^{l} \frac{i^m}{m!(2x)^m} \frac{(l+m)!}{(l-m)!} \ .$$

Spherical Harmonics

The spherical harmonics Y_l^m are a set of functions defined on the surface of a sphere and form an orthonormal basis, hence any function defined on the surface of a sphere can be expressed as a sum of spherical harmonics. They can be denoted by either $\mathrm{Y}_l^{m\,(\theta,\varphi)}$ or $\mathrm{Y}_l^{m\,(\mathbf{r})}$, where only the direction of $\mathbf{r}$ is relevant. They are defined by

$$\mathrm{Y}_l^{m\,(\theta,\varphi)} = \sqrt{\frac{(2l+1)}{4\pi}\frac{(l-m)!}{(l+m)!}}\ \mathrm{P}_l^{m\,(\cos\theta)}\ e^{im\varphi}\ ,$$

with the associated Legendre polynomials $\mathrm{P}_l^{m\,(\cos\theta)}$ given by

$$\mathrm{P}_l^{m\,(x)} = (-1)^m\ 2^l\left(1-x^2\right)^{\frac{m}{2}} \sum_{k=m}^{l} \frac{k!}{(k-m)!}\ x^{k-m} \binom{l}{k} \binom{\frac{l+k-1}{2}}{l}\ ,$$

containing the generalized form of the binomial coefficient

$$\binom{\alpha}{k} = \frac{A}{k!} \qquad \text{with}\quad A = \alpha(\alpha-1)(\alpha-2)\ \ldots\ (\alpha-k+1)\ .$$

Furthermore, the relations

$$\begin{aligned} {}^*\mathrm{Y}_l^{m\,(\theta,\varphi)} &= (-1)^m\ \mathrm{Y}_l^{-m\,(\theta,\varphi)} \qquad\qquad \text{and} \\ \mathrm{Y}_l^{m\,(\mathbf{r})} &= (-1)^l\ \mathrm{Y}_l^{m\,(-\mathbf{r})} \end{aligned}$$

can be useful in the computation (with the complex conjugation denoted by *).

Gaunt coefficients

The Gaunt coefficients γ are defined as

$$\gamma_{(l_1,m_1,l_2,m_2,l_3,m_3)} = \int_\varphi^{2\pi}\int_\theta^{\pi} \mathrm{Y}_{l_1}^{m_1\,(\theta,\varphi)}\ \mathrm{Y}_{l_2}^{m_2\,(\theta,\varphi)}\ \mathrm{Y}_{l_3}^{m_3\,(\theta,\varphi)}\ \sin\theta\ \mathrm{d}\theta\mathrm{d}\varphi\ . \tag{A.1}$$

Since the evaluation of the integrals is rather expensive, their relation to the Wigner 3-j-symbols can be used:

$$\begin{aligned} &\int_\varphi^{2\pi}\int_\theta^{\pi} \mathrm{Y}_{l_1}^{m_1\,(\theta,\varphi)}\ \mathrm{Y}_{l_2}^{m_2\,(\theta,\varphi)}\ \mathrm{Y}_{l_3}^{m_3\,(\theta,\varphi)}\ \sin\theta\ \mathrm{d}\theta\mathrm{d}\varphi \\ &\qquad = \sqrt{\frac{(2l_1+1)(2l_2+1)(2l_3+1)}{4\pi}} \begin{pmatrix} l_1 & l_2 & l_3 \\ 0 & 0 & 0 \end{pmatrix} \begin{pmatrix} l_1 & l_2 & l_3 \\ m_1 & m_2 & m_3 \end{pmatrix}\ . \end{aligned}$$

B. Supporting Information

Derivation of ΔE

Within section 2.3.1 an approximation for the peak width ΔE was postulated. To evaluate the equation

$$\sqrt{E}\ (\Delta\sqrt{E}) = \sqrt{E}\left(\sqrt{E+\frac{\Delta E}{2}} - \sqrt{E-\frac{\Delta E}{2}}\right)$$

the right side is squared, which yields

$$E\left(E+\frac{\Delta E}{2} - 2\sqrt{\left(E+\frac{\Delta E}{2}\right)\left(E-\frac{\Delta E}{2}\right)} + E - \frac{\Delta E}{2}\right)\ .$$

This can be rearranged to

$$E\left(2E - 2\sqrt{E^2 - \left(\frac{\Delta E}{2}\right)^2}\right)\ ,$$

and further simplified to

$$2E^2\left(1 - \sqrt{1-\left(\frac{\Delta E}{2E}\right)^2}\right)\ .$$

The approximation of $(1-x)^{\frac{1}{2}} \approx 1 - \frac{x}{2}$ according to the first two terms of a Taylor series leads to

$$2E^2\left(1 - \left[1 - \frac{\left(\frac{\Delta E}{2E}\right)^2}{2}\right]\right) = \left(\frac{\Delta E}{2}\right)^2\ .$$

Since the equation was squared in the beginning, this results in

$$\sqrt{E}\ (\Delta\sqrt{E}) \approx \left(\frac{\Delta E}{2}\right)\ .$$

Coordinates of Si(111)-(5 × 2)-Au

Table B.1.: Positions of silicon atoms in the top six layers of the substrate for the LEED optimized model. The coordinates are in the same reference frame as in Table 6.1.

layer	no.	x[Å]	y[Å]	z[Å]	layer	no.	x[Å]	y[Å]	z[Å]
1	1	1.92	1.12	9.375	4	1	0.00	-0.05	5.425
1	2	-1.92	1.18	9.363	4	2	-3.94	-0.05	5.425
1	3	0.00	4.34	9.439	4	3	1.92	3.32	5.493
1	4	-3.84	4.44	9.415	4	4	-1.92	3.32	5.493
1	5	1.96	7.71	9.520	4	5	0.00	6.65	5.570
1	6	-1.96	7.71	9.520	4	6	-3.84	6.75	5.558
1	7	0.00	11.25	9.497	4	7	1.92	9.92	5.580
1	8	-3.84	11.09	9.513	4	8	-1.92	9.92	5.580
1	9	1.94	14.58	9.364	4	9	0.00	13.25	5.518
1	10	-1.94	14.58	9.364	4	10	-3.84	13.30	5.476
2	1	0.01	2.20	8.527	5	1	0.00	0.00	3.091
2	2	-3.88	2.21	8.521	5	2	-3.84	0.00	3.086
2	3	1.85	5.53	8.716	5	3	1.92	3.32	3.115
2	4	-1.85	5.53	8.716	5	4	-1.92	3.32	3.117
2	5	0.00	8.99	8.767	5	5	0.00	6.65	3.205
2	6	-3.84	8.85	8.738	5	6	-3.84	6.65	3.180
2	7	1.97	12.26	8.701	5	7	1.92	9.97	3.184
2	8	-1.97	12.26	8.701	5	8	-1.92	9.97	3.184
2	9	0.00	15.56	8.524	5	9	0.00	13.30	3.166
2	10	-3.84	15.55	8.505	5	10	-3.84	13.30	3.141
3	1	0.00	2.10	6.198	6	1	1.92	1.11	2.335
3	2	-3.89	2.20	6.202	6	2	-1.92	1.11	2.336
3	3	1.81	5.55	6.360	6	3	0.00	4.43	2.367
3	4	-1.81	5.55	6.360	6	4	-3.84	4.43	2.364
3	5	0.00	9.00	6.388	6	5	1.92	7.76	2.379
3	6	-3.84	8.86	6.368	6	6	-1.92	7.76	2.378
3	7	1.94	12.22	6.328	6	7	0.00	11.08	2.402
3	8	-1.94	12.22	6.328	6	8	-3.84	11.08	2.390
3	9	0.00	15.49	6.182	6	9	1.92	14.41	2.354
3	10	-3.84	15.65	6.164	6	10	-1.92	14.41	2.355

Deviation between the KK and KK* model

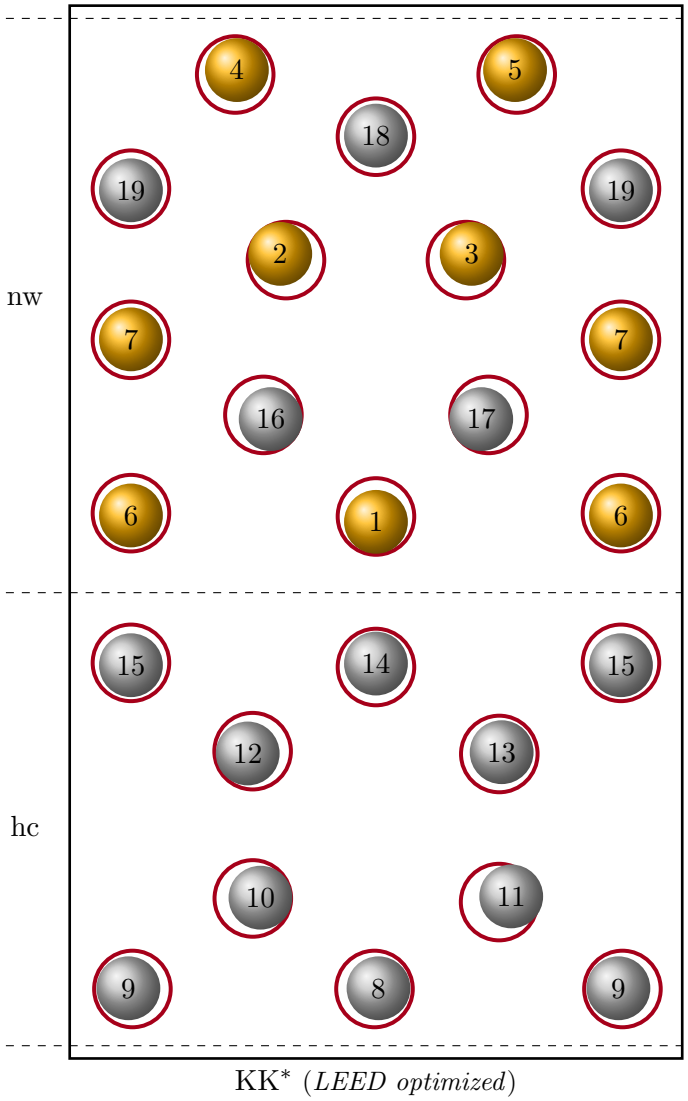

Figure B.1.: Comparison off the surface of the KK model derived by DFT (red circles) with the KK* model, which was optimized with LEED data (yellow spheres for gold atoms and gray spheres for silicon atoms). Except from small differences within the uncertainty of the LEED analysis the two models are in very good accordance. The deviations in the honeycomb motif (hc) are expected to originate in the different possible alignments of adjacent unit cells (cf. Figure 6.8).

Table B.2.: Differences from the KK* model (optimized by LEED) to the KK model (derived by DFT) of the surface and topmost silicon bilayer. The cartesian components are given as well as the radial difference (Δr) 6.1. The numbers of layers and atoms corresponds to Table 6.1 and Table B.1, respectively.

layer	no.		Δx[Å]	Δy[Å]	Δz[Å]	Δr[Å]
Surf	1	Au	0.00	-0.08	-0.006	0.080
Surf	2	Au	-0.09	0.10	0.019	0.136
Surf	3	Au	0.09	0.10	0.019	0.136
Surf	4	Au	0.03	0.07	-0.014	0.077
Surf	5	Au	-0.03	0.07	-0.014	0.077
Surf	6	Au	0.00	-0.04	0.021	0.045
Surf	7	Au	0.00	0.01	0.001	0.010
Surf	8	hc	0.06	0.01	-0.023	0.065
Surf	9	hc	-0.06	0.01	-0.023	0.065
Surf	10	hc	0.12	0.01	-0.010	0.121
Surf	11	hc	0.19	0.09	0.013	0.211
Surf	12	hc	-0.08	-0.04	-0.012	0.090
Surf	13	hc	0.04	0.03	-0.015	0.052
Surf	14	hc	0.00	0.05	-0.031	0.059
Surf	15	hc	0.00	-0.04	-0.025	0.047
Surf	16	nw	0.11	-0.07	-0.025	0.133
Surf	17	nw	-0.11	-0.07	-0.025	0.133
Surf	18	nw	0.00	0.02	0.009	0.022
Surf	19	nw	0.00	-0.03	-0.037	0.048
1	1		0.00	0.00	-0.058	0.058
1	2		0.01	0.04	-0.058	0.071
1	3		0.00	0.01	-0.042	0.043
1	4		0.00	0.09	-0.044	0.100
1	5		0.06	-0.04	-0.047	0.086
1	6		-0.07	-0.04	-0.047	0.093
1	7		0.00	0.00	-0.036	0.036
1	8		0.00	-0.01	-0.058	0.059
1	9		0.00	0.02	-0.017	0.026
1	10		-0.00	0.02	-0.017	0.026
2	1		0.00	0.02	-0.032	0.038
2	2		-0.04	0.02	-0.034	0.056
2	3		-0.06	0.01	-0.038	0.072
2	4		0.06	0.01	-0.038	0.072
2	5		0.00	0.04	-0.037	0.054
2	6		0.00	-0.01	-0.058	0.059
2	7		0.01	-0.02	-0.017	0.028
2	8		-0.01	-0.02	-0.017	0.028
2	9		0.00	-0.02	0.017	0.026
2	10		0.00	0.01	-0.016	0.019

C. List of Symbols and Abbreviations

Abbreviations

EBH model	Structural model of Si(111)-(5 × 2)-Au proposed by Erwin, Barke and Himpsel
GUI	Graphical User Interface
IV	Intensity-Voltage (implying the dependence of spot intensity from the accelerating voltage)
KK model	Structural model of Si(111)-(5 × 2)-Au proposed by Kwon and Kang
LEED	Low-Energy Electron Diffraction
MCP	Micro-Channel Plate
ROI	Region of Interest
STM	Scanning Tunneling Microscopy
SXRD	Surface X-ray Diffraction
UHV	Ultra High Vacuum

Symbols

R_{P}	Pendry R (Reliability) Factor
δ_l	Phase shift
t_l	scattering element (amplitude of a scattered spherical wave)
t_θ	atomic scattering factor
${}_i^j G$	Propagator from atom i to atom j
${}_i T$	Scattering matrix of atom i
$\mathrm{h}_l^{(1)}(x)$	Spherical Hankel function of the first kind
$\mathrm{h}_l^{(2)}(x)$	Spherical Hankel function of the second kind
$j_l(x)$	Spherical Bessel function of the first kind
$y_l(x)$	Spherical Bessel function of the second kind
$\mathrm{Y}_l^m(\theta,\varphi)$ or $\mathrm{Y}_l^m(\mathbf{r})$	Spherical Harmonic
$\gamma(l_1,m_1,l_2,m_2,l_3,m_3)$	Gaunt coefficients

Danksagung

An dieser Stelle möchte ich allen Menschen danken, die mich unterstützt haben und somit ihren Beitrag zum Gelingen dieser Arbeit geleistet haben.
Besonders bedanken möchte ich mich bei meinem Doktorvater Prof. Dr. Joachim Wollschläger; zuerst einmal allgemein für die Betreuung mit stets guter Laune, die eine tolle Arbeitsatmosphäre geschaffen hat, insbesondere aber auch für die fortwährende Unterstützung, sodass aus zahlreichen Ideen und Diskussionen diese Doktorarbeit entstehen konnte. Zudem sei Prof. Dr. Simone Sanna dafür gedankt, mir die DFT-Strukturmodelle zur Verfügung zu stellen und die Rolle des Zweitgutachters zu übernehmen.
Außerdem möchte ich Dr. Lutz Hammer und Tilman Kißlinger von der Friedrich-Alexander-Universität Erlangen-Nürnberg dafür danken, dass sie ihre Erfahrungen bezüglich LEED Analysen mit mir geteilt haben. Ein großer Dank gilt außerdem Jannis Thien, meinem langjährigen Bürokollegen, für die Diskussionen etlicher Fragestellungen und den stets spaßigen Arbeitsalltag. Des Weiteren sei Gregor Steinhoff für die tatkräftige Unterstützung im Labor gedankt, insbesondere beim umfangreichen Aufbau der UHV-Kammer. Außerdem danke ich Florian Steinbach, mit dem ich im Rahmen seiner Bachelorarbeit Messungen durchgeführt habe, die Eingang in diese Arbeit gefunden haben.
Natürlich gilt mein Dank auch allen nicht namentlich genannten Mitgliedern und Ehemaligen der AG für die gute Arbeitsatmosphäre. Für die vielen Konstruktionen und Reparaturen gilt mein Dank ebenfalls der Feinmechanischen Werkstatt.
Abschließend geht noch ein herzlicher Dank an meine Familie und meine Frau Miriam für die bedingungslose Unterstützung sowie an meine Kinder Vincent und Linnea Noemi, deren Lachen jeden Tag erhellt.

Vielen Dank!